REMOVAL AND RECOVERY OF PHOSPHONATE ANTISCALANTS

Luciaan Boels

Cover image: Jos Blomsma and Luciaan Boels
Cover design: Peter de Jong

ISBN: 978-94-6108-370-8

Boels, L., 2012
Removal and Recovery of Phosphonate Antiscalants

PhD thesis Delft University of Technology, Delft, The Netherlands – with references – with summary in Dutch

Printed by: Gildeprint Drukkerijen, Enschede, The Netherlands

REMOVAL AND RECOVERY OF PHOSPHONATE ANTISCALANTS

Proefschrift

ter verkrijging van de graad van doctor
aan de Technische Universiteit Delft,
op gezag van de Rector Magnificus Prof. Ir. K.C.A.M. Luyben,
voorzitter van het College voor Promoties,
in het openbaar te verdedigen op maandag 26 november 2012 om 15.00 uur.

door

Luciaan BOELS

Scheikundig Ingenieur
geboren te Emmen

Dit proefschrift is goedgekeurd door de promotor:

Prof. Dr. G. J. Witkamp

Samenstelling promotiecommissie:

Rector Magnificus,	voorzitter
Prof. Dr. G. J. Witkamp,	Technische Universiteit Delft, promotor
Prof. Dr. Ir. L. A. M. van der Wielen	Technische Universiteit Delft
Prof. Dr. A. Schmidt-Ott	Technische Universiteit Delft
Prof. Dr. Ir. P. J. A. M. Kerkhof	Technische Universiteit Eindhoven
Prof. M. D. Kennedy, PhD	UNESCO-IHE / Technische Universiteit Delft
Prof. Dr. Ir. H. H. M. Rijnaarts	Wageningen Universiteit
Dr. Ir. K. J. Keesman	Wageningen Universiteit

SUMMARY

In reverse osmosis (RO) desalination processes, the use of phosphonates prevents scaling, thus allowing for a higher product water recovery, which increases the efficiency of the process. However, a major concern associated with their use in RO desalination is the high cost and environmental impacts associated with the discharge of the waste brine or membrane concentrate containing phosphonates. Therefore, technologies are needed that can remove and recover phosphonate antiscalants from membrane concentrates. Chapters 2 to 5 of this thesis describe a process for the removal and recovery of phosphonate antiscalants by using adsorption technology.

In **Chapter 2** the phosphonate adsorption capacities of two commercially available anion exchange resins and activated carbon were compared to that of the cheap waste material iron-coated waste filtration sand (WFS). The results presented showed that, in contrast to the exchange resins, the equilibrium adsorption of nitrilotris(methylene phosphonic acid) (NTMP) on WFS is not suppressed at increasing ionic strength and is much less affected by the competitive anions carbonate and sulfate. The strong affinity of phosphonate with the iron oxy-hydroxide in the coating resulted in a relatively high adsorption capacity for NTMP of this waste material.

Iron oxy-hydroxides perform very well in adsorbing phosphonates from membrane concentrates. Therefore, an iron oxy-hydroxide was selected that, in contrast with WFS, has a high purity and can be obtained commercially. Granular ferric hydroxide (GFH) was investigated as an adsorbent for NTMP in **Chapter 3**. Both the equilibrium and kinetics of NTMP adsorption on GFH were investigated. The adsorption kinetics were predicted fairly well with two models that considered either combined film-pore or combined film-surface diffusion as the main mechanisms for mass transport. It was demonstrated that phosphonate is preferentially adsorbed over sulfate by GFH and that the presence of calcium is beneficial for the adsorption process. Calcium causes a transformation in the equilibrium adsorption isotherm from a Langmuir type to a Freundlich type with much higher adsorption capacities. Spent GFH is reusable after regeneration with a sodium hydroxide solution, showing that

NTMP can be recovered from the RO concentrate.

In analogy with Chapter 3, the adsorption and desorption of NTMP from RO membrane concentrate on iron-coated waste filtration sand (WFS) has been investigated in **Chapter 4**. Equilibrium adsorption was described well with a Langmuir isotherm. Although the low cost and on-site availability of WFS is advantageous over GFH, the results revealed some drawbacks. WFS appeared to have a much lower adsorption capacity compared to GFH, which was related to the presence of impurities, the presence of manganese oxides, and aging of the ferrihydrite phase in the coating of WFS.

The aim of **Chapter 5** was to employ GFH in a packed bed adsorption column. The effective diffusivities and external film mass transfer coefficients estimated in Chapter 3 were used to predict the concentration of phosphonate in the effluent. Also, the regeneration of the saturated column with sodium hydroxide solution was investigated. In addition, it was investigated whether the regeneration solution containing the recovered phosphonate could be further concentrated by using a nano-filtration or a calcium-phosphonate precipitation step. The use of nano-filtration seemed to be more attractive.

The first five chapters show that adsorptive removal of phosphonate antiscalants offers a viable way to improve RO concentrate treatment processes and enables the recovery of the phosphonate for reuse in the RO desalination process. Another way of tackling the unwanted discharge of phosphonates is minimizing their use. Smart sensors that predict the risk of scaling at an early stage can help to control the dosage of phosphonate antiscalants. This will allow for minimum usage of phosphonates without the risk of scaling. Chapters 6, 7, and 8 contribute to the development of such a sensor. Focus was on the development of the actuator part of the sensor that enhances crystal growth and precipitation by ultrasonic irradiation.

In **Chapter 6** the effect of ultrasonic irradiation on the crystallization of calcite was investigated. Seeded calcite growth experiments were conducted under constant composition conditions while the applied ultrasonic irradiation created cavitation bubbles throughout the suspension. In this way it was demonstrated that ultrasound enhances the crystallization rate of calcite

substantially (i.e., 46 %), due to the ability of the generated cavitation bubbles altering the crystals' habit and size. The increased surface area available for crystal growth resulted in enhancement of the observed crystallization rate.

In **Chapter 7**, the cavitation phenomena that are responsible for the previously observed volumetric crystallization rate enhancement were visualized using high speed photography. Cavitation clusters cause attrition, disruption of aggregates and deagglomeration, whereas streamer cavitation causes deagglomeration only. Cavitation inception on the surface gave the small crystals momentum. However, it was shown that breakage of accelerated crystals by interparticle collisions is unrealistic because, upon bubble collapse, they subsequently experienced a deceleration much stronger than expected from drag forces. These direct observations contradict the general assumption that interparticle collisions always play an important role in particle attrition by cavitation. Scanning electron microscopy pictures of irradiated calcite crystals showed deep circular indentations, possibly caused by shockwave induced jet impingement. Moreover, the appearance of voluminous fragments with large planes of fracture indicated that acoustic cavitation can also cause the breakage of single crystal structures.

The possibility of using ultrasound as a tool to enhance the demineralization of supersaturated calcium carbonate solutions (e.g., membrane concentrates) containing growth inhibitors was investigated in **Chapter 8**. The inhibiting effect of the phosphonate NTMP on crystal growth can be mitigated by ultrasonic irradiation. The results can be explained in part by breakage and attrition of poisoned crystals, resulting in an increase in fresh surface area. Mass spectroscopy analysis of sonicated NTMP solutions revealed that ultrasound can also degrade NTMP. These observations confirm in part the hypothesis that ultrasound can be used as actuator.

As an alternative to the removal of phosphonates or minimizing their use by smart sensoring techniques, phosphonates may also entirely be replaced by environmental friendly antiscalants, which is the subject of **Chapter 9**. The effectiveness of such an alternative, carboxymethyl inulin (CMI) biopolymers, in inhibiting calcium carbonate crystallization was compared to two

phosphonate antiscalants. Compared to the phosphonates, the biopolymers exhibited a stronger inhibitory effect on the crystal growth of calcite. It was shown that the ability of the biopolymers to mitigate the spontaneous precipitation of calcium carbonate is controlled by their degree of carboxylation. The biopolymers can affect the crystal habit similar to the phosphonates, which suggests that their function as crystal growth inhibitor is comparable. These results demonstrate that CMI biopolymers are effective calcium carbonate crystallization inhibitors, indicating they can replace phosphonates as antiscalant.

In **Chapter 10**, the results presented in this work are being discussed and, where possible, placed into perspective of future desalination developments.

SAMENVATTING

Het gebruik van fosfonaten in omgekeerde osmose ontzoutingsprocessen voorkomt scaling. Hierdoor wordt het mogelijk een hogere product water recovery te halen zodat het rendement van het ontzoutingsproces stijgt. Een groot probleem echter dat gepaard gaat met het gebruik van fosfonaten zijn de hoge kosten en belasting op het milieu gerelateerd aan de lozing van brijnen of membraanconcentraten die deze fosfonaten bevatten. Er zijn daarom technologieën nodig die deze fosfonaatantiscalants kunnen verwijderen en terugwinnen uit membraanconcentraten. De hoofdstukken 2 tot en met 5 van dit proefschrift beschrijven een proces voor de verwijdering en terugwinning van fosfonaatantiscalants middels van adsorptietechnologie.

In **Hoofdstuk 2** werden de adsorptiecapaciteiten voor fosfonaat van twee commercieel beschikbare anion uitwisselingharsen en actief kool vergeleken met die van het goedkope afvalmateriaal ijzer-gecoat afvalfiltratiezand (WFS). De gepresenteerde resultaten laten zien dat de evenwichtsadsorptie van nitrilotris(methyleenfosfonzuur) (NTMP) op WFS in tegenstelling tot de anion uitwisselingsharsen niet wordt onderdrukt door een toenemende ionsterkte en in vergelijking veel minder wordt beïnvloed door de competitieve anionen carbonaat en sulfaat. De sterke affiniteit van fosfonaat met het ijzer oxy-hydroxide in de coating van WFS resulteerde in een relatief hoge adsorptiecapaciteit van dit afvalmateriaal voor NTMP.

IJzer oxy-hydroxides zijn zeer goed in staat fosfonaten te adsorberen uit membraanconcentraten. Daarom werd er een ijzer oxy-hydroxide geselecteerd dat, in tegenstelling tot WFS, een hoge zuiverheid heeft en commercieel beschikbaar is. Korrelvormig ferrihydroxide (GFH) werd onderzocht als adsorbens voor NTMP in **Hoofdstuk 3**. Zowel de evenwichtsadsorptie als de kinetiek van NTMP adsorptie op GFH werden onderzocht. De adsorptiekinetiek kon goed worden voorspeld met twee modellen waarin de gecombineerde film-poriediffusie of film-oppervlaktediffusie als belangrijkste mechanismen voor massatransport worden beschouwd.

Aangetoond werd dat fosfonaat preferent ten opzichte van sulfaat wordt geadsorbeerd door GFH en dat de aanwezigheid van calcium gunstig is voor

het adsorptieproces. Calcium zorgt onder andere voor een omzetting van de evenwichtsadsorptie-isotherm van een Langmuir type naar een Freundlich type met een veel hogere adsorptiecapaciteit. Gebruikt GFH kan worden hergebruikt na regeneratie met een natriumhydroxideoplossing. Dit duidt erop dat NTMP teruggewonnen kan worden uit het membraanconcentraat.

In analogie met Hoofdstuk 3 werd in **Hoofdstuk 4** de adsorptie en desorptie van NTMP uit RO membraanconcentraat op ijzer gecoat afvalfiltratiezand (WFS) onderzocht. De evenwichtsadsorptie kon goed beschreven worden met een Langmuir isotherm.

Hoewel WFS in het voordeel is ten opzichte van GFH door een lage prijs en lokale beschikbaarheid, onthulden de resultaten ook nadelen van het gebruik van WFS. WFS blijkt een veel lagere adsorptiecapaciteit te hebben ten opzichte van GFH. Deze lagere adsorptiecapaciteit kon worden gerelateerd aan de aanwezigheid van verontreinigingen, de aanwezigheid van mangaanoxides en het verouderen van de ferrihydrietfase in de coating van WFS.

Het doel van **Hoofdstuk 5** was om GFH te gebruiken in een gepakte adsorptiekolom. De effectieve diffusiecoëfficiënten en de externe film massatransportcoëfficiënten die werden bepaald in Hoofdstuk 3, werden gebruikt om de concentratie fosfonaat in het effluent van de kolom te voorspellen. Voorts werd de regeneratie van de verzadigde kolom met natriumhydroxideoplossing onderzocht. Daarnaast werd onderzocht of de regeneratieoplossing met daarin teruggewonnen fosfonaat verder opgewerkt kan worden door middel van een nano-filtratie of een calcium-fosfonaat precipitatie stap. Het gebruik van nano-filtratie bleek technisch gezien de voorkeur te hebben.

De eerste vijf hoofdstukken hebben laten zien dat de verwijdering van fosfonaatantiscalants door middel van adsorptie op ijzer oxy-hydroxides een veelbelovende manier is om de behandeling van RO concentraten te verbeteren en om fosfonaat te kunnen terugwinnen voor hergebruik in het RO ontzoutingsproces. Een andere optie om de ongewenste lozing van fosfonaten aan te pakken is door hun gebruik te minimaliseren. Slimme sensoren die het gevaar van scaling in een vroegtijdig stadium kunnen voorspellen, zouden de

dosering van antiscalants kunnen verbeteren. Op deze manier kan het gebruik van fosfonaten geminimaliseerd worden zonder dat er scaling optreedt. De Hoofdstukken 6, 7 en 8 dragen bij aan de ontwikkeling van een dergelijke sensor. De nadruk lag hier op de ontwikkeling van de actuator van de sensor die als functie heeft kristalgroei en precipitatie versneld te induceren middels ultrasone geluidsgolven.

In **Hoofdstuk 6** werd het effect van ultrasone bestraling op de kristallisatie van calciet onderzocht. Bij een constante oververzadiging lieten we bestaande calcietkiemen uitgroeien in de aanwezigheid van cavitatiebellen die opgewekt werden door middel van ultrageluid. Op deze manier kon worden aangetoond dat ultrageluid de kristallisatiesnelheid van calciet fors kan laten toenemen (i.c., 46 %) als gevolg van het vermogen van de opgewekte cavitatiebellen om het uiterlijk en de grootte van de kristallen te beïnvloeden. Het toegenomen kristaloppervlak dat beschikbaar is voor groei veroorzaakte de waargenomen toename in kristallisatiesnelheid.

In **Hoofdstuk 7** werden de cavitatiefenomenen die verantwoordelijk zijn voor de eerdere waargenomen toename in kristallisatiesnelheid gevisualiseerd met behulp van een hogesnelheidscamera. Cavitatieclusters veroorzaken attritie, disruptie van aggregaten en deagglomeratie, terwijl stromercavitatie alleen deagglomeratie veroorzaakte. Cavitatie-inceptie op het kristaloppervlak gaf de kleine kristallen impuls. Er werd echter aangetoond dat het opbreken van versnelde kristallen door onderlinge botsingen onrealistisch is omdat ze door de latere implosie van de cavitatiebel een afremmende kracht ondervinden die groter is dan de verwachtte frictiekrachten.

Deze directe observaties zijn in tegenspraak met de algemene aanname dat onderlinge botsingen altijd een belangrijke rol spelen in het opbreken van deeltjes door cavitatie. Rasterelectronenmicroscopische foto's van ultrasoon bestraalde calcietkristallen lieten diepe cirkelvormige inkepingen zien die mogelijk veroorzaakt zijn door schokgolf geïnduceerde jet inslagen. Ook de aanwezigheid van volumineuze fragmenten met grote breukvlakken wijzen op het opbreken van kristalstructuren door akoestische cavitatie.

De mogelijkheid om ultrageluid te gebruiken om de demineralisatie van

oververzadigde calciumcarbonaatoplossingen (bijvoorbeeld membraan-concentraten) met daarin kristalgroeiremmers te versnellen werd onderzocht in **Hoofdstuk 8**. Het remmende effect van de fosfonaat NTMP op de kristalgroei kan ondermijnd worden onder invloed van ultrasone bestraling. De resultaten konden deels verklaard worden door de attritie en het opbreken van met NTMP vergiftigde kristallen wat gepaard gaat met een toename van schoon kristaloppervlak. Analyse van ultrasoon behandelde NTMP oplossingen met massaspectroscopie liet zien dat ultrageluid NTMP ook kan afbreken. Deze waarnemingen bevestigen deels de hypothese dat ultrageluid gebruikt kan worden als actuator voor kristallisatie.

Als alternatief voor de verwijdering van fosfonaten of het minimaliseren van hun gebruik met slimme sensortechnieken, zouden de fosfonaten ook volledig vervangen kunnen worden door milieuvriendelijke antiscalants. Dit is het onderwerp van **Hoofdstuk 9**. De effectiviteit van een dergelijk alternatief, carboxymethylinuline (CMI) biopolymeren, in het remmen van calciumcarbonaat kristallisatie werd vergeleken met twee typen fosfonaatantiscalants. In vergelijking tot deze fosfonaten, vertoonden de biopolymeren een sterker remmend effect op de kristalgroei van calciet. Aangetoond werd dat het vermogen van de biopolymeren om de spontane precipitatie van calciumcarbonaat te remmen wordt bepaald door het aantal carbonzuregroepen die de biopolymeren bevatten. CMI biopolymeren en fosfonaten beïnvloeden het uiterlijk van de kristallen op een vergelijkbare manier. Hieruit werd geconcludeerd dat CMI biopolymeren en fosfonaten op een vergelijkbare manier functioneren als kristalgroeiremmer. Deze resultaten laten zien dat CMI biopolymeren effectieve remmers van calciumcarbonaatkristallisatie zijn en daarom fosfonaten mogelijk kunnen vervangen als antiscalant.

In **Hoofdstuk 10** worden de resultaten van dit werk bediscussieerd en waar mogelijk in perspectief geplaatst van de toekomstige ontwikkelingen op het gebied van ontzoutingsprocessen.

TABLE OF CONTENTS

INTRODUCTION 1

Fresh water is the most important natural resource necessary for the survival of all ecosystems, yet only 2.5 % of the earth's water is fresh water, of which the majority is locked in ice (1). Moreover, the available water in aquifers is drained at a rate larger than the natural recharge rate. The limitation of fresh water resources in a world where population grows, climate changes, and pollution increases, threatens the adequacy of future drinking water supplies (2). As a consequence, the development of techniques to save, purify, and desalinate water to secure water supplies, has emerged as one of the major challenges of the 21st century. While conventional water resources are declining and salt water is abundantly available, desalination has emerged as an economically attractive and competitive way to satisfy the growing demand for water. However, a major concern associated with desalination processes is the environmental impact of the waste brine discharge. Besides the high salt content, these waste brines contain chemical additives necessarily used to avoid scaling in the process equipment. These additives, antiscalants, can impose a threat to the environment when discharged. This chapter provides a general background for this work that aims at finding methods to avoid such antiscalant discharge. It starts with explaining the formation of scaling, the control of scaling by the use of antiscalants, and the problems associated with the discharge of antiscalant containing waste brines. It furthermore introduces briefly the approaches that have been investigated in order to fulfil the presented research objectives.

1.1 Desalination

The limitation of fresh water resources has led to the rapid increase in the development and installation of processes that can desalinate abundantly available salt and brackish water.

Desalination processes effectively remove fresh water from salty water, producing a water product stream with a low concentration of salt and another stream with a high concentration of remaining salts, i.e., the waste brine or concentrate. Desalination processes are primarily devoted to convert seawater and brackish groundwater into drinking water. From the early 1950s, mainly thermal driven processes were developed for desalination operations. Today, however, reverse osmosis desalination, a pressure drive membrane process, has emerged as the most important desalination process since its commercialization in the 1970s. Approximately 51 % of the total global water production (i.e., 44.8 Mm^3 per day) is accomplished by reverse osmosis (RO). The market share of RO in desalting seawater is 35 %, while thermal desalination processes account for 61 %. For brackish water desalination, on the other hand, thermal desalination plays a negligible role (< 2 %), while RO accounts for 84 % of the total production capacity (3). Desalination by RO generally has lower capital costs and requires less energy compared to thermal desalination processes, especially for brackish water desalination.

1.2 Scale formation and control

The key factors that determine the economical feasibility of an RO installation are the water product recovery (i.e., the ratio of the product volume to the feed volume), the process operating costs, and the value of the water product. Especially for brackish water RO installations, water product recovery has to be sufficiently high, i.e., ≥ 70 – 80 %. However, high water product recoveries provoke the accumulation of rejected constituents on the membrane surface, causing the membrane to foul. Fouling is a serious problem, because it results in permeate flux decline, membrane degradation, increased transmembrane pressures, and elevated operating costs. Three kinds of fouling

can be distinguished: cake formation by the accumulation of rejected solids, biofouling by colonization of the membrane with microorganisms, and scale formation by the crystallization of sparingly soluble minerals (4).

Fouling is a complex phenomenon and its nature is strongly dependent on the feed water source, operating conditions, type of membrane, and membrane module geometry. Therefore, fouling may be prevented or delayed by altering the feed water characteristics or by optimizing the operating parameters and system design.

1.2.1 Scaling

The high operating water product recoveries and salt rejection efficiencies of RO desalination processes cause a 4 to 10 times increase of the relative dissolved salt concentration. As a result, sparingly soluble salts, like $CaCO_3$, $BaSO_4$, and $CaSO_4$, often attain a state of supersaturation in the water stream containing the rejected constituents; the concentrate. In addition, the concentration of salts near the membrane surface is even higher due to a phenomenon called concentration polarization. This mechanism may even cause a supersaturation of the salts near the membrane surface while their concentration in the bulk is still undersaturated. Supersaturation means that the water contains more dissolved salt than that represented by the thermodynamic equilibrium saturation. Therefore, there is a risk that the supersaturated salts crystallize which can lead to the formation of hard mineral deposits on the membrane surface, i.e., scaling.

Although supersaturation is the driving force for crystallization, it is not the only factor that determines when and at which rate the crystals will form. The cation to anion ratio, the availability of a favorable crystallization surface, and the presence of inorganic and organic impurities are also key factors in the process of crystallization. In addition, these factors influence the crystalline form in which the salt crystallizes and the habit of the formed crystals. These crystal properties determine the ability of the crystals to adhere to a surface and the hardness of the formed surface deposits. In fact, it is the mitigating effect that some impurities have on crystallization that can easily be exploited to

control scaling during RO desalination.

1.2.2 Scale control by antiscalant addition

There are several ways to prevent or minimize fouling by scale formation. An effective but economically undesirable way to reduce the risk of scaling is by limiting the product water recovery. Alternatively, the solution chemistry of the feed water can be altered by ion-exchange softening which can remove part of the scaling salt ions. Also, acidification of the feed water reduces the supersaturation of most sparingly soluble salts. Another technique that is currently under investigation is the implementation of intermediate chemical demineralization steps. However, the addition of organic impurities to the feed water that can effectively inhibit crystallization is and has been the predominant solution for scale control.

The presence of organic impurities can affect crystallization considerably. Impurities often adsorb selectively onto different crystal faces and retard their growth rates. However, a total face coverage with impurity is not necessary to induce growth retardation. Utilizing the classic Kossel model, three sites may be considered at which impurities may adsorb and hinder the movement of growth layers across the crystal faces; at a kink, at a step or on a face between steps (ledge). Kinks are energetically favourable sites for adsorption of solute ions and, therefore, can be considered as the active growth sites of a crystal. If impurity adsorption onto such kink sites is possible, growth inhibition occurs at very low impurity concentration in the solution. More impurity would be needed if adsorption to steps is preferred, while a much higher concentration is required if adsorption only occurs on ledges (Figure 1) (5).

Although it is believed that impurities can suppress crystal nucleation as well, a general explanation for this phenomenon cannot be given with so little quantitative evidence yet available. Most reported data on nucleation suppression by impurities are based on the delayed shower of nuclei that marks the onset of nucleation. However, nuclei are only being observed when they have grown to a detectable size. Therefore, depending on the detection method, a certain period of growth always preceded the moment when nuclei are

detected. Consequently, the suppression of nucleation by impurities may often be attributed primarily to growth inhibition as well.

Recently, evidence has been found for the existence of a two-step nucleation mechanism in which the formation of crystals starts with the formation of stable prenucleation ion clusters (6, 7). For calcium carbonate, aggregation of these clusters leads to the nucleation of amorphous nanoparticles (8). Possibly, antiscalants impair this cluster aggregation, suppressing nucleation.

Impurities designed to inhibit the crystallization of scaling salts, are called antiscalants. Antiscalants, primarily comprising polyelectrolytes such as phosphonates or polycarboxylates, typically prevent or retard scaling at relatively low concentrations (< 10 mg dm^{-3}), where the ion concentrations are stoichiometrically much higher.

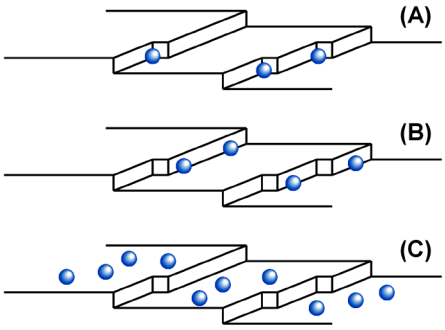

Figure 1. Sites for impurity adsorption on a growing crystal: (A) kink; (B) step; (C) ledge.

1.2.3 Phosphonate antiscalants

An important class of antiscalants comprises the phosphonates, which are the corresponding anions of phosphonic acids, which are compounds containing one or more $CPO(OH)_2$ groups. The name, structure, and abbreviation of some commonly used phosphonates are shown in Table 1. Phosphonates are very effective crystallization inhibitors and this distinctive feature has led to their extensive industrial use in cooling waters, oil fields and

desalination systems to inhibit scale formation. In RO desalination processes (Figure 2) the use of phosphonates prevents scaling, thus allowing for higher water product recoveries (4, 9). However, a major concern associated with their use in RO desalination is the high cost and environmental impacts associated with the discharge of membrane concentrates containing phosphonates. Although the direct toxicity to aquatic life of these phosphonates is low, they do affect the environment.

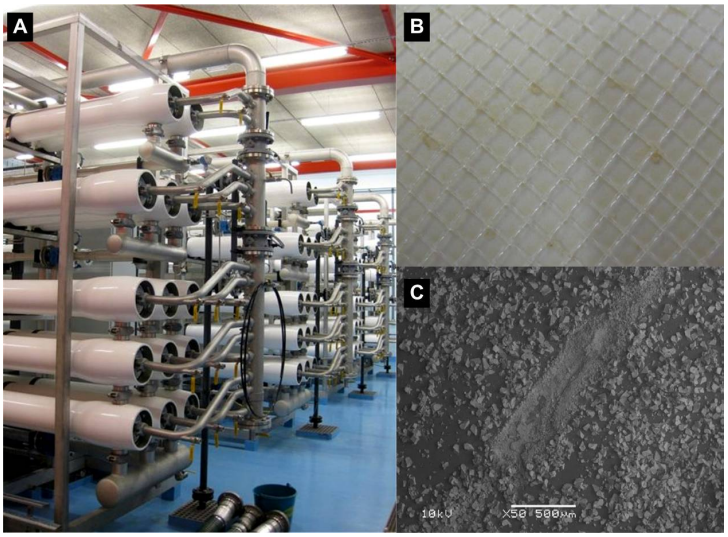

Figure 2. (A) A Dutch reverse osmosis desalination plant for the production of drinking water from brackish groundwater: (B) Example of $CaCO_3$ scaling on a membrane and feed spacer by inadequate antiscalant dosing; (C) Scanning electron microscopic picture of the precipitated $CaCO_3$ crystals.

Phosphonates contribute to the total phosphate content, and are considered to be compounds that promote eutrophication of the receiving surface water. Also, the phosphonates used as antiscalant have not been identified to occur naturally and may influence the transport of heavy metals in the marine environment. In addition, the reserves of the phosphate rock used to make phosphonates are finite, and concerns have been raised that they are in danger of exhaustion (10). Increased government awareness of this environmental problem rapidly imposes more and more severe restrictions on concentrate

disposal. Therefore, technologies are needed that can remove and recover these phosphonates from RO membrane concentrates.

Table 1. Abbreviation, name and chemical structures of three commonly used phosphonates.

Abbreviation	Name	Structure
HEDP	1-hydroxy(ethane-diphosphonic acid)	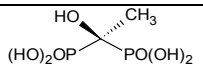
NTMP	Nitrilotris(methylene-phosphonic acid)	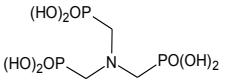
DTPMP	Diethylenetriamine penta(methylenephosphonic acid)	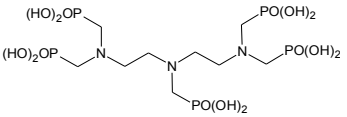

1.2.4 Concentrate treatment

As a result of the increasing awareness of the problems associated with concentrate disposal, the downstream treatment of concentrates is recently receiving considerable research interest in order to improve product water recoveries and reduce size and impact of concentrate streams before discharge. One of the promising approaches for concentrate disposal is through chemically induced precipitation of the dissolved salts, mostly calcium carbonate, followed by a solid/liquid separation step (11, 12). However, the presence of antiscalants in the concentrate inhibits the efficiency and effectiveness of such demineralization processes. Therefore, technologies are needed that remove or degrade the antiscalants before or during concentrate treatment. Antiscalant degradation can be achieved via chemical oxidation using ozone or peroxides (13). However, one of the main advantages of removing phosphonates above degrading them is the opportunity for their recovery and subsequent reuse. Therefore, the emphasis of this work lies primarily on the removal and recovery of phosphonates. Particularly, the use of adsorption technology has been recognized as a promising and fundamental approach to achieve these goals, due to its efficiency and its technical feasibility. Alternatively, if

demineralization of the concentrate is not a goal, and only the discharge of phosphonate antiscalants needs to be avoided, the use of phosphonates may be eliminated by replacing them by environmental friendly alternatives that are biodegradable and free of phosphorous. The performance of one such alternative antiscalant in inhibiting mineral crystallization has been addressed as well in this work.

1.2.5 Enhanced demineralization by ultrasound

The presence of antiscalants in membrane concentrates inhibits the efficiency and effectiveness of crystallization processes that may be used to demineralize concentrates. Therefore, removal or degradation of the antiscalants seems mandatory. It may, however, be possible to enhance the inhibited crystallization process in a different way, namely by ultrasound.

Ultrasound may be able to control the course of crystallization processes by the unique phenomenon of cavitation, which occurs when a liquid is exposed to high power ultrasound. Cavitation is the interaction of (acoustic) pressure waves with cavities (microbubbles), caused by the rupture of liquid in the negative pressure cycle (14).

If ultrasound can enhance the crystallization of scaling salts, it may also serve as an actuator for a sensor that can predict the scaling potential of a concentrate stream. Such a sensor may help in dosing antiscalants more efficiently to the RO desalination process, which allows for a minimum usage of antiscalants. Therefore, investigating the effect of ultrasound on the crystallization of scaling salts such as calcium carbonate is of great interest.

1.3 Research objectives

The effort of this research was primarily devoted to the following objectives:

- Develop a process for the removal and recovery of phosphonate antiscalants

- Address the effectiveness of environmental friendly alternative antiscalants that may replace phosphonates.

- Investigate the ability of ultrasound to enhance calcium carbonate crystallization and clarify the basic processes underlying this ability.

1.4 Outline

In **Chapter 2**, a comparison is made between the capacity of two anion exchange resins, activated carbon, and iron-coated waste filtration sand for adsorbing the phosphonate antiscalant nitrilotris(methylenephosphonic acid) (NTMP). The effect of pH, ionic strength, and the presence of competitive anions on the equilibrium adsorption are presented.

Chapter 3 describes the adsorption and desorption of NTMP from reverse osmosis membrane concentrate onto granular ferric hydroxide (GFH). Besides the adsorption equilibrium, the kinetics of adsorption is presented, which is described with different kinetic adsorption models. The role of calcium ions in the adsorption of phosphonate and the effect of sulfate are addressed as well.

In analogy with the work presented in Chapter 3, equilibrium and kinetic studies are carried out in **Chapter 4** to determine the sorption capacity and the rate of phosphonate uptake on the cheap alternative adsorbent identified in Chapter 2: iron-coated waste filtration sand.

Chapter 5 describes the use of GFH in a continuous operated packed-bed adsorption column. Together with the column breakthrough experiments, the recovery of the phosphonate antiscalant, following the regeneration of the saturated column is demonstrated.

In **Chapter 6**(*), the effect of ultrasonic irradiation on the crystallization of calcite is investigated. Calcite growth experiments are conducted while ultrasonic irradiation created cavitation bubbles throughout the suspension. In this way, changes in the rate of crystal growth are measured directly and can be related to the applied ultrasound.

In **Chapter 7**(*), the physical interaction of acoustic cavitation with suspended calcite crystals is visualized using high speed photography. The cavitation phenomena that are responsible for affecting the crystallization of calcite are identified and presented in this chapter.

The possibility to use ultrasound as a tool to enhance the desupersaturation of supersaturated calcium carbonate solutions (e.g., membrane concentrates) containing growth inhibitors is investigated in **Chapter 8**. Calcite growth experiments in the presence of the inhibitor NTMP are conducted in the presence and absence of ultrasonic irradiation. Both the physical and chemical effects that ultrasound has on crystals covered with phosphonate inhibitor are addressed.

In **Chapter 9**, a detailed study is presented in which the effectiveness of carboxymethyl inulin biopolymers in inhibiting calcium carbonate crystallization is compared to that of the phosphonates nitrilotris(methylenephosphonic acid) and 1-hydroxyethane-1,1-diphosphonate. The presented data is used to demonstrate whether these environmentally friendly antiscalants have the ability to replace the phosphonate antiscalants.

A general discussion and perspectives of the presented work is given in **Chapter 10**.

(*) *The work presented in Chapters 6 and 7 was conducted in close collaboration with Martijn Wagterveld. Both the author and Martijn Wagterveld contributed an equal share in the experimental work as well as the writing of these two chapters*.

1.5 References

(1) Gleick, P. H. *Water in Crisis: a Guide to the World's Fresh Water Resources*, Oxford University Press: New York, 1993.

(2) Vörösmarty, C. J.; Green, P.; Salisbury, J.; Lammers, R. B. Global water resources: vulnerability from climate change and population growth. *Science* **2000**, *289*, 284-288.

(3) Lattemann, S.; Kennedy, M. D.; Schippers, J. C.; Amy, G. S*ustainability Science and Engineering*, Elsevier, 2010, 7-39.

(4) Antony, A.; Low, J. H.; Gray, S.; Childress, A. E.; Le-Clech, P.; Leslie, G. Scale

formation and control in high pressure membrane water treatment systems: a review. *J. Membr. Sci.* **2011**, *383*, 1-16.

(5) Mullin, J. W. *Crystallization*, Elsevier Butterworth-Heinemann: Burlington, MA, 2001.

(6) Vekilov, P. G. The two-step mechanism of nucleation of crystals in solution *Nanoscale* **2010**, *2*, 2346-2357

(7) Gebauer, D.; Völkel, A.; Cölfen, H. Stable prenucleation calcium carbonate clusters. *Science* **2008**, *322*, 1819-1822.

(8) Pouget, M. E.; Bomans, P. H. H.; Goos, J. A. C. M.; Frederik, P. M.; de With, G.; Sommerdijk, N. A. J. M. The initial stages of template-controlled $CaCO_3$ formation revealed by cryo-TEM. *Science* **2009**, *323*, 1455-1258.

(9) Greenlee, L. F.; Lawler, D. F.; Freeman, B. D.; Marrot, B.; Moulin, P. Reverse osmosis desalination: water sources, technology, and today's challenges. *Water Res.* **2009**, *43*, 2317-2348.

(10) Cordell, D.; Drangert, J. -O.; White, S. The story of phosphorus: global food security and food for thought. *Global Environ. Change* **2009**, *19*, 292-305.

(11) Gabelich, C. J., Williams, M. D., Rahardianto, A., Franklin, J. C., Cohen, Y. High-recovery reverse osmosis desalination using intermediate chemical demineralization. *J. Membr. Sci.* **2007**, *301*, 131–141.

(12) Rahardianto, A.; McCool, B. C.; Cohen, Y. Accelerated desupersaturation of reverse osmosis concentrate by chemically-enhanced seeded precipitation. *Desalination* **2010**, *264*, 256-267.

(13) Greenlee, L. F.; Testa, F.; Lawler, D. F.; Freeman, B. D.; Moulin, P. Effect of antiscalant degradation on salt precipitation and solid/liquid separation of RO concentrate. *J. Membr. Sci.* 2011, 366, 48-61.

(14) Shah, Y. T.; Pandit, A. B.; Moholkar, V. S. *Cavitation Reaction Engineering*, Plenum Pub Corp, 1999.

2 ADSORPTIVE REMOVAL OF NITRILOTRIS(METHYLENEPHOSPHONIC ACID) ANTISCALANT FROM MEMBRANE CONCENTRATES BY IRON-COATED WASTE FILTRATION SAND

Iron-coated waste filtration sand was investigated as a low-cost adsorbent for the removal of nitrilotris(methylenephosphonic acid) (NTMP) from membrane concentrates. The adsorption of this phosphonate-based antiscalant on this material was measured and compared with two commercially available anion exchange resins and activated carbon. Comprehensive adsorption experiments were conducted in several synthetic concentrate solutions and in a concentrate collected from a full-scale nano-filtration brackish water desalination plant. The effect of pH, ionic strength and the presence of competitive anions on the equilibrium adsorption were investigated. The results showed that, in contrast to the anion exchange resins, the adsorption on coated filtration sand is not suppressed at increasing ionic strength and is much less affected by the competitive anions carbonate and sulfate. The adsorption decreased slightly when the pH was raised from 7.0 to 8.0. The adsorption isotherms in the real nano-filtration concentrate, measured in the concentration interval of 5 - 50 mg dm^{-1} NTMP, showed that the maximum adsorption capacity of coated filtration sand was 4.06 mg g^{-1}. The adsorption capacity per unit mass of the adsorbents at low NTMP concentration (12.5 mg dm^{-3}) followed the decreasing order Amberlite IRA-410 > coated filtration sand > Amberlite IRA-900 > Norit SAE Super. This demonstrates that the use of iron-coated waste filtration sand offers a promising means for the removal of NTMP from membrane concentrates.

This chapter has been published as:

Boels, L.; Tervahauta, T.; Witkamp, G. J. Adsorptive removal of nitrilotris(methylenephosphonic acid) antiscalant from membrane concentrates by iron-coated waste filtration sand. *J. Hazard. Mater.* **2010**, *182*, 855-862

2.1 Introduction

Phosphonates are extensively used in water treatment processes to inhibit scaling of sparingly soluble salts like calcium carbonates, calcium phosphates, sulfates, silicates and others (1-3). In membrane processes, the use of antiscalants allows for a higher water recovery (4). However, the discharge of a membrane concentrate, or waste brine, containing a phosphonate-based antiscalant can be problematic, especially in those cases where large surface water is absent (5). Phosphonates contribute to the total phosphate content, and are considered to be compounds that promote eutrophication of the receiving surface water (6). In addition, the phosphonates used as antiscalant are not identified to occur naturally (7) and, despite their resistance against degradation, release aminomethylphosphonic acid as a metabolite (8). Furthermore, their complexing ability might promote an undesirable remobilization of heavy metals. Removal of phosphonate-based antiscalants could also improve downstream concentrate treatment processes in which sparingly soluble salts are being removed. Recently, this downstream treatment of concentrates received considerable attention in order to improve water recoveries and reduce the size and impact of the concentrate stream before discharge (9-11).

A commonly used phosphonate is nitrilotris(methylenephosphonic acid) (NTMP), which is a very effective scale inhibitor (Figure 1) (7, 12). In general, antiscalants like NTMP are effectively used at relatively low concentrations (< 10 mg dm^{-3}) (1). Therefore, the use of adsorption technology could offer a cost effective way to remove NTMP from membrane concentrates. However, the specific salt content in membrane concentrates puts high demands on the adsorbent in terms of capacity and selectivity. Especially the presence of competitive anions and alkaline earth metal cations in nano-filtration brackish water concentrates may influence the adsorption of NTMP on the selected adsorbent markedly. A suitable adsorbent should be low-cost and exhibit a high adsorption capacity for NTMP at concentrations typically found in membrane concentrates.

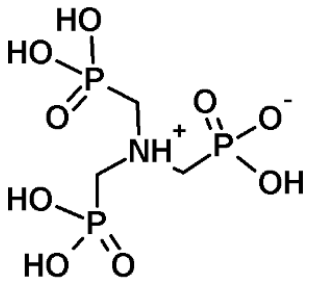

Figure 1. Chemical structure of nitrilotris(methylenephosphonic acid), NTMP.

Iron-coated filtration sand, can be considered to be low-cost because it is abundantly available as a waste by-product in the production of drinking water from groundwater (13). Aeration of groundwater in rapid sand filtration processes is often applied for the removal of iron and manganese, before the groundwater undergoes further treatment (e.g., membrane filtration) (14).

The presence of iron oxide in the outer shell of the coated filtration sand is the key in its applicability as an adsorbent for NTMP. Elaborated work on the adsorption of several phosphonates onto the iron oxide goethite was conducted by Nowack and Stone (15-17). Several applications of sand covered with iron oxides found in literature mainly comprise the adsorption of heavy metals (18-20), phosphates (21-23), and humic substances (19). However, the removal of phosphonate-based antiscalant by iron-coated filtration sand has not been addressed yet.

The aim of the present work is to investigate whether iron-coated filtration sand can be used for the removal of the phosphonate NTMP from membrane concentrates. The adsorption of NTMP on this low-cost waste material was compared with two commercial anion exchange resins and activated carbon. Equilibrium adsorption experiments were carried out in a range of synthetic concentrate solutions in order to evaluate the effect of ionic strength, the presence of competitive anions and pH on the adsorption process. In this way, the primary factors that may influence the adsorption performance in real membrane concentrates were investigated. Finally, the adsorption of

NTMP in a real brackish water nano-filtration (NF) concentrate was investigated.

2.2 Materials and methods

2.2.1 Materials

Nitrilotris(methylenephosphonic acid) (NTMP) was obtained from Fluka in its acid form with a purity of 99 %. Magnesium sulfate ($MgSO_4.7H_2O$), sodium bicarbonate ($NaHCO_3$), sodium chloride (NaCl), and potassium nitrate (KNO_3) were of analytical grade and were obtained from Boom (Meppel, The Netherlands). High quality Milli-Q water (resistivity > 18 MΩ cm) was used for preparation of the synthetic concentrate solutions.

The coated filtration sand used in this study was obtained from one of the largest drinking water companies in the Netherlands. The filtration sand was received wet. The particles were washed thoroughly with distilled water and subsequently dried under vacuum at room temperature for several days before use (humidity < 5 wt.%, determined by measuring the weight loss after additional drying of coated filtration sand samples at 105 °C under N_2-flow for 24 h). The same batch of coated filtration sand was used throughout all experiments. For comparison purposes, two commercially available anion exchange resins and activated carbon were also investigated as adsorbent for NTMP. Amberlite IRA-900 (Fluka) and Amberlite IRA-410 (Fluka), are strong anion exchange resins. The powdered activated carbon SAE Super (Norit), is mainly developed for wastewater treatment and is considered to be a strong multi-purpose adsorbent.

The NF-concentrate was collected from a full scale nano-filtration brackish water desalination plant (Dinxperlo, The Netherlands).

2.2.2 Methods

The coated filtration sand was characterized by scanning electron microscopy (SEM) (Jeol JSM-6480 LV) equipped with energy dispersive X-ray

spectroscopy (EDS) for elemental analysis (Noran). For comparison, both duplicate samples of an intact shell and a mixture of several powdered shells were analyzed. Furthermore, a known amount of shell material was completely dissolved in a 2 M HCl and 0.2 M $NH_2OH.HCl$ solution. After the chemical extraction, the dissolved metals were quantified using inductively-coupled plasma spectrometry (ICP) (Optima 3000XL, Perkin-Elmer) and the total organic content (TOC) of the coating was determined with a TOC analyzer (TOC-V CPH, Shimadzu). The characterization was done on triplicate samples. Further characterization of the shell was carried out using infrared spectroscopy (ATR-FTIR) (Shimadzu 4800) and powder X-ray diffraction (XRD) (Bruker D8 Advance). The specific surface area, the pore volume distribution and the average pore size of the adsorbents were measured with nitrogen adsorption (Micromeritics Tristar 3000).

The point of zero charge (PZC) was estimated using the mass titration technique proposed by Noh and Schwarz (24). Different masses of coated filtration sand (2.5 – 7.5 g dm^{-3}) were suspended in a 0.03 M KNO_3 solution and agitated for 24 h under N_2 atmosphere at 25 ± 0.1 °C until equilibrium pH was reached. By plotting equilibrium pH versus coated filtration sand mass, the PZC could be easily estimated from the appearance of a plateau in the curve.

The adsorption isotherms of NTMP at 25 °C on the coated filtration sand and the commercial adsorbents were measured in 6 different synthetic solutions and in NF-concentrate (Table 1). The pH was adjusted with a 0.05 M NaOH solution to the desired value. The adsorption experiments were conducted at different NTMP concentrations ranging from 5 to 300 mg dm^{-3}. The maximum NTMP concentration used in the NF-concentrate was 50 mg dm^{-3}, in order to prevent the precipitation of NTMP with calcium.

In a screw-capped flask, 0.1 g of adsorbent and 75 mL of NTMP solution were mixed and placed in a shaking bath (Julabo SW22) at 180 rpm and 25 °C. In preliminary experiments it was found that the minimum time required to attain equilibrium for the resins, activated carbon, and coated filtration sand, was 20, 16 and 72 h, respectively. To be absolutely certain that equilibrium was reached for all adsorbents, 120 h equilibrium time was used in all further

experiments. After the experiments, filtered samples of the solution were analyzed for the phosphonate content with ICP (25).

The fresh NF-concentrate was analyzed for its specific salt content with ICP and the TOC was measured. NTMP solutions with concentrations ranging from 5 to 50 mg dm^{-3} were prepared by dissolving solid NTMP in the NF-concentrate. After adjusting the pH of each solution, the adsorption experiments were subsequently initiated and conducted as described previously. Additional samples were taken after 18, 62 and 96 h, to enable the analysis of adsorption performance before $CaCO_3$ precipitation occurred. Also, aliquots of solution were filtered through a 0.2 μm filter, acidified, and analyzed with ICP for the calcium content. In this way the concentrate was monitored in time to identify any $CaCO_3$ precipitation.

2.3 Results and discussion

2.3.1 Characteristics of coated filtration sand

In Table 2, the elemental composition of the filtration sand's coating as determined with EDS and chemical extraction (CE) is shown. The main component of the coating was iron oxide. The percentage of iron oxide (Fe_2O_3) can be calculated from the average elemental composition to be 60 % (assuming that iron was present in its highest oxidation state). Also, a considerable amount of manganese was identified. The high carbon content in the coating is probably due to the presence of organic contaminations and/or carbonates. This was confirmed by the average TOC value of the coating, which was determined to be 58 mg g^{-1}. The results of the chemical extraction and the EDS analysis of the powdered sample are comparable. The EDS results of the intact shell, however, show a much lower manganese content. This indicates that the elemental composition of the coating is not homogeneous.

Table 1. Composition of the used NTMP solutions and the brackish water NF-concentrate.

Component	Units	Solution						NF-concentrate
		1	2	3	4	5	6	
Na^+	g dm^{-3}	<0.1	2.39	2.39	2.16	0.966	0.966	0.110
K^+	mg dm^{-3}	-	-	-	-	-	-	16.3
Ca^{2+}	g dm^{-3}	-	-	-	-	-	-	0.535
Mg^{2+}	mg dm^{-3}	0	0	0	72.9	72.9	72.9	42.7
Ba^{2+}	mg dm^{-3}	-	-	-	-	-	-	0.45
HCO_3^-	g dm^{-3}	0	0	0.610	0.610	0.610	0.610	1.21
SO_4^{2-}	g dm^{-3}	0	0	0	0.288	0.288	0.288	0.494
NO_3^-	mg dm^{-3}	-	-	-	-	-	-	20.5
Cl^-	g dm^{-3}	0	3.65	3.33	2.98	1.13	1.13	0.176
PO_4^{3-}	mg dm^{-3}	-	-	-	-	-	-	< 0.05
NTMP	mg dm^{-3}	5 - 300	5 - 300	5 - 300	5 - 300	5 - 300	5 - 300	5 - 50
IS[(a)]	M	< 0.01	0.10	0.10	0.10	0.05	0.05	0.074
pH	-	7.0	7.0	7.0	7.0	7.0	8.0	7.0[(b)] - 7.8[(c)]

(a) IS = Ionic strength; (b) pH of NF-concentrate adjusted to 7.0; (c) pH of NF-concentrate as received.

Table 2. Elemental composition of filtration sand coating determined with EDS analysis and CE-ICP.

Method	**Fe** (*wt %*)	**Mn** (*wt %*)	**Si** (*wt %*)	**P** (*wt %*)	**Ca** (*wt %*)	**O** (*wt %*)	**C** (*wt %*)
EDS shell	38.1	0.38	1.57	1.01	1.87	43.1	12.9
EDS powder	43.0	13.4	0.98	0.48	2.50	29.2	10.2
CE-ICP	41.1	9.4	-	-	-	-	-

The ATR-FTIR spectra and the X-ray diffraction pattern of the coated waste filtration sand (WFS) are shown in Figure 2. For comparison, the ATR-FTIR spectra taken from a pure ferrihydrite sample, synthesized according to literature (26), and the WFS sample is superimposed in this figure. The ATR-FTIR spectrum of the filtration sand coating (Figure 2A) can be assigned to poorly crystalline ferrihydrite, or so-called amorphous iron(III)-hydroxide because of the strong adsorption band with peaks at 551 and 692 cm^{-1}, which are also present in the spectra of the synthetic sample. The broad bands centered at 1586 and 3234 cm^{-1} can be assigned to the superposition of stretching vibrations of hydroxyl groups and water molecules. The band at 1375 cm^{-1} suggests the presence of carbonates in the sample. Because there is Si present in the coating (Table 2), the band at 944 cm^{-1} can be assigned to the stretching mode of Si-O-Fe groups (27).

The X-ray diffraction pattern (Figure 2B) also shows the presence of poorly crystalline 2-line ferrihydrite because of the two broad peaks at 38 and 72 ° (26). The origin of the peaks at 24 and 43 ° remains unclear, but they might indicate the presence of MnO_2 and other iron oxide phases like lepidocrocite and/or goethite. It is likely that the coating consisted of a mixture of poorly ordered iron oxides together with some impurities.

Nitrogen adsorption data showed that activated carbon SAE Super has the largest surface area of 998 $m^2 g^{-1}$, mainly composed of micropores (average pore size: 2.63 nm). Amberlite IRA-900, which has a macro reticular structure, has a surface area of 15.6 $m^2 g^{-1}$ and the largest average pore size (mesopores, average pore size: 33.9 nm). No porosity data could be obtained for Amberlite

IRA-410 because of its gel structure.

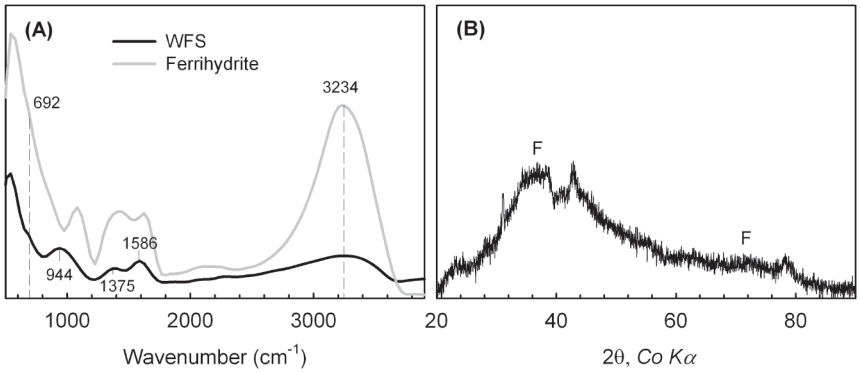

Figure 2. A) ATR-FTIR spectra of filtration sand coating (WFS) and pure ferrihydrite. B) XRD pattern of filtration sand coating, corresponding to low crystalline ferrihydrite (F).

The coated filtration sand had a relatively large specific surface area of 109 m^2 g^{-1} (average pore size: 4.13 nm), much larger than the nominal geometric surface area. This means that the coating is quite porous, which might be explained by the presence of ferrihydrite, as shown by ATR-FTIR and X-Ray analysis. Due to its amorphous nature, ferrihydrite is known to exhibit a large specific surface area. Also, it has been reported that the specific surface area of coated filtration sand increases with the development of coating (20, 28). The material under investigation had a well developed coating. The average weight ratio of shell/sand was determined to be 1.17. In other words, 54 weight % of the particle comprises the coating. SEM pictures of the coated filtration sand, shown in Fig. 3, show the presence of very rough/porous regions.

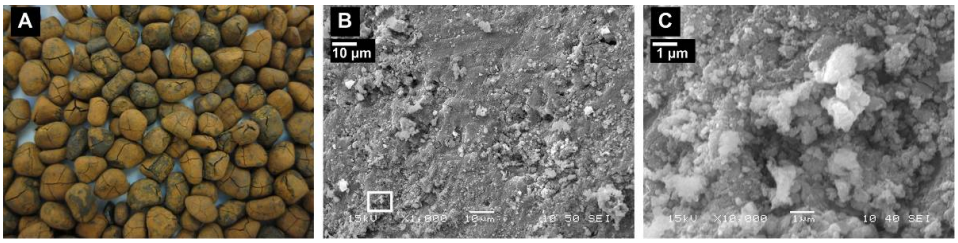

Figure 3. Dried coated filtration sand particles: (A) orange colored grains with a median size of 2.3 mm; (B) SEM picture of the coating magnified 1,000 times and (C) 10,000 times.

Ferrihydrite is probably the most effective iron oxide phase for the adsorption of NTMP, due to its large surface area. Therefore, the coating of filtration sand should preferably have a high iron content in the form of ferrihydrite. However, depending on the raw water quality and process conditions, the chemical composition of filtration sand coating can vary markedly (29). Nevertheless, ferrihydrite is most likely the primarily occurring phase at the conditions in a rapid sand filtration process, even though it is considered to be a transient metastable phase, because contaminants like phosphate, organic acids and Si, normally present in groundwater, cause a considerable stabilization of the ferrihydrite phase (30).

2.3.2 Adsorption isotherm description

The adsorption capacity is one of the most important parameters in adsorption processes, because it dictates the amount of adsorbent required. The relationship between the bulk aqueous phase equilibrium concentration of adsorbate and the amount adsorbed at constant temperature can be represented by adsorption isotherms. These adsorption isotherms, which reflect equilibria, can often be described by the Langmuir model (31). In this work, the adsorption isotherms will be correlated with the Langmuir model, because of its simplicity and easy incorporation in future design models. The Langmuir model is written as

$$\Gamma = \Gamma_{\max} \frac{K_{ads}[A]}{1 + K_{ads}[A]} \qquad (1)$$

where Γ_{max} is the maximum adsorption capacity ($mg\ g^{-1}$), Γ denotes the adsorbent capacity ($mg\ g^{-1}$) at equilibrium concentration [A] ($mg\ dm^{-3}$), and K_{ads} ($dm^3\ mg^{-1}$) is an experimentally determined equilibrium constant for the adsorption process. This constant can be related to the standard Gibbs free energy of adsorption, $\Delta G_{0,ads}$ ($kJ\ mol^{-1}$), by the following equation

$$\Delta G_{0,ads} = -\mathbf{R}T \ln(K_{ads}) \qquad (2)$$

where **R** is the gas universal constant (8.314 $J\ mol^{-1}\ K^{-1}$), and T (K) is the absolute temperature.

2.3.3 Effect of ionic strength

The adsorption isotherms of NTMP on coated filtration sand (WFS), Amberlite IRA-900, Amberlite IRA-410 and Norit SAE Super in pure water at neutral pH (solution 1) are shown in Figure 4A. The anion exchangers Amberlite IRA-410 and Amberlite IRA-900 exhibit the highest adsorption capacities of 144.2 and 116.2 mg g^{-1}, respectively, at an equilibrium concentration of 26 mg dm^{-3}. Their positive surface charge, provided as functional groups, seems to cause high capacities even at low NTMP concentrations. Much lower adsorption capacities are shown for coated filtration sand and activated carbon (13.4 & 7.92 mg g^{-1}, respectively). The initial slopes of the isotherms of filtration sand and activated carbon are much lower, which indicates a weaker interaction (i.e., low K_{ads}) with NTMP at these conditions. Figure 4B shows how the adsorption is affected by the presence of the background electrolyte NaCl. The presence of background electrolyte NaCl has a large influence on the adsorption isotherms of both anion exchange resins. At ionic strength 0.1 M, Amberlite IRA-410 showed the best adsorption, even though the basicity of the dimethylethanolamine functionality of Amberlite IRA-410 is slightly lower compared to the trimethylamine functionality of the Amberlite IRA-900. The adsorption of NTMP on coated filtration sand at higher ionic strength was not suppressed. On the contrary, it slightly improved. The weakest interaction of NTMP was observed with the hydrophobic carbon surface of SAE Super. The observed differences in the adsorption capacities (Table 3) are probably not related strongly to differences in pore size between the adsorbents. The diameter of an NTMP molecule lies around 0.5 nm (calculated from the molecular geometry. Software: SpartanModel 2006), which is far below the measured average pore sizes of the adsorbents.

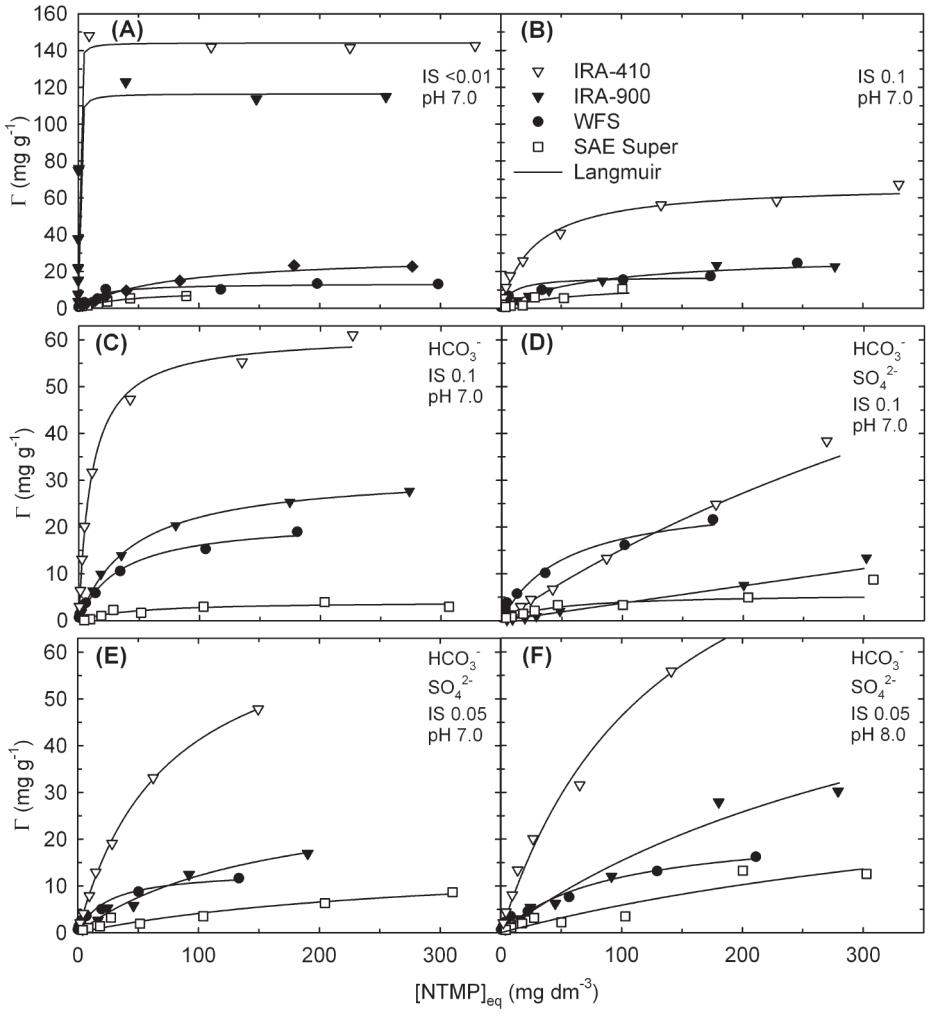

Figure 4. Adsorption isotherms of NTMP in the 6 synthetic concentrate solutions: (A) solution 1; (B) solution 2; (C) solution 3; (D) solution 4; (E) solution 5; (F) solution 6. The obtained Langmuir parameters for coated filtration sand (WFS) are shown in Table 3. In Appendix A, the Langmuir parameters for the other adsorbents are given in Table A1.

2.3.4 *Effect of competitive anions*

The adsorption of NTMP in membrane concentrate is different from that in pure water. The presence of competitive anions, for instance, may influence the adsorption of NTMP on the coated filtration sand markedly. According to Table 1, bicarbonate and sulfate are the major anions present in the NF-concentrate. Therefore, the effect of both competitive anions on the adsorption performance of coated filtration sand was investigated by measuring the adsorption isotherms of NTMP in the presence of carbonate (solution 3) and both carbonate and sulfate (solution 4). The adsorption isotherms of NTMP on the four adsorbents in solution 3 and 4 are shown in Figure 4. In the presence of carbonate (Figure 4C), the anion exchange resins and the coated filtration sand showed a similar adsorption compared to the adsorption in the absence of carbonate at equal ionic strength (Figure 4B). However, the equilibrium constant, K_{ads}, of NTMP adsorption, is lower and, therefore, the initial slopes of the isotherms are shallower. This means that at low NTMP concentration, the adsorption was interfered by the presence of carbonate ions. It seems that sulfate has a more profound interfering effect than carbonate, especially in the case of the anion exchange resins, where both the equilibrium constant and the maximum adsorption capacity are decreased strongly (Figure 4D). This interfering effect is less profound on the adsorption of NTMP on coated filtration sand and activated carbon, although both isotherms are slightly shallower. This indicates that the coated filtration sand exhibits a relatively high selectivity for the phosphonate functionalities in NTMP.

2.3.5 *Effect of pH*

The adsorption isotherms of NTMP at neutral pH (solution 5) and those measured at pH 8.0 (solution 6) are shown in Figure 4. The adsorption isotherms do not change significantly at pH 8.0, a value closer to the value of membrane concentrate. A small increase in adsorption occurs on both anion exchange resins. This increase might be related to the protonation level of NTMP, which can undergo numerous changes as a function of pH. When an additional proton becomes dissociated at pH 8.0 (32), the NTMP anion becomes

more negatively charged, which may promote a stronger adsorption. The slope of the isotherm of coated filtration sand is lower, which indicates a weaker interaction (i.e., lower K_{ads}) with NTMP at pH 8.0. Possibly, the surface charge of the filtration sand's coating at pH 8.0 was less beneficial for NTMP adsorption, because the magnitude of the positive surface charge decreases with the increase in pH. The PZC of the coated filtration sand was estimated to be at pH 8.2. This indicates that the surface charge was much closer to zero at pH 8.0, which translated into a lower adsorption. In both solutions, the amount of background NaCl was reduced such that it would yield an ionic strength of 0.05 M (Table 1). At lower ionic strength, the anion exchange resins perform better, whereas the coated filtration sand and activated carbon show a slight decrease in adsorption. This is in line with previous observations (Section 2.3).

2.3.6 Adsorption of NTMP in NF-concentrate

The adsorption tests conducted in NF-concentrate were subject to $CaCO_3$ precipitation before equilibrium was reached, especially at pH 7.8, because the supersaturation ratio, S, with respect to $CaCO_3$ in the concentrate was very high. For $CaCO_3$, S, the driving force for precipitation, is best expressed in terms of the solubility product (33)

$$S = (IAP / K_{sol})^{1/v} \quad (3)$$

where IAP (-) is the ion activity product, K_{sol} (-) is the solubility product, and v (-) is the number of ions in the formula unit. The relative $CaCO_3$ supersaturation (S - 1) in the concentrate was calculated to be 7.0 (Software: Visual Minteq v2.53, model: Davies). Therefore, precipitation of this salt was inevitable on the long term. If precipitation occurs, an additional surface for NTMP adsorption becomes available, and the measurement of a true equilibrium adsorption on the adsorbent becomes impossible.

At pH 7.0, the relative $CaCO_3$ supersaturation is much lower and calculated to be 2.0, and therefore, less precipitation was observed. For the anion exchange resins, precipitation was observed at 62 h of adsorption as was

evident from the turbid NTMP solutions and decreased Ca^{2+} concentration. Therefore, only the adsorption after 18 h for both resins could be measured (Figure 5B), which was close to the 20 h needed to attain equilibrium. The concentrate solutions in the bottles containing coated filtration sand and activated carbon were less susceptible for precipitation on the long term. Therefore, the adsorption isotherms at equilibrium could be measured at t = 120 h, which is much longer than the residence times in large-scale adsorption columns (Figure 5A). To illustrate the effect of $CaCO_3$ precipitation on the adsorption isotherm, the data points for activated carbon at pH 7.8 are also included in this figure.

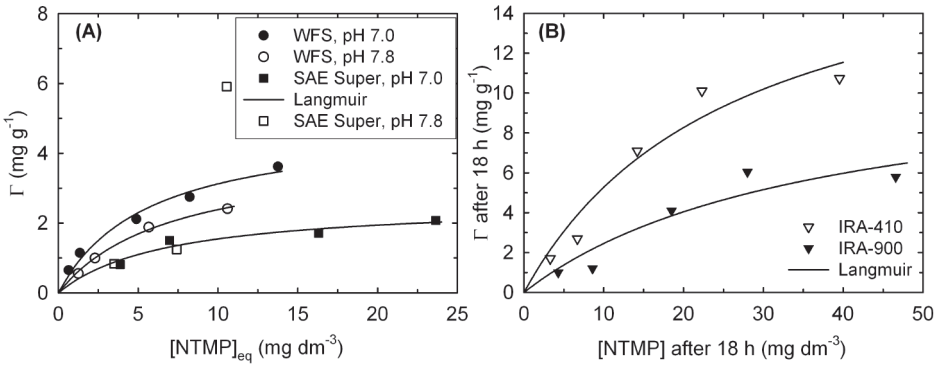

Figure 5. Adsorption of NTMP in NF-concentrate: (A) on coated filtration sand (WFS) and SAE Super at pH 7.0 and 7.8; (B) on the anion exchange resins after 18 h (close to equilibrium) at pH 7.0. The obtained Langmuir parameters are shown in Tables 3 and A1 (Appendix A).

It seems that in NF-concentrate, the maximum adsorption capacity of each adsorbent is much less compared to the values found in the synthetic solutions (see Table 3 & Table A1 in Appendix A). It was shown that sulfate interferes with the adsorption of NTMP (Section 2.4). According to Table 1, the sulfate content is almost a factor two higher compared to the used synthetic solutions. In addition, the presence of NOM (naturally occurring materials) like humic acids, are likely to compete with NTMP for the available adsorption sites, because of the affinity of the iron hydroxyl groups for NOM adsorption. This idea was supported by the relatively high TOC value of the concentrate,

which was measured to be 46 mg dm^{-3}. Also, organic contaminations already present in the filtration sand's coating (TOC 58 mg g^{-1}) might diminish NTMP adsorption. Nevertheless, the equilibrium adsorption of the coated filtration sand at low NTMP concentrations is higher compared to activated carbon (Figure 5A), and the resins after 18 h (Figure 5B). A possible explanation could be that the presence of alkaline earth metals, especially Ca^{2+}, enhances the adsorption process onto the iron oxide. In case of goethite, it was shown that when Ca^{2+} concentration is present in excess of the phosphonate concentration, considerable increase in adsorption occurs (15). A similar phenomenon might play a role in the adsorption of NTMP on ferrihydrite, because excess Ca^{2+} is present in the NF-concentrate (Table 1). As expected, the adsorption of NTMP on coated filtration sand is lower at pH 7.8 (see Section 3.5).

The adsorption capacities at NTMP concentrations of 12.5 mg dm^{-3}, the parameters obtained from the Langmuir fit, the maximum surface coverage, Λ_{max} ($\mu g\ m^{-2}$), and the free energy of adsorption calculated for coated filtration sand are shown in Table 3 (see Table A1 in Appendix A for data on the other adsorbents). At an NTMP concentration of 12.5 mg dm^{-3}, typically found in membrane concentrates, the adsorption performance of coated filtration sand in solutions matrices 4 - 6 and NF-concentrate is better compared to Amberlite IRA-900 and SAE-Super. Although Amberlite IRA-410 shows the best performance, it is a relatively expensive resin that cannot compete with iron-coated waste filtration sand in terms of the amount of NTMP adsorbed per unit cost of material. Even though the maximum adsorption capacity is much less in the NF-concentrate, the adsorption capacity of coated filtration sand at 12.5 mg dm^{-3} is comparable to those measured in solutions 5 and 6 (Table 3).

The Langmuir model gives an acceptable description of the experimental data, as can be seen from the correlation coefficient R^2. The maximum surface coverage was calculated for the coating only by using the weight factor 0.54 (Section 2.1). The values for the surface coverage in the synthetic solution are relatively high, and it can be calculated that 0.5 - 0.9 NTMP molecules (diameter ~0.5 nm) can be adsorbed on the coating in the synthetic solutions, while only 0.15 NTMP molecules per nm^2 are adsorbed in NF-concentrate. This indicates

that in NF-concentrate, competition plays a pivotal role in the maximum attainable adsorption capacity.

Table 3. Parameters obtained from the Langmuir fit of the isotherms for coated filtration sand.

Parameter	Solution						NF-concentrate	
	1	2	3	4	5	6	pH 7.0	pH 7.8
Γ_{max} *(mg g^{-1})*	13.4	17.0	21.6	26.6	21.0	22.6	4.88	4.06
$\Gamma_{12.5}$ *(mg g^{-1})*	6.27	9.03	5.78	5.13	3.37	2.76	3.67	2.60
Λ_{max} *(μg m^{-2})*(a)	229	290	369	454	358	386	83.3	69.3
K_{ads} *(dm^3 g^{-1})*	0.070	0.090	0.029	0.019	0.015	0.011	0.178	0.143
$\Delta G_{0,ads}$ *(kJ mol^{-1})*	-10.5	-11.2	-8.35	-7.30	-6.71	-5.94	-12.8	-12.3
R^2 *(-)*	0.938	0.950	0.986	0.976	0.931	0.969	0.970	0.993

(a) Maximum surface coverage of the coating. Value calculated by multiplying the maximum surface coverage of the coated filtration sand by 1/0.54.

The estimated values for the standard Gibbs free energy of adsorption, calculated from the equilibrium constant K_{ads} (Section 2.2), are relatively low, indicating that physisorption processes i.e., Van der Waals forces and hydrogen bonding, are dominating.

2.4 Conclusions

It was demonstrated that iron-coated waste filtration sand is a promising adsorbent for the removal of nitrilotris(methylenephosphonic acid) (NTMP) from membrane concentrates, due to the good adsorption performance at low NTMP concentrations and its low-cost. The adsorption of NTMP on coated filtration sand was measured in different synthetic concentrate solutions and in NF-concentrate and compared to the adsorption on activated carbon and two anion exchange resins. In contrast to the anion exchange resins, a higher ionic strength did not suppress the adsorption of NTMP on coated filtration sand and activated carbon. Furthermore, the interfering effect of the competitive polyanions carbonate and sulfate is less profound on the adsorption of NTMP on coated filtration sand. The adsorption of NTMP on coated filtration sand decreased when the pH was raised from 7.0 to 8.0 due to a lower positive

surface charge of the coating. In NF-concentrate, coated filtration sand showed a lower maximum adsorption capacity compared to the synthetic solutions due to the different solution composition and the presence of competitive organic compounds. At low NTMP concentrations (12.5 mg dm^{-3}), however, the adsorption capacity of coated filtration sand in NF-concentrate was not lower compared to the synthetic solutions. The adsorption capacity of the adsorbents at an NTMP concentration of 12.5 mg dm^{-3} in solutions 4, 5, 6 and the NF-concentrate, followed the decreasing order Amberlite IRA-410 > coated filtration sand > Amberlite IRA-900 > Norit SAE Super.

2.5 Acknowledgements

This work was performed in the TTIW-cooperation framework of Wetsus, Centre of Excellence for Sustainable Water Technology (www.wetsus.nl). Wetsus is funded by the Dutch Ministry of Economic Affairs, the European Union Regional Development Fund, the Province of Fryslân, the City of Leeuwarden and the EZ/Kompas program of "Samenwerkingsverband Noord-Nederland". The authors like to thank the participants of the research theme "Concentrates" for the discussions and their financial support. We would especially like to thank Kamuran Yasadi for the ATR-FTIR analysis, Martijn Wagterveld for the SEM analysis, Ruud Hendrikx for the X-ray analysis, and Michel van den Brink for the ICP analysis. Finally, we would like to thank Ron Jong from Vitens for the supply of coated filtration sand and NF-concentrate.

2.6 References

(1) Greenlee, L. F.; Lawler, D. F.; Freeman, B. D.; Marrot, B.; Moulin, P. Reverse osmosis desalination: water sources, technology, and today's challenges. *Water Res.* **2009**, *43*, 2317-2348.

(2) Gill, J. S. A novel inhibitor for scale control in water desalination. *Desalination* **1999**, *124*, 43-50.

(3) Gledhill, W. E.; Feijtel, T. C. J. *The Handbook of Environmental Chemistry*, Heidelberg Springer: Berlin, Germany, 1992.

(4) Hasson, D.; Drak, A.; Semiat, R. Inception of $CaSO_4$ scaling on RO membranes at various water recovery levels. *Desalination* **2001**, *139*, 73-81.

(5) Nederlof, M. M.; van Paassen, J. A. M.; Jong, R. Nanofiltration concentrate disposal: experiences in The Netherlands. *Desalination* **2005**, *178*, 303-312.

(6) Correll, D. L. The role of phosphorus in the eutrophication of receiving waters: a review. *J. Environ. Qual.* **1998**, *27*, 261-266.

(7) Jaworska, J.; Van Genderen-Takken, H.; Hanstveit, A.; van de Plassehe, E.; Feijtel, T. Environmental risk assessment of phosphonates, used in domestic laundry and cleaning agents in The Netherlands. *Chemosphere* **2002**, *47*, 655-665.

(8) Steber, J.; Wierich, P. Properties of aminotris(methylenephosphonate) affecting its environmental fate, degradability, sludge adsorption, mobility in soils and bioconcentration. *Chemosphere* **1987**, *16*, 1323-1337.

(9) Gabelich, C. J., Williams, M. D., Rahardianto, A., Franklin, J. C., Cohen, Y. High-recovery reverse osmosis desalination using intermediate chemical demineralization. *J. Membr. Sci.* **2007**, *301*, 131–141.

(10) Greenlee, L. F.; Testa, F.; Lawler, D. F.; Freeman, B. D.; Moulin, P. The effect of antiscalant addition on calcium carbonate precipitation for a simplified synthetic brackish water reverse osmosis concentrate. *Water Res.* **2010**, *44*, 2957-2969.

(11) Rahardianto, A.; Gao, J.; Gabelich, C. J.; Williams, M. D.; Cohen, Y. High recovery membrane desalting of low-salinity brackish water: integration of accelerated precipitation softening with membrane RO. *J. Membr. Sci.* **2007**, *289*, 123-137.

(12) Demadis, K. D. Chemistry of organophosphonate scale inhibitors, part 4: stability of amino-tris-(methylene phosphonate) towards degradation by oxidizing biocides. *Phosphorus Sulfur* **2006**, *181*, 167-176.

(13) Sharma, S. K. *Adsorptive Iron Removal from Groundwater*, Swets & Zeitlinger B.V.: Lisse, The Netherlands, 2001.

(14) Sharma, S. K.; Petrusevski, B.; Schippers, J. C. Biological iron removal from groundwater: a review. *J. Water Supply Res. T.* **2005**, *54*, 239-247.

(15) Nowack, B.; Stone, A. T. The influence of metal ions on the adsorption of phosphonates onto goethite. *Environ. Sci. Technol.* **1999**, *33*, 3627-3633.

(16) Nowack, B.; Stone, A. T. Adsorption of phosphonates onto the goethite-water interface. *J. Colloid Interface Sci.* **1999**, *214*, 20-30.

(17) Nowack, B.; Stone, A. T. Competitive adsorption of phosphate and phosphonates onto goethite. *Water Res.* **2006**, *40*, 2201-2209.

(18) Benjamin, M. M.; Sletten, R. S.; Bailey, R. P.; Bennett, T. Sorption and filtration of metals using iron-oxide-coated sand. *Water Res.* **1996**, *30*, 2609-2620.

(19) Lai, C. H.; Chen, C. Y. Removal of metal ions and humic acid from water by iron-coated filter media. *Chemosphere* **2001**, *44*, 1177-1184.

(20) Lo, S. L.; Jeng, H. T.; Lai, C. H. Characteristics and adsorption properties of iron-coated sand. *Water Sci. Technol.* **1997**, *35*, 63-70.

(21) Boujelben, N.; Bouzid, J.; Elouear, Z.; Feki, A.; Jamoussi, F.; Montiel, A. Phosphorus removal from aqueous solution using iron coated natural and engineered sorbents. *J. Hazard. Mater.* **2008**, *151*, 103-110.

(22) Mezenner, N. Y.; Bensmaili, A. Kinetics and thermodynamic study of phosphate adsorption on iron hydroxide-eggshell waste. *Chem. Eng. J.* **2009**, *147*, 87-96.

(23) Zeng, L.; Li, X. M.; Liu, J. D. Adsorptive removal of phosphate from aqueous solutions using iron oxide tailings. *Water Res.* **2004**, *38*, 1318-1326.

(24) Noh, J. S.; Schwarz, J. A. Estimation of the point of zero charge of simple oxides by mass titration. *J. Colloid Interface Sci.* **1989**, *130*, 157-164.

(25) Ibrahim, H.; Issa, Y. M.; Kamal, R. The determination of phosphonate base scale inhibitors in brines by plasma spectrometry. *Mikrochim. Acta* **1992**, *109*, 201-209.

(26) Schwertmann, U., Cornell, R.M. *Iron Oxides in the Laboratory*, Wiley-VCH Verlag GmbH: Weinheim, Germany, 2000.

(27) Carlson, L.; Schwertmann, U. Natural ferrihydrites in surface deposits from Finland and their association with silica. *Geochim. Cosmochim. Acta* **1981**, *45*, 421-429.

(28) Chang, Y. J.; Li, C. W.; Benjamin, M. M. Iron oxide-coated media for NOM sorption and particulate filtration. *J. Am. Water Works Ass.* **1997**, *89*, 100-113.

(29) Sharma, S. K., Petrusevski, B. and Schippers, J. C. Characterisation of coated sand from iron removal plants. *J. Water Sci. Technol.: Water Supply.* **2002**, *2*, 247-257.

(30) Schwertmann, U.; Fechter, H. The point of zero charge of natural and synthetic ferrihydrites and its relation to adsorbed silicate. *Clay Miner.* **1982**, *17*, 471-476.

(31) Stumm, W., Morgan, J.J. *Aquatic Chemistry: Chemical Equilibria and Rates in Natural Waters*, NY. John Wiley & Sons, Inc.: New York, 1996.

(32) Kan, A. T.; Fu, G. M.; Tomson, M. B. Adsorption and precipitation of an aminoalkylphosphonate onto calcite. *J. Colloid Interface Sci.* **2005**, *281*, 275-284.

(33) Mullin, J. W. *Crystallization*, Elsevier Butterworth-Heinemann: Burlington, MA, 2001.

ADSORPTION OF PHOSPHONATE ANTISCALANT FROM REVERSE OSMOSIS MEMBRANE CONCENTRATE ONTO GRANULAR FERRIC HYDROXIDE

3

Adsorptive removal of antiscalants offers a promising way to improve current reverse osmosis (RO) concentrate treatment processes and enables the reuse of the antiscalant in the RO desalination process. This work investigates the adsorption and desorption of the phosphonate antiscalant nitrilotris(methylenephosphonic acid) (NTMP) from RO membrane concentrate onto granular ferric hydroxide (GFH), a material that consists predominantly of akaganéite. The kinetics of the adsorption of NTMP onto GFH was predicted fairly well with two models that consider either combined film-pore or combined film-surface diffusion as the main mechanism for mass transport. It is also demonstrated that NTMP is preferentially adsorbed over sulfate by GFH at pH 7.85. The presence of calcium causes a transformation in the equilibrium adsorption isotherm from a Langmuir type to a Freundlich type with much higher adsorption capacities. Furthermore, calcium also increases the rate of adsorption substantially. GFH is reusable after regeneration with sodium hydroxide solution, indicating that NTMP can be potentially recovered from the RO concentrate. This work shows that GFH is a promising adsorbent for the removal and recovery of NTMP antiscalant from RO membrane concentrates.

This chapter has been published as:

Boels, L.; Keesman, K. J.; Witkamp, G. J. Adsorption of phosphonate antiscalant from reverse osmosis membrane concentrate onto granular ferric hydroxide. *Environ. Sci. & Technol*. **2012**, *46*, 9638-9645.

3.1 Introduction

Phosphonates are the corresponding anions of phosphonic acids, which are compounds containing one or more $CPO(OH)_2$ groups. Phosphonates are used in many applications due to their excellent chelating properties. For example, in the pulp, paper, and textile industry, they are used to bind heavy metals in bleaching solutions to avoid peroxide inactivation. They are also used as dispersion and corrosion-inhibiting agents for the prevention of copper and iron oxide deposits (1, 2).

Phosphonates are not only excellent chelating agents but also very effective inhibitors of mineral precipitation and growth (3-5). This distinctive feature has led to the extensive industrial use of phosphonates as antiscalants in cooling waters, oil fields, and desalination systems to inhibit scale formation (e.g., calcium carbonate or barium sulfate precipitation). The worldwide consumption of phosphonates in 1998 was 56,000 t, and the consumption in Europe in 1999 was 16,000 t (2).

In reverse osmosis (RO) desalination processes, the use of phosphonates prevents scaling, thus allowing for a higher product water recovery (6-11). However, a major concern associated with their use in RO desalination is the high cost and environmental impacts associated with the discharge of the membrane concentrate or waste brine containing phosphonates (12-18). Phosphonates contribute to the total phosphorus content and are considered to be compounds that promote eutrophication of the receiving surface water (19). In addition, the phosphonates used as antiscalants have not been identified to occur naturally and may influence the transport of heavy metals in the marine environment. Increased government awareness of this environmental problem rapidly imposes more and more severe restrictions on concentrate disposal.

As a result, the downstream treatment of concentrates is recently receiving considerable research interest to improve product water recoveries and reduce the size and impact of concentrate streams before discharge (20-23). One approach is through chemically induced precipitation of the dissolved salts followed by a solid/liquid separation step. However, the presence of antiscalants in the concentrate affects the efficiency of the demineralization

process even at high supersaturation levels (20, 21) and can reduce the precipitate particle size, which in turn presents issues during the separation of the precipitated salts (22).

One way to overcome these problems is by degrading the antiscalants via (chemical) oxidation processes (23, 24) or by using cyanobacteria (25). Also, the addition of polyaluminium chloride as an antiscalant scavenger has been reported to improve concentrate desupersaturation (26).

Adsorptive removal of antiscalants prior to the salt precipitation process may be a promising alternative solution for concentrate treatment. The absence of antiscalants enhances the demineralization process and reduces the use of crystallization agents such as hydrated lime. Most importantly, by adsorption, the chemical structure of the phosphonate can be preserved, which enables the reuse of the phosphonate as an antiscalant in the RO process.

The objective of this study is to investigate the adsorption and desorption of the phosphonate antiscalant nitrilotris(methylenephosphonic acid) (NTMP) from RO membrane concentrate onto granular ferric hydroxide (GFH). Both equilibrium and kinetic studies are carried out to determine the sorption capacity and the rate of NTMP uptake for GFH. The role of calcium ions in phosphonate adsorption and the competitive adsorption of sulfate are addressed as well. For the future design of continuously operated adsorbers, this work aims at modeling the adsorption equilibrium and kinetics with two models for intraparticle diffusion.

3.2 Materials and methods

3.2.1 Adsorbent

Commercially available granular ferric hydroxide (GFH) was obtained from GEH Wasserchemie (Osnabrück). GFH consists predominantly of the chloride-bearing iron oxy-hydroxide β-FeOOH, or akaganéite (27), and was originally developed for arsenic removal (28). The GFH material was sieved wet to 0.8 - 2.0 mm from the size supplied (0.2 – 2.0 mm) to give a more uniform sample size. The water content was determined to be 44.5 ± 1.4 %. All results are

presented on a dry mass basis (drying at 105 °C for 24 h).

The specific surface area and the pore volume of GFH were measured with nitrogen adsorption (Micromeritics Tristar 3000) on six replicate samples. The surface and structure of the adsorbent were further characterized by scanning electron microscopy (Jeol JSM-6480 LV) and Raman spectroscopy (Horiba/Jobin Yvon, Labram HR L/2/719)

3.2.2 Synthetic RO concentrate

The composition of the water used for the adsorption experiments was based on that of concentrates produced by brackish water RO membrane filtration installations. A simplified water data set was chosen to make synthetic RO concentrate in the laboratory, in which only the major ions were added: calcium, carbonate, sodium, and chloride. This simplified synthetic concentrate also allowed investigation of the effect of sulfate, which was added in some experiments. In experiments where the effect of calcium was investigated, the ionic strength was kept constant by adding NaCl. The synthetic concentrate solutions were prepared by the simultaneous addition of 0.5 dm^3 of a 12 mM $CaCl_2.2H_2O$ solution and 0.5 dm^3 of a 28 mM $NaHCO_3$ solution containing the phosphonate antiscalant NTMP. In this way, a metastable supersaturated $CaCO_3$ solution was obtained with an ionic strength of 0.03 M and a pH of 7.85 ± 0.02.

All solutions were prepared using deionized water. The salts used in this study were of analytical grade and were obtained from VWR. NTMP was obtained from Sigma-Aldrich in its acid form with a purity of > 97 %.

3.2.3 Batch adsorption experiments

Batch adsorption experiments were conducted in a double-walled thermostated (297.5 ± 0.5 K) glass reactor equipped with a pitched blade turbine impeller and four baffles. The adsorbent particles were put inside three baskets that were affixed to the stirrer shaft to permit good liquid-solid contact without adsorbent attrition. Immediately after the calcium and carbonate solutions were mixed, the measurements were started by contacting the baskets into the 1 dm^3 solution and starting the stirrer at 350 rpm. This stirring speed was high enough

for external mass transfer resistance to be nearly constant.

The pH was measured continuously. The presence of bicarbonate in the synthetic concentrate ensured a constant solution pH throughout the adsorption experiments. However, some minor adjustments were necessary with a diluted base to keep the pH at the desired level of 7.85 ± 0.02 at the highest employed masses of adsorbent. Aliquots of solution were removed periodically with a syringe, filtered by a 0.45 μm filter, diluted, and analyzed for the phosphorus content with inductively coupled plasma (ICP) spectrometry (Optima 3000XL, Perkin-Elmer) (29). To obtain optimal precision and accuracy during ICP analysis, yttrium was employed as an internal standard to correct for nonspectral interferences from the solution matrix (accuracy correlation curve < 5 %). The employed initial NTMP concentration and adsorbent mass were in the range of 10.2×10^{-3} - 25.4×10^{-3} kg m^{-3} and 2.6×10^{-3} - 6.2×10^{-3} kg, respectively.

3.2.4 Adsorption isotherms

Equilibrium adsorption isotherms were obtained by addition of different amounts of powdered adsorbent to 100 mL of synthetic concentrate solution containing 30 mg dm^{-3} NTMP. The suspensions were stirred vigorously for 24 h in screw-capped flasks at 297.5 ± 0.5 K. The presence of bicarbonate in the synthetic concentrate solutions ensured a constant solution pH of 7.85 ± 0.02. The phosphorus content was quantified as described above. Also, the calcium content was measured using ICP to validate the absence of $CaCO_3$ and/or Ca^{2+} - NTMP precipitation. In one experiment where sulfate was present in the synthetic concentrate, ion chromatography (761 compact ion chromatograph, Metrohm, Switzerland) was used to quantify the sulfate content.

3.2.5 Adsorbent regeneration

After the adsorption step, the synthetic concentrate solution was replaced by 1 dm^3 of a 0.1 M NaOH solution, and stirring was continued at 350 rpm. Following the desorption step in NaOH, the particles were washed twice in 1 dm^3 of deionized water for 4 h.

3.2.6 Numerical modeling

The models for intraparticle diffusion were numerically solved using Matlab's (version R2010b) built-in pdepe solver, which converts the partial differential equations to ordinary differential equations using a second-order spatial discretization method. A response surface methodology (30) was employed to find the combination of external film mass transfer coefficient and effective diffusivity that gave the minimum sum of squares of the residuals between the experimental data and the theoretical adsorbed amount profiles. This method allows for a good understanding of the relation between both parameters, because in the prior parameter domain, both the true minimum and any possible local minima are visible. In addition, the sensitivity of both parameters was analyzed by varying each parameter separately by ±10% of their optimum value and quantifying the change in model output. This is known as a one-at-a-time sensitivity analysis. From this analysis the standard deviations of the parameter estimates have been calculated using standard statistical techniques (31). The Matlab computer codes are available in Appendix B.

3.3 Results and discussion

3.3.1 Physical properties GFH adsorbent

The surface of GFH appears to be porous (Figure 1 A). According to the nitrogen adsorption measurements, the specific Brunauer-Emmett-Teller (BET) (32) surface area and the pore volume of the adsorbent were 289.3 ± 8.7 $m^2 g^{-1}$ and 0.33 ± 0.01 $cm^3 g^{-1}$, respectively. The measurements also revealed that GFH contains both micropores and mesopores and that the measured pore size distribution corresponds well with the literature; i.e., 97 % of the pores in GFH have a diameter below 4.5 nm (33). The average particle radius, R, was determined to be 0.62×10^{-3} m and the apparent particle density, ρ_p, was 1115 kg m^{-3}. From the values of the apparent particle density and the pore volume, the porosity, ε_p, of the adsorbent was calculated to be 0.37. The Raman spectrum (Figure 1 B) confirmed that the GFH adsorbent consists predominantly of

akaganéite (34).

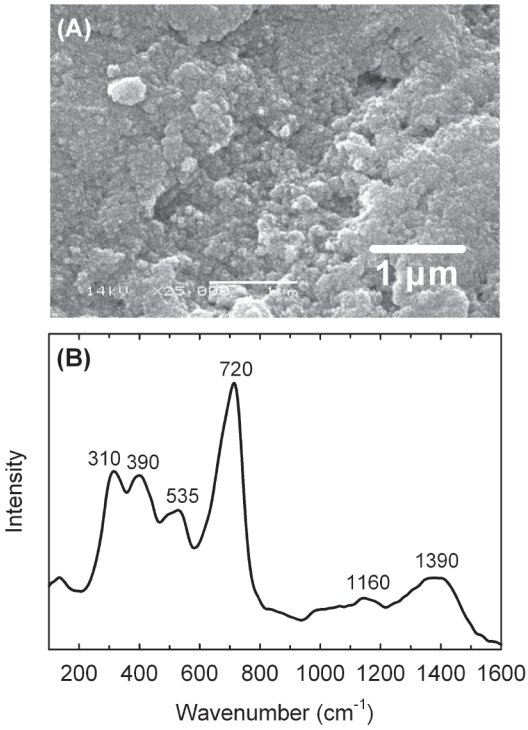

Figure 1. (A) SEM picture of the GFH particle surface showing that the adsorbent has a porous structure; (B) Raman spectrum (λ = 532 nm, laser power at sample 50 µW, acquisition time 60 min) of GHF showing characteristic bands for akaganéite.

3.3.2 Equilibrium adsorption

The equilibrium for the adsorption of NTMP from the synthetic RO membrane concentrate onto GFH may be described by one of the many equilibrium isotherm models available (35). The two best known isotherm models are the Langmuir and Freundlich isotherms represented by eqs 1 and 2,

$$q = \frac{q_{\max} k_L c_{eq}}{1 + k_L c_{eq}} \quad (1)$$

$$q = a_F c_{eq}^{n} \quad (2)$$

respectively, where q ($kg\ kg^{-1}$) is the amount adsorbed at the equilibrium concentration, c_{eq} ($kg\ m^{-3}$), and q_{max} ($kg\ kg^{-1}$) is the maximum adsorption capacity. The parameters k_L ($m^3\ kg^{-1}$), a_F ($kg\ kg^{-1}\ [m^3\ kg^{-1}]^n$), and n (-) can be determined by fitting the experimental data. The adsorption isotherms could not be adequately described by the Langmuir equation when calcium was present (Table 1, Figure 3A). The empirical Freundlich equation, however, can describe the equilibrium correlation satisfactorily, although the surface density of NTMP (approximately 1.2 molecules/nm^2) does not exceed the monolayer coverage yet. The Langmuir and Freundlich parameters as a function of the molar Ca^{2+} : NTMP ratio are listed in Table 1.

Table 1. Langmuir and Freundlich parameters as a function of the molar Ca^{2+} : NTMP ratio.[(a)]

Ca^{2+} : NTMP	**q_{max} ($kg\ kg^{-1}$)**	**k_L ($m^3\ kg^{-1}$)**	**R^2**	**a_F ($kg\ kg^{-1}[m^3\ kg^{-1}]^n$)**	**n (-)**	**R^2**
0 : 1	0.071	2184	0.9873	0.098	0.083	0.9803
2 : 1	0.128	3143	0.9125	0.288	0.177	0.9915
60 : 1	0.178	1596	0.9866	0.332	0.146	0.9935

(a) The parameters were found from fitting the experimental adsorption isotherms.

The study showed that adsorptive equilibrium was reached after 9 h when using the powdered adsorbent (Figure 3A, line d). The isotherms presented here were obtained from data taken after adsorption for 24 h.

3.3.3 Adsorption kinetics

Adsorption is a complicated process that involves combined film, pore, and surface diffusion apart from sorbate-sorbent and sorbate-sorbate interactions. However, it is desirable to use simplified models for mass transfer that only consides the dominating mass transport mechanisms in the adsorption process for design and process operation purposes. The two models used in this study consider the combined mass transport mechanisms of film diffusion across the hydrodynamic boundary layer of the adsorbent and intraparticle resistance in the form of either pore or surface diffusion (Figure 2).

Both models are based on the Fickian laws for diffusion and are denoted as the pore diffusion model (PDM) and the surface diffusion model (SDM); see Table 2 (36, 37). The following assumptions were made:

(1) The adsorbate in the bulk is ideally mixed.
(2) The adsorbent particles are spherical with the same radius R.
(3) The rate of adsorption is much faster than the rate of diffusion, so there is an instantaneous equilibrium according to the (Freundlich) isotherm between the fluid-phase concentration and the adsorbed-phase concentration at each position inside the pores.
(4) The film mass transfer coefficient is independent of the bulk liquid concentrations in the batch adsorber.
(5) The effective diffusivity is independent of the concentration in the pores.

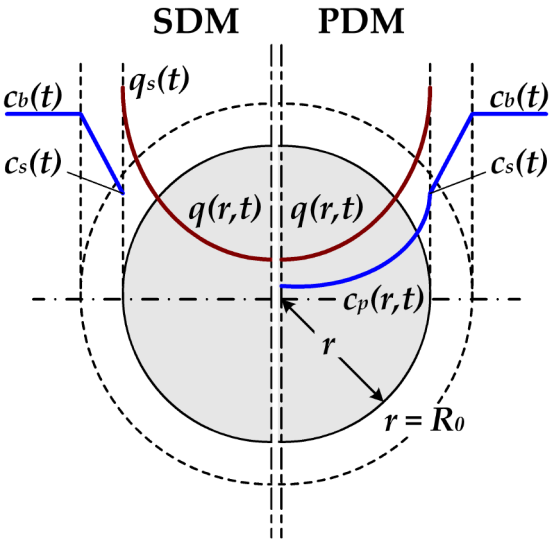

Figure 2. Concentration profiles in a spherical adsorbent particle as described by the PDM and the SDM.

Table 2. Model equations describing the adsorption kinetics

	Pore Diffusion Model	**Surface Diffusion Model**
Particle mass balance	$\frac{\partial c_p(r,t)}{\partial t} + \rho_p \frac{1-\varepsilon_p}{\varepsilon_p} \frac{\partial q(r,t)}{\partial t} = D_p \frac{1}{r^2} \frac{\partial}{\partial r}\left(r^2 \frac{\partial c_p(r,t)}{\partial r} \right)$	$\frac{\partial q(r,t)}{\partial t} = D_s \frac{1}{r^2} \frac{\partial}{\partial r}\left(r^2 \frac{\partial q(r,t)}{\partial r} \right)$
Boundary conditions	$\left.\frac{\partial q(r,t)}{\partial r}\right\|_{r=0} = \left.\frac{\partial c_p(r,t)}{\partial r}\right\|_{r=0} = 0$	$\left.\frac{\partial q(r,t)}{\partial r}\right\|_{r=0} = 0$
	$\varepsilon_p D_p \left.\frac{\partial c_p(r,t)}{\partial r}\right\|_{r=R} = k_f \left(c_b(t) - c_p(R,t) \right)$	$\rho_p D_s \left.\frac{\partial q(r,t)}{\partial r}\right\|_{r=R} = k_f \left(c_b(t) - c_s(R,t) \right)$
Initial conditions	$c_b(0) = c_0,\ q(r,0) = c_p(r,0) = 0$	$c_b(0) = c_0,\ q(r,0) = 0$
Equilibrium	$q(r,0) = f\left(c_p(r,t) \right)$	$q(R,0) = f\left(c_s(t) \right)$
Average amount adsorbed	$\bar{q} + \frac{\varepsilon_p}{\rho_p} \bar{c_p} = \frac{3}{R^3} \int_0^R \left(q(r,t) + \frac{\varepsilon_p}{\rho_p} c_p(r,t) \right) r^2 dr$	$\bar{q}(t) = \frac{3}{R^3} \int_0^R q(r,t) r^2 dr$
Mass balance batch adsorber	$V\left(c_0 - c_b(t) \right) = w \left(\bar{q} + \frac{\varepsilon_p}{\rho_p} \bar{c_p} \right)$	$V\left(c_0 - c_b(t) \right) = w \bar{q}(t)$

The amounts of adsorbed NTMP on GFH as a function of time are plotted in Figure 3 C, D in terms of the initial concentration, c_0 (×10^{-3} kg m^{-3}), and adsorbent mass, w (×10^{-3} kg).

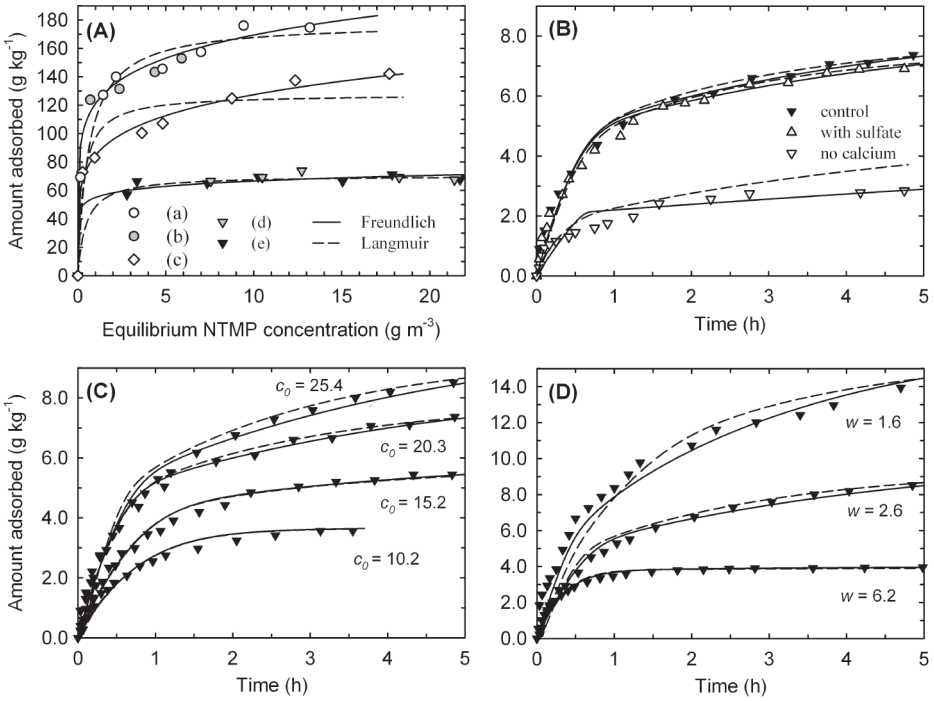

Figure 3. **(A)** Equilibrium adsorption isotherms for the adsorption of NTMP on GFH described by means of the Freundlich and Langmuir isotherm models: (a) control, Ca^{2+} : NTMP = 60 : 1; (b) control + sulfate; (c) Ca^{2+} : NTMP = 2 : 1; (d) Ca^{2+} : NTMP = 0 : 1, 24 h results; (e) Ca^{2+} : NTMP = 0 : 1, 9 h results. **(B)** Effect of sulfate and calcium ions on the adsorbed amount profile of NTMP on GFH (c_0 = 20.3 × 10^{-3} kg m^{-3}); **(C)** Comparison of the experimental and theoretical adsorbed amount profiles of NTMP on GFH (adsorbent mass = 2.6 × 10^{-3} kg) as a function of the initial NTMP concentration, c_0 ($kg\ m^{-3}$); **(D)** Comparison of the experimental and theoretical adsorbed amount profiles of NTMP on GFH (c_0 = 25.4 × 10^{-3} kg m^{-3}) as a function of the adsorbent mass, w (×10^{-3} kg). The solid and dashed lines in panels B-D represent the numerical solutions of the SDM and PDM models, respectively.

Both the pore and surface diffusion models with the effective diffusivity and external film mass transfer coefficient as model parameters gave fairly good agreement with the experimental data (Table 3).

Table 3. Results of PDM and SDM modeling for NTMP adsorption on GFH.

Solution	w $\times 10^{-3}$ (kg)	c_0 $\times 10^{-3}$ $(kg\ m^{-3})$	D_p $\times 10^{-10}$ $(m^2\ s^{-1})$	k_f $\times 10^{-5}$ $(m\ s^{-1})$	RE[(b)] (%)	D_s $\times 10^{-15}$ $(m^2\ s^{-1})$	k_f $\times 10^{-5}$ $(m\ s^{-1})$	RE (%)
SC[(a)]	1.55	25.4	7.1 ± 2.4	3.3 ± 0.9	8.5	20.0 ± 1.8	3.6 ± 0.4	4.6
	2.61	25.4	2.3 ± 0.6	3.3 ± 0.0	4.6	6.2 ± 0.4	2.5 ± 0.1	2.5
	2.50	20.3	2.4 ± 0.5	3.3 ± 0.5	4.7	4.8 ± 0.6	3.0 ± 0.3	4.2
	2.55	15.2	2.2 ± 0.5	2.9 ± 0.1	4.0	2.6 ± 0.5	2.6 ± 0.1	4.0
	2.61	10.2	<1.3 ± 2.6	3.3 ± 0.1	3.9	<1.3 ± 1.6	2.8 ± 0.1	4.2
	6.30	25.4	<1.2 ± 2.5	3.3 ± 0.4	3.0	<1.2 ± 1.1	2.7 ± 0.1	4.6
SC no Ca^{2+}[(c)]	2.61	20.3	0.3 ± 0.2	1.4 ± 0.5	3.2	2.1 ± 0.6	1.3 ± 0.2	4.1
SC with SO_4^{2-}	2.61	20.3	2.6 ± 0.6	3.3 ± 0.5	6.1	4.4 ± 0.6	3.0 ± 0.2	4.4

(a) SC = synthetic concentrate; (b) RE = relative error between experimental data and model prediction; (c) Langmuir model used.

The estimated values for the external film mass transfer coefficients, k_f, are approximately constant and correspond reasonably well with the values that can be estimated from the initial slope of the concentration decay profiles when intraparticle diffusional resistance is negligible ($k_f = [2.9 \pm 0.5] \times 10^{-5}$ m s^{-1}) (38). The estimated values for the surface diffusivity, D_s, increase with increasing surface coverage (i.e., high initial NTMP concentrations and/or low adsorbent mass). On the other hand, the pore diffusivity, D_p, seems to be relatively constant with initial NTMP concentration at constant adsorbent mass, which justifies model assumption 5. The parameter sensitivity analysis revealed that the diffusivities in both models could be less accurately estimated than the external film mass transfer coefficients. Thus, the predictions of both models are more sensitive to changes in k_f than in D_s or D_p. The calculated standard deviations for the parameters in the SDM model seem to be relatively lower compared to those calculated for the PDM model, indicating that the SDM model parameters are better identifiable.

In liquid-phase adsorption, the pore diffusivity equals the molecular diffusivity modified by the physical properties of the adsorbent, including adsorbent porosity, pore tortuosity, and pore constrictivity (i.e., reflecting the ratio of the adsorbate size to the average pore size). Therefore, as one may expect, the effective pore diffusivities should be at least 1 order of magnitude lower than the molecular diffusivity, which is on the order of 10^{-9} m^2 s^{-1} (38). The values for the pore diffusivities obtained here are 1 order of magnitude lower, which indicates that the pore diffusion model can describe the adsorption process quite well. In other words, no unrealistically high values of D_p are needed to fit the model with the experimental data. Although it is likely that other mechanisms, in particular surface diffusion, contribute to the intraparticle diffusion process as well, these results suggest that pore diffusion plays a significant role, especially when the high porosity and the presence of mesopores in GFH are taken into account.

According to the ratio of the external mass transfer resistance over the internal mass transfer resistance, which is reflected by the Biot number, intraparticle diffusion is the controlling mass transfer mechanism in all

experiments.

The response surface plots in Figure 4 show the correlation between the external film mass transfer coefficient and effective diffusivity, revealing the true minimum values of the error between the experimental data and the model prediction.

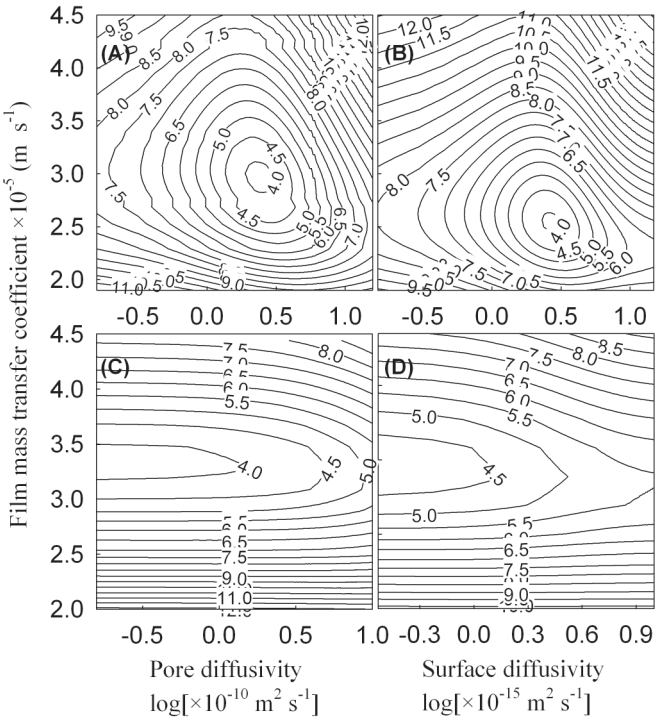

Figure 4. Response surface plots of the PDM and SDM simulations for two experiments with an initial NTMP concentration of (A, B) 15.2 × 10^{-3} kg m^{-3} and (C, D) 10.2 × 10^{-3} kg m^{-3}. The plots show that the effective diffusivities become unidentifiable when the average surface loading of the adsorbent becomes very low. The numbers in the plots represent the relative error (%) between the experimental data and the model prediction.

The figures show that the estimation of the pore and surface diffusivities are becoming more difficult at low surface loadings. The estimated effective diffusivities and external film mass transfer coefficients can be used for the

design and process operation of packed bed adsorption columns.

3.3.4 The effect of calcium

Nowack and Stone (40, 41) studied the equilibrium adsorption of several phosphonates onto the iron oxy-hydroxide goethite (α-FeOOH) at pH 7.2 and found that excess calcium concentrations can increase the maximum surface coverage of phosphonates substantially. A similar effect of calcium is known for the adsorption of phosphate (42).

Phosphonates and phosphate may be coadsorbed with Ca^{2+} ions on iron oxy-hydroxides in a ternary manner, enhancing their adsorption. This phenomenon may be beneficial to the adsorption of phosphonates from membrane concentrates on GFH, because excess amounts of calcium are commonly observed in membrane concentrates.

To validate whether calcium also plays an influential role in the adsorption of phosphonate onto akaganéite, equilibrium and kinetic adsorption experiments were conducted with GFH both in the absence and in the presence of calcium. The experiments show that calcium has a remarkable influence on the adsorption of NTMP onto GFH. In the absence of calcium, much lower amounts of NTMP are adsorbed. A Ca^{2+} : NTMP ratio of 2 : 1 is already sufficient to double the adsorption capacity. The fact that both $CaCO_3$ and Ca^{2+}-NTMP precipitates do not exceed their solubility limit at these conditions demonstrates that the phenomenon responsible for the enhanced NTMP adsorption is not due to the formation of these precipitates. In the presence of calcium the shape of the isotherm transforms from a Langmuir to a Freundlich type. This may indicate that, in the presence of calcium, adsorption of NTMP is not restricted to the monolayer coverage at high equilibrium concentrations. In addition, both the effective diffusivity and external film mass transfer coefficient are lower in the absence of calcium. This shows that calcium not only increases the surface coverage of phosphonates but also increases the rate of adsorption substantially. Therefore, calcium plays an important and advantageous role in the adsorption of phosphonate onto GFH from RO concentrates.

3.3.5 Competitive adsorption of sulfate

Besides calcium and (bi)carbonate, sulfate is one of the major anions commonly present in membrane concentrates. Sulfate might compete with phosphonates for adsorption sites, thereby reducing the adsorption capacity for phosphonate.

To explore this possibility, an excess amount of sulfate was added to the concentrate solution (i.e., 4 mM). From Figure 3A, it is apparent that the equilibrium adsorption of NTMP on GFH has not been affected by the presence of sulfate. Also, the adsorption kinetics was not affected by sulfate, because experimental data collected in the presence and absence of sulfate are nearly indistinguishable (Figure 3B). In fact, quantification of the sulfate content with ion chromatography showed that no adsorption of sulfate occurred. These results clearly indicate that NTMP has a higher affinity for adsorption on GFH than sulfate and, therefore, is a stronger competitor. This is in agreement with previous results reported for the adsorption of phosphate onto GFH (43-45). These studies showed that GFH exhibits a high selectivity for phosphate ions despite the presence of large amounts of major cations and anions. In general, it has been observed that the pH dependence of sulfate adsorption on iron oxy-hydroxides is much larger that that of phosphate adsorption and that sulfate adsorption above the point of zero charge (PZC) of the iron oxy-hydroxide is negligible (45-47). In this study, the high bicarbonate content of the concentrates dictates the pH toward 7.85, which is above the reported value of the PZC of GFH (i.e., 7.5) (48). Therefore, no adsorption of sulfate was observed, and as a result, the adsorption of NTMP was not affected. In conclusion, sulfate affects neither the equilibrium nor the kinetics of adsorption of NTMP on GFH in membrane concentrates at pH 7.85 ± 0.02.

3.3.6 Adsorbent reusability

An important aspect in the selection of a suitable adsorbent is its reusability. If GFH can successfully be regenerated, not only is it possible to reuse it, but it also provides a way to recover NTMP from the RO concentrate. The performance of GFH in an adsorption/desorption cycle as a function of

adsorbent mass is shown in Figure 5. By transferring the saturated GFH particles into a 0.1 M NaOH solution after the first adsorption step, desorption of NTMP occurs. It is noticeable, however, that even at pH 13 a significant amount of NTMP remains adsorbed, indicating that the binding of NTMP is facilitated by strong chemical bonds. This is supported by earlier observations that the adsorption of phosphate and phosphonates onto iron oxy-hydroxides is nearly independent of the ionic strength, which points toward a so-called inner-sphere complex (41, 49, 50).

Following the desorption step in NaOH, the particles were washed with 1 dm^3 of deionized water twice for 4h. Apparently, this washing with deionized water removed the remainder of adsorbed NTMP from the GFH particles because the second adsorption step shows a repetition of the dynamical shape of the first adsorption step and a similar adsorption capacity was reached. Therefore, it can be concluded that GFH is reusable.

If the adsorption of phosphonate onto GFH is thought of as a mononuclear complexation reaction, as proposed by Nowack and Stone (41) for phosphonate adsorption onto goethite, it is easily understood why NTMP desorbs at high pH. At high pH, a shift in the adsorption equilibrium occurs so that less NTMP is bound to the surface hydroxyl groups. In addition, the surface of the GFH is negatively charged at high pH, because the surface acid/base reaction is shifted more towards negatively charged species, which hinders the adsorption of the highly negative NTMP anion (protonation constant for $H_1NTMP^{5-} + H^+ = 7.25$ (51)). Consequently, desorption of NTMP occurs at pH 13. Dissolution of GFH might be another mechanism that contributes to the observed desorption of NTMP, because the solubility of iron oxy-hydroxides increases above pH 9 (52).

Chitrakar et al. (44) used synthetic akaganéite for phosphate adsorption from seawater and also regenerated with a 0.1 M NaOH solution. They reported almost no loss in capacity for up to 12 adsorption/desorption cycles. Although these observations indicate that GFH is relatively robust, prolonged contact with water reduces the chloride content of akaganéite and thereby increases the chance of collapse of the structure.

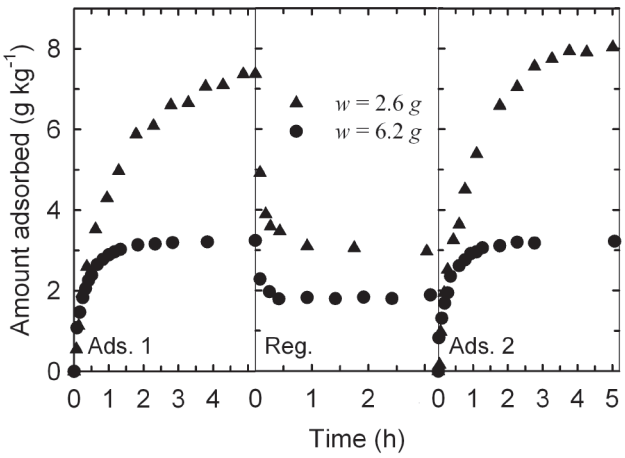

Figure 5. Reusability of different loads of GFH after treatment with a 0.1 M NaOH solution and deionized water. The initial NTMP concentration in the adsorption steps was 20.3×10^{-3} kg m^{-3}.

This may lead to, depending on temperature, the transformation to the more crystalline phase goethite or hematite, which will mitigate the adsorption capacity. Especially during regeneration, the stabilizing chloride ions can be exchanged by hydroxide ions. Therefore, the possibility of structure collapse and dissolution of GFH during regeneration should be taken into account in future research.

Nevertheless, it can be concluded that GFH is reusable after regeneration with sodium hydroxide solution, which indicates that NTMP can potentially be recovered from the RO concentrate.

3.4 Acknowledgements

This work was performed in the TTIW-cooperation framework of Wetsus, Centre of Excellence for Sustainable Water Technology (www.wetsus.nl). Wetsus is funded by the Dutch Ministry of Economic Affairs, the European Union Regional Development Fund, the Province of Fryslân, the City of Leeuwarden, and the EZ/Kompas program of "Samenwerkingsverband Noord-Nederland". We thank the participants of the research theme

"Concentrates" for the discussions and their financial support. We especially thank Christine Wegmann and Maarten Biesheuvel for their useful suggestions and Jan Tuinstra for constructing the reactor baffles. We gratefully acknowledge GEH Wasserchemie for providing us with a free sample of GFH.

3.5 Nomenclature

a_F	constant in the Freundlich isotherm	kg kg^{-1}(m^3 kg^{-1})^n
c_0	initial liquid-phase concentration	kg m^{-3}
c_b	liquid-phase concentration at any time t	kg m^{-3}
c_p	concentration of adsorbate in the pores at any time t	kg m^{-3}
$\overline{c_p}$	average of c_p over time and particle volume	kg m^{-3}
c_s	adsorbate concentration at $r = R$	kg m^{-3}
D_p	effective pore diffusivity	m^2 s^{-1}
D_s	effective surface diffusivity	m^2 s^{-1}
k_L	constant in the Langmuir isotherm	m^3 kg^{-1}
k_f	external film mass transfer coefficient	m s^{-1}
n	exponent in the Freundlich isotherm	-
q	amount adsorbed on the surface	kg kg^{-1}
q_{eq}	amount adsorbed on the surface at equilibrium	kg kg^{-1}
q_{max}	maximum possible amount adsorbed on the surface	kg kg^{-1}
q_0	value of q corresponding to c_0	kg kg^{-1}
$\overline{q}$	average of q over time and particle volume	kg kg^{-1}
r	radial coordinate of the particle	m
R	(average) particle radius	m
t	time	s
V	volume of sorbate solution	m^3
w	mass of adsorbent	kg
ε_p	particle porosity	-
ρ_p	particle density	kg m^{-3}

3.6 Literature cited

(1) Knepper, T. P. Synthetic chelating agents and compounds exhibiting complexing properties in the aquatic environment. *TrAC, Trends Anal. Chem.* **2003**, *22*, 708-724.

(2) Nowack, B. Environmental chemistry of phosphonates. *Water Res.* **2003**, *37*, 2533-2546.

(3) Reddy, M. M. N., G. H. Calcite crystal growth inhibition by phosphonates. *Desalination* **1973**, *12*, 61-73.

(4) Zieba, A.; Sethuraman, G.; Perez, F.; Nancollas, G. H.; Cameron, D. Influence of Organic Phosphonates on Hydroxyapatite Crystal Growth Kinetics. *Langmuir* **1996**, *12*, 2853-2858.

(5) Tang, Y. M.; Yang, W. Z.; Yin, X. S.; Liu, Y.; Yin, P. W.; Wang, J. T. Investigation of $CaCO_3$ scale inhibition by PAA, ATMP and PAPEMP. *Desalination* **2008**, *228*, 55-60.

(6) Butt, F. H. R., F.; Baduruthamal, U. Evaluation of SHMP and advanced scale inhibitors for control of $CaSO_4$, $SrSO_4$, and $CaCO_3$ scales in RO desalination. *Desalination* **1997**, *109*, 323-332.

(7) Hasson, D.; Drak, A.; Semiat, R. Inception of $CaSO_4$ scaling on RO membranes at various water recovery levels. *Desalination* **2001**, *139*, 73-81.

(8) Essam E.A, G. Enhancing RO system performance utilizing antiscalants. *Desalination* **2003**, *153*, 149-153.

(9) Tzotzi, C. P., T.; Yiantsios, S. G.; Karabelas, A. J.; Andritsos, N. A study of $CaCO_3$ scale formation and inhibition in RO and NF membrane processes. *J. Membr. Sci.* **2007**, *296*, 171–184.

(10) Greenlee, L. F.; Lawler, D. F.; Freeman, B. D.; Marrot, B.; Moulin, P. Reverse osmosis desalination: water sources, technology, and today's challenges. *Water Res.* **2009**, *43*, 2317-2348.

(11) Antony, A.; Low, J. H.; Gray, S.; Childress, A. E.; Le-Clech, P.; Leslie, G. Scale formation and control in high pressure membrane water treatment systems: a review. *J. Membr. Sci.* **2011**, *383*, 1-16.

(12) Squire, D. Reverse osmosis concentrate disposal in the UK. *Desalination* **2000**, *132*, 47-54.

(13) Nederlof, M. M.; Hoogendoorn, J. H. Desalination of brackish groundwater: the concentrate dilemma. *Desalination* **2005**, *182*, 441-447.

(14) Nederlof, M. M.; van Paassen, J. A. M.; Jong, R. Nanofiltration concentrate disposal: experiences in The Netherlands. *Desalination* **2005**, *178*, 303-312.

(15) Khan, S. J.; Murchland, D.; Rhodes, M.; Waite, T. D. Management of concentrated

waste streams from high-pressure membrane water treatment systems. *Crit. Rev. Environ. Sci. Technol.* **2009**, *39*, 367-415.

(16) Tularam, G. A.; Ilahee, M. Environmental concerns of desalinating seawater using reverse osmosis. *J. Environ. Monit.* **2007**, *9*, 805-813.

(17) Lattemann, S.; Höpner, T. Environmental impact and impact assessment of seawater desalination. *Desalination* **2008**, *220*, 1-15.

(18) Hoepner, T.; Lattemann, S. Chemical impacts from seawater desalination plants a case study of the northern Red Sea. *Desalination* **2003**, *152*, 133-140.

(19) Correll, D. L. The role of phosphorus in the eutrophication of receiving waters: a review. *J. Environ. Qual.* **1998**, *27*, 261-266.

(20) Gabelich, C. J., Williams, M. D., Rahardianto, A., Franklin, J. C., Cohen, Y. High-recovery reverse osmosis desalination using intermediate chemical demineralization. *J. Membr. Sci.* **2007**, *301*, 131–141.

(21) Rahardianto, A.; McCool, B. C.; Cohen, Y. Accelerated desupersaturation of reverse osmosis concentrate by chemically-enhanced seeded precipitation. *Desalination* **2010**, *264*, 256-267.

(22) Greenlee, L. F.; Testa, F.; Lawler, D. F.; Freeman, B. D.; Moulin, P. Effect of antiscalants on precipitation of an RO concentrate: metals precipitated and particle characteristics for several water compositions. *Water Res.* **2010**, *44*, 2672-2684.

(23) Greenlee, L. F.; Testa, F.; Lawler, D. F.; Freeman, B. D.; Moulin, P. Effect of antiscalant degradation on salt precipitation and solid/liquid separation of RO concentrate. *J. Membr. Sci.* **2011**, *366*, 48-61.

(24) Sillanpää, M. E. T.; Agustiono Kurniawan, T.; Lo, W. H. Degradation of chelating agents in aqueous solution using advanced oxidation process (AOP). *Chemosphere* **2011**, *83*, 1443-1460.

(25) Forlani, G.; Prearo, V.; Wieczorek, D.; Kafarski, P.; Lipok, J. Phosphonate degradation by *Spirulina* strains: cyanobacterial biofilters for the removal of anticorrosive polyphosphonates from wastewater. *Enzyme Microb. Technol.* **2011**, *48*, 299-305.

(26) Yang, Q. F.; Lisitsin, D.; Liu, Y. Q.; David, H.; Semiat, R. Desupersaturation of RO concentrates by addition of coagulant and surfactant. *J. Chem. Eng. Jpn.* **2007**, *40*, 730-735.

(27) Schwertmann, U., Cornell, R. M. *Iron Oxides in the Laboratory*, Wiley-VCH Verlag GmbH: Weinheim, Germany, 2000.

(28) Driehaus, W.; Jekel, M.; Hildebrandt, U. Granular ferric hydroxide a new

adsorbent for the removal of arsenic from natural water. *J. Water Supply: Res. Technol.* **1998**, *47*, 30-35.

(29) Ibrahim, H.; Issa, Y. M.; Kamal, R. The determination of phosphonate base scale inhibitors in brines by plasma spectrometry. *Mikrochim. Acta* **1992**, *109*, 201-209.

(30) Box, G. E. P.; Wilson, K. B. On the experimental attainment of optimum conditions. *J. R. Stat. Soc. B* **1951**, *13*, 1-45.

(31) Keesman, K. J. *System Identification: An Introduction*; Springer: London, 2011.

(32) Brunauer, S.; Emmett, P. H.; Teller, E. Adsorption of Gases in Multimolecular Layers. *J. Am. Chem. Soc.* **1938**, *60*, 309.

(33) Steiner, M.; Pronk, W.; Boller, M. A. Modeling of copper sorption onto GFH and design of full-scale GFH adsorbers. *Environ. Sci. Technol.* **2006**, *40*, 1629-1635.

(34) Colomban, P.; Cherifi, S.; Despert, G. Raman identification of corrosion products on automotive galvanized steel sheets. *J. Raman Spectrosc.* **2008**, *39*, 881-886.

(35) Foo, K. Y.; Hameed, B. H. Insights into the modeling of adsorption isotherm systems. *Chem. Eng. J.* **2010**, *156*, 2-10.

(36) Webi, T. W.; Chakravort, R. K. Pore and solid diffusion models for fixed-bed adsorbers. *AIChE J.* **1974**, *20*, 228-238.

(37) Moon, H.; Kook Lee, W. Intraparticle diffusion in liquid-phase adsorption of phenols with activated carbon in finite batch adsorber. *J. Colloid Interface Sci.* **1983**, *96*, 162-171.

(38) McKay, G.; El Geundi, M.; Nassar, M. M. External mass transport processes during the adsorption of dyes onto bagasse pith. *Water Res.* **1988**, *22*, 1527-1533.

(39) Chisti, Y., *Kirk-Othmer Encyclopedia of Chemical Technology*, 5th ed.; Wiley: New York, 2005; Vol. 15, pp 1–75.

(40) Nowack, B.; Stone, A. T. The influence of metal ions on the adsorption of phosphonates onto goethite. *Environ. Sci. Technol.* **1999**, *33*, 3627-3633.

(41) Nowack, B.; Stone, A. T. Adsorption of Phosphonates onto the Goethite-Water Interface. *J. Colloid Interface Sci.* **1999**, *214*, 20-30.

(42) Rietra, R. J. J.; Hiemstra, T.; van Riemsdijk, W. H. Interaction between Calcium and Phosphate Adsorption on Goethite. *Environ. Sci. Technol.* **2001**, *35*, 3369-3374.

(43) Sperlich, A.; Warschke, D.; Wegmann, C.; Ernst, M.; Jekel, M. Treatment of membrane concentrates: phosphate removal and reduction of scaling potential. *Water Sci. Technol.* **2010**, *61*, 301-306.

(44) Chitrakar, R.; Tezuka, S.; Sonoda, A.; Sakane, K.; Ooi, K.; Hirotsu, T. Phosphate adsorption on synthetic goethite and akaganeite. *J. Colloid Interface Sci.* **2006**, *298*, 602-608.

(45) Genz, A.; Kornmüller, A.; Jekel, M. Advanced phosphorus removal from membrane filtrates by adsorption on activated aluminium oxide and granulated ferric hydroxide. *Water Res.* **2004**, *38*, 3523-3530.

(46) Geelhoed, J. S.; Hiemstra, T.; Van Riemsdijk, W. H. Phosphate and sulfate adsorption on goethite: single anion and competitive adsorption. *Geochim. Cosmochim. Acta* **1997**, *61*, 2389-2396.

(47) Ryden, J. C.; Syers, J. K.; Tillman, R. W. Inorganic anion sorption and interactions with phosphate sorption by hydrous ferric oxide gel. *J. Soil Sci.* **1987**, *38*, 211-217.

(48) Saha, B.; Bains, R.; Greenwood, F. Physicochemical characterization of granular ferric hydroxide (GFH) for arsenic(V) sorption from water. *Sep. Sci. Technol.* **2005**, *40*, 2909-2932.

(49) Deliyanni, E. A.; Peleka, E. N.; Lazaridis, N. K. Comparative study of phosphates removal from aqueous solutions by nanocrystalline akaganéite and hybrid surfactant-akaganéite. *Sep. Purif. Technol.* **2007**, *52*, 478-486.

(50) Boels, L.; Tervahauta, T.; Witkamp, G. J. Adsorptive removal of nitrilotris(methylenephosphonic acid) antiscalant from membrane concentrates by iron-coated waste filtration sand. *J. Hazard. Mater.* **2010**, *182*, 855-862.

(51) Popov, K.; Rönkömäki, H.; Lajunen, L. H. J. Critical evaluation of stability constants of phosphonic acids (IUPAC Technical Report). *Pure Appl. Chem.* **2001**, *73*, 1641-1677.

(52) Liu, X.; Millero, F. J. The solubility of iron hydroxide in sodium chloride solutions. *Geochim. Cosmochim. Acta* **1999**, *63*, 3487-3497.

ADSORPTION OF PHOSPHONATE ANTISCALANT FROM REVERSE OSMOSIS MEMBRANE CONCENTRATE ONTO IRON-COATED WASTE FILTRATION SAND

4

In analogy with Chapter 3, the adsorption and desorption of nitrilotris(methylene-phosphonic acid) (NTMP) from Reverse Osmosis (RO) membrane concentrate onto an alternative iron based adsorbent was investigated. This adsorbent, iron-coated waste filtration sand (WFS), was first presented in Chapter 2. The equilibrium adsorption of NTMP was described well with a Langmuir isotherm. The kinetics of the adsorption of NTMP onto WFS could be described well with a pore or a surface diffusion model. Also, WFS can be reused after regeneration with a sodium hydroxide solution. WFS appeared to have a lower adsorption capacity and rate compared to GFH, which was related to the presence of impurities, the presence of manganese oxides in the coating, and aging of the ferrihydrite phase.

4.1 Introduction

In the preceding chapter, it was shown that the commercially available granular ferric hydroxide (GFH) is a very effective phosphonate adsorbent. Here, the performance of the cheap alternative adsorbent presented in Chapter 2 will be investigated in more detail. Iron-coated waste filtration sand (WFS) can be considered to be low-cost because it is abundantly available as a waste by-product in the production of drinking water from groundwater (1). Aeration of groundwater in rapid sand filtration processes is often applied for the removal of dissolved iron and manganese before the groundwater undergoes further treatment (e.g., membrane filtration) (2). The presence of iron oxy-hydroxide, predominantly in the form of ferrihydrite, in the coating of WFS was shown to be the key in its applicability as an adsorbent for the phosphonate antiscalant nitrilotris(methylenephosphonic acid) (NTMP) (3).

The objective is to investigate the adsorption and desorption of NTMP from RO membrane concentrate onto WFS. Both equilibrium and kinetic studies were carried out to determine the sorption capacity and the rate of NTMP uptake for WFS. It is aimed at modeling the adsorption kinetics with different models for intra-particle diffusion. Ultimately, a comparison can be made between the performance of WFS and GFH in adsorbing NTMP.

4.2 Materials and methods

4.2.1 Adsorbent

The iron-coated waste filtration sand (WFS) used in this study was obtained from one of the largest drinking water companies in the Netherlands. WFS is a waste by-product in the production of drinking water from groundwater. Therefore, this waste material contains contaminants like natural organic matter and a fraction of phosphate. For this reason, the material was washed with 3 batches of a 0.1 M NaOH solution and subsequently washed thoroughly with distilled water. The WFS material was sieved to 2.0 - 3.0 mm. The water content was determined to be 22.5 ± 2.3 %. All results are presented

on a dry mass basis (drying at 105 °C for 24 h). The same batch of WFS was used throughout all experiments.

A detailed analysis of the coating properties of WFS with infrared spectroscopy (ATR-FTIR) (Shimadzu 4800), powder X-ray diffraction and elemental analysis were presented in Chapter 2. The coating consists mainly of the amorphous iron oxy-hydroxide ferrihydrite. The specific surface area and the pore volume of WFS were measured with nitrogen adsorption (Micromeritics Tristar 3000) on 6 replicate samples. The surface and structure of the adsorbent was further characterized by scanning electron microscopy (Jeol JSM-6480 LV) and X-ray Photoelectron Spectroscopy (PHI 5400, ESCA).

4.2.2 Methods

In Chapter 3, the experimental procedures for the equilibrium and kinetic adsorption experiments have been described in detail. The same procedures, solutions and equipment were used in this study. In short, adsorption experiments were conducted at 297.5 ± 0.5 K in synthetic concentrate solutions that were prepared by the simultaneous addition of 0.5 dm^3 of a 12 mM $CaCl_2.2H_2O$ solution and 0.5 dm^3 of a 28 mM $NaHCO_3$ solution containing NTMP. This synthetic concentrate solution had an ionic strength of 0.03 M and a pH of 7.85 ± 0.02.

In the experiments for determining the equilibrium adsorption isotherms, the sand cores were removed by grounding and sieving the wet WFS particles. Afterwards, part of the powdered coating was dried at 105 °C for 24 h before use. The other part was employed wet.

4.3 Results and discussion

4.3.1 Physical properties WFS adsorbent

The surface of WFS appears to be porous (Figure 1). According to the nitrogen adsorption measurements, the specific BET (4) surface area and the pore volume of the adsorbents' coating was 221.9 ± 21.9 $m^2\ g^{-1}$ and 0.24 ± 0.06 $cm^3\ g^{-1}$, respectively. The average particle radius, *R*, was determined to be 1.2 ×

10^{-3} m and the apparent particle density, ρ_p, was 1235 kg m^{-3}. From the values of the apparent particle density and the pore volume, the porosity, ε_p, of the adsorbent was calculated to be 0.30.

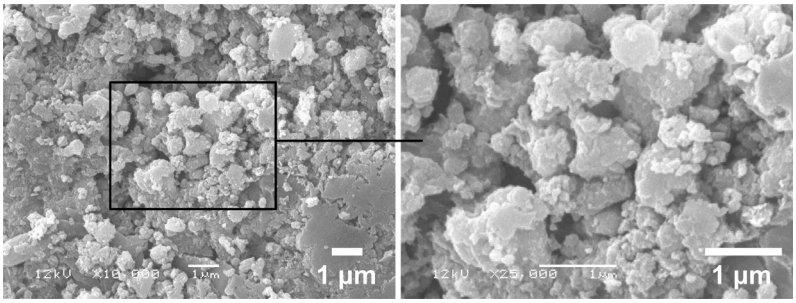

Figure 1. SEM pictures of the WFS particle surface show that the adsorbent appears to have a porous structure.

The chemical composition of the WFS coating has been presented previously, showing that approximately 10 weight % of the coating consists of manganese oxides (3). However, the X-ray diffraction and infrared spectroscopic analysis did not revealed which manganese oxide species are present. Therefore, an effort was made to analyze the ionic states of manganese and iron in the coating of WFS by using X-ray Photoelectron Spectroscopy (Figure 2 & Table 1).

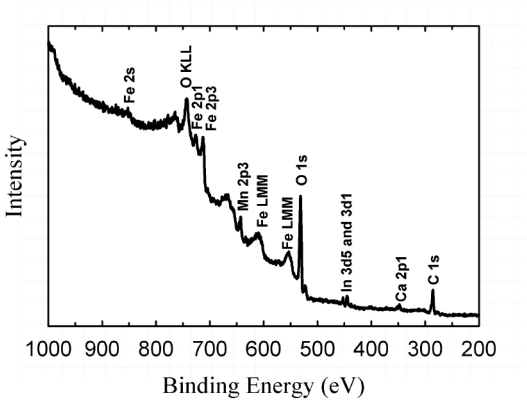

Figure 2. XPS survey of the WFS coating for the determination of the ionic state of manganese and iron.

Table 1. Identification of the recorded X-ray photoelectron lines.

Spectral line	Binding Energy (*eV*)	Occurrence (%)	Species
O $1s_{1/2}$ – 1	529.6	42	metal oxides
O $1s_{1/2}$ – 2	531.0	36	OH, ferrates, manganates
O $1s_{1/2}$ – 3	532.2	18	H_2O, CO
O $1s_{1/2}$ – 4	533.5	4	ligands
Mn $2p_{3/2}$	641.6	78	Mn_2O_3
Mn $2p_{3/2}$	643.7	22	manganates, MnO_2
Fe $2p_{3/2}$	710.6	66	Fe_2O_3, FeOOH
Fe $2p_{3/2}$	713.0	34	ferrates

According to the XPS analysis, the coating contains species of mainly Mn^{3+} and Fe^{3+}. For both of these elements, the presence of higher oxides as MnO_2, manganates, and ferrates were detected.

4.3.2 Equilibrium adsorption isotherm

The equilibrium for the adsorption of NTMP from the synthetic membrane concentrate onto iron-coated waste filtration sand is presented in Figure 3A. In contrast to the isotherms obtained for GFH, the shape of the isotherm of WFS is not of the "high-affinity" type and can be described very well with the Langmuir equation (equation 1, Chapter 3). The maximum amount that can be adsorbed on WFS is about one third that of GFH under similar conditions. Drying of the WFS coating before use mitigates the adsorption capacity substantially. For this reason, the WFS adsorbent was kept wet throughout the experiments. The Langmuir parameters k_L (222.5 m^3 kg^{-1}) and q_{max} (0.057 kg kg^{-1}) for the wet WFS coating, were found by fitting the experimental data.

Besides the lower specific surface area of WFS, a multitude of reasons can be found for the lower adsorption capacity of WFS compared to GFH. In contrast to GFH, which is pure and consist of synthesized akaganéite, WFS is produced from groundwater. Therefore, this waste material may, despite the pre-washing with NaOH, still contain contaminants that lower the available amount of sorption sites for NTMP.

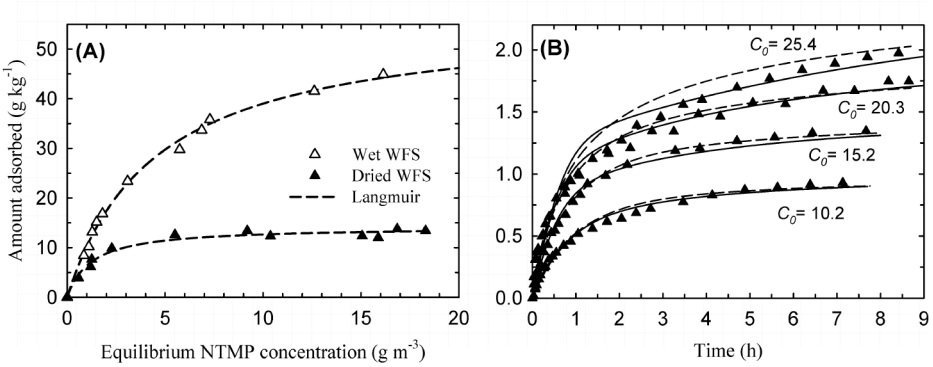

Figure 3. (A) Description of the experimental adsorption isotherms by means of the Langmuir model for the adsorption of NTMP on dried and wet WFS. (B) Comparison of the experimental and theoretical adsorbed amount profiles of NTMP on WFS (weight of coating = 10 g) as a function of the initial NTMP concentration c_0 ($g\ m^{-3}$). The dashed and solid lines represent the numerical solutions of respectively the pore and surface diffusion model.

According to the XPS analysis, the coating of WFS also contains a considerable fraction of Mn^{3+} and Mn^{4+} oxides. Most manganese oxides have a negative surface charge at near neutral pH (5). Therefore, the contribution of these manganese oxides to the adsorption of NTMP at pH 7.85 is expected to be much less compared to the ferrihydrite fraction in the coating. In addition, aging of the ferrihydrite phase in the coating is likely to decrease the reactivity towards NTMP. In general, the age of WFS may reach up to 3 years before it is taken out of the rapid sand filtration process.

4.3.3 Adsorption kinetics

The two models used in this study consider the combined mass transport mechanisms of film diffusion across the hydrodynamic boundary layer of the adsorbent and intraparticle resistance in the form of either pore or surface diffusion. Both models have been described in detail in Chapter 3.

The amount adsorbed on WFS is plotted in Figure 3B in terms of the initial NTMP concentration, c_0, at constant adsorbent weight. Both models with the effective diffusivities and external film mass transfer coefficients as model parameters gave fairly good agreement with the experimental data (Table 2).

Table 2. Results of SDM and PDM modeling for NTMP adsorption on WFS. A constant amount of WFS adsorbent was used which contained 10 g of coating.

c_0	D_s	k_f	RE[(a)]	D_p	k_f	RE
$\times 10^{-3}$	$\times 10^{-15}$	$\times 10^{-5}$		$\times 10^{-10}$	$\times 10^{-5}$	
($kg\ m^{-3}$)	($m^2\ s^{-1}$)	($m\ s^{-1}$)	(%)	($m^2\ s^{-1}$)	($m\ s^{-1}$)	(%)
10.2	22.1 ± 4.5	1.1 ± 0.1	3.4	5.1 ± 1.8	0.9 ± 0.2	3.2
15.2	18.6 ± 2.4	1.4 ± 0.1	2.4	3.9 ± 0.4	1.1 ± 0.0	1.9
20.3	16.7 ± 1.9	1.3 ± 0.1	3.6	2.0 ± 0.3	1.1 ± 0.1	3.5
25.4	10.3 ± 1.4	1.0 ± 0.1	4.4	1.2 ± 0.2	0.9 ± 0.1	4.5

(a) RE = Relative Error between experimental data and model prediction.

The estimated values for the external film mass transfer coefficients, k_f, are much lower compared to those estimated for GFH, because of the larger particle size of WFS. Both the estimated values for the surface diffusivity, D_s, and pore diffusivity, D_p, decrease with increasing surface coverage (i.e., increasing initial NTMP concentrations). It is evident form the results presented here and those presented in Chapter 3 that GFH is superior compared to WFS in terms of adsorption capacity and adsorption rate. Given the fact that WFS is a waste material and its composition depends on the raw water quality and process conditions under which it has been produced, variations in capacity from batch to batch due to material in homogeneity can be expected. On the other hand however, the low cost and on-site availability of WFS may compensate for the drawbacks of using WFS.

4.3.4 Adsorbent reusability

The performance of WFS in multiple adsorption/desorption cycles is shown in Figure 4. WFS reaches a solid (coating) phase concentration of 1.8 g kg^{-1} after 8 h in the first step. By transferring the saturated WFS particles into a 0.1 M NaOH solution, desorption of NTMP occurs. It appears that in the desorption step at pH 13 all NTMP desorbs. However, analysis of the coating composition revealed the presence of phosphate contamination (4.6 ± 0.6 g kg^{-1}) throughout the WFS particles. It is reasonable to expect that phosphate desorbs at pH 13 as well. Consequently, a higher phosphorous content was measured in the NaOH solution with ICP, a method that cannot discriminate between the

different origins of the measured phosphorus. It seems, however, that the desorption and washing steps are sufficient to remove the majority of the adsorbed NTMP, because the second and third adsorption steps show a repetition of the dynamical shape of the first adsorption step and reach almost similar solid phase concentrations. Therefore, it can be concluded that the adsorbent was successfully regenerated.

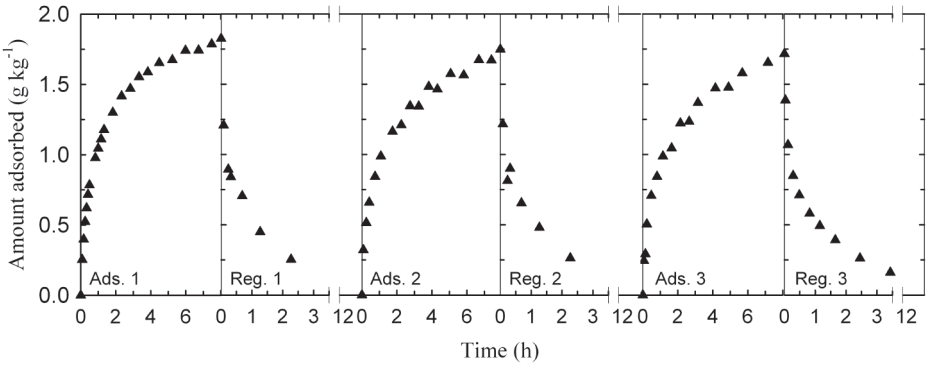

Figure 4. Reusability of WFS after treatment with 0.1 M NaOH solution and deionized water. The initial NTMP concentration in the adsorption steps was 20.3 g m^{-3}.

4.4 Conclusions

The equilibrium and kinetics of NTMP adsorption onto iron-coated waste filtration sand has been investigated. The equilibrium adsorption was described well with a Langmuir isotherm. The results showed that drying of the adsorbent mitigates the adsorption capacity substantially. The adsorption kinetics could be predicted fairly well by the pore and surface diffusion models. In comparison with GFH, WFS exhibit a lower capacity and a lower adsorption rate. Therefore, more WFS adsorbent is needed to obtain the desired degree of phosphonate removal. The lower capacity was related to the presence of impurities (e.g., phosphate) and the presence of manganese oxides. Also, the relative high age of the ferrihydrite phase in WFS may decrease its reactivity towards NTMP. However, the low cost and on-site availability may compensate for these drawbacks. WFS is reusable after regeneration with sodium hydroxide solution.

4.5 References

(1) Sharma, S. K. *Adsorptive Iron Removal from Groundwater*, Swets & Zeitlinger B.V.: Lisse, The Netherlands, 2001.

(2) Sharma, S. K.; Petrusevski, B.; Schippers, J. C. Biological iron removal from groundwater: a review. *J. Water Supply Res. Technol.* **2005**, *54*, 239-247.

(3) Boels, L.; Tervahauta, T.; Witkamp, G. J. Adsorptive removal of nitrilotris(methylenephosphonic acid) antiscalant from membrane concentrates by iron-coated waste filtration sand. *J. Hazard. Mater.* **2010**, *182*, 855-862.

(4) Brunauer, S.; Emmett, P. H.; Teller, E. Adsorption of gases in multimolecular layers. *J. Am. Chem. Soc.* **1938**, *60*, 309.

(5) Tan, W. F.; Lu, S. J.; Liu, F.; Feng, X. H.; He, J. Z.; Koopal, L. K. Determination of the point-of-zero, charge of manganese oxides with different methods including an improved salt titration method. *Soil Sci.* **2008**, *173*, 277-286.

PHOSPHONATE ANTISCALANT RECOVERY FROM MEMBRANE CONCENTRATES WITH GRANULAR FERRIC HYDROXIDE

5

The adsorption and desorption of nitrilotris(methylenephosphonic acid) (NTMP) from reverse osmosis (RO) membrane concentrates onto granular ferric hydroxide (GFH) was investigated. The effect of particle size, bed contact time and composition of the concentrate solution on the column adsorption dynamics is presented. The adsorption dynamics could be predicted reasonably well with a surface diffusion model. Also, the regeneration of the saturated column with sodium hydroxide solution was demonstrated. The desorbed NTMP can be recovered from this regeneration solution either by precipitation with calcium or by filtration over a nano-filtration membrane. Nano-filtration seemed to be technical more feasible. This work shows that GFH can be successfully employed to remove and recover phosphonate antiscalant from RO membrane concentrates

Prepared for publication in *Water Science & Technology* as:

Boels, L.; Fabregat, M. V.; Keesman, K. J.; Witkamp, G. J. Phosphonate antiscalant recovery from membrane concentrates with granular ferric hydroxide.

5.1 Introduction

The concentrate streams of reverse osmosis (RO) desalination processes contain chemical additives which are necessarily used for pre-treatment and cleaning. These additives are typically discharged into surface waters along with the concentrate, which impairs the marine environment (1-5). An important group of additives are phosphonates, which are used for scale control (i.e., antiscalants). Although the direct toxicity to aquatic life of phosphonates is low, they can have a negative affect on the environment. Phosphonates contribute to the total phosphate content, and are considered to be compounds that promote eutrophication of the receiving surface water. Also, the excellent chelating properties of phosphonates may influence the transport of heavy metals in the marine environment. In addition, the reserves of the phosphate rock used to make phosphonates are finite, and concerns have been raised that these reserves are in danger of exhaustion (6). Therefore, a concentrate treatment process has been proposed in which the phosphonate antiscalant is removed via adsorption onto granular ferric hydroxide (GFH) (7). The iron oxy-hydroxide surface of GFH was shown to have a strong affinity with phosphonate anions, which leads to favorable adsorption characteristics and high adsorption capacities.

The next step in the development of a phosphonate recovery process involves the continuous adsorption and desorption of phosphonate in a packed bed adsorption column, which is the subject of the present work. It is aimed at modeling the effluent concentration profiles, i.e., the breakthrough curves, of the packed-bed adsorption column at various operating conditions. This analysis can be used to evaluate the column design parameters and optimize its operation. Finally, the recovery of the NTMP by treating the regeneration solution with a nano-filtration or a calcium-phosphonate precipitation step will be investigated.

5.1.1 Packed-bed column modeling

In previous work it was shown that the diffusion of NTMP into the GFH particles can be described fairly well with a model that only considers surface

diffusion (7). In this surface diffusion model (SDM), the particle is assumed to be homogeneous. However, this does not preclude the use of this model for porous GFH particles where the amount of adsorbate in the pore liquid is being neglected. The mass balance inside a spherical particle can be written in dimensionless form by summarizing the essential state variables in dimensionless groups as

$$\frac{\partial Q(R,\tau)}{\partial \tau} = \frac{St}{Bi}\frac{1}{R^2}\frac{\partial}{\partial R}\left(R^2\frac{\partial Q(R,\tau)}{\partial R}\right) \tag{1}$$

with initial condition

$$Q(R,0) = 0 \tag{2}$$

and boundary condition

$$\left.\frac{\partial Q(R,\tau)}{\partial R}\right|_{R=0} = 0 \tag{3}$$

At the particle surface, the mass that diffuses into the particle equals the mass transported across the hydrodynamic boundary layer. Therefore, the second boundary condition at the particle surface is given by

$$\left.\frac{\partial Q(R,\tau)}{\partial R}\right|_{R=1} = Bi\left(C_b(\tau) - C_s(1,\tau)\right) \tag{4}$$

where the fluid phase concentration of adsorbate at the outer surface of the particle, C_s, can be related to the amount adsorbed, Q, by the Freundlich equation

$$C_s(1,\tau) = \frac{1}{c_0}\left(\frac{Q(1,\tau)q_0}{a_F}\right)^{\frac{1}{n}} \tag{5}$$

With the dimensionless variables defined as

$$Q = \frac{q}{q_0};\ \tau = \frac{t\rho_b\varphi_v}{w\varepsilon_b D_g};\ C_b = \frac{c_b}{c_0};\ C_s = \frac{c_s}{c_0};\ R = \frac{r}{R_0}$$

And the dimensionless groups defined as

$$Bi = \frac{k_f R_0 c_0}{\rho_p D_s q_0}\ \text{(Biot)};\ St = \frac{k_f w}{\rho_p R_0 \varphi_v}\ \text{(Stanton)};\ D_g = \frac{\rho_b q_0}{\varepsilon_b c_0}$$

The concentration of adsorbate in the (bulk) liquid phase, C_b, in eq 4, can be described by a differential mass balance of the isothermal packed-bed column.

$$\varepsilon_b \frac{\partial c_b(z,t)}{\partial t} = -v_f \frac{\partial c_b(z,t)}{\partial z} - 3(1-\varepsilon_b)\frac{k_f}{R}\left(c_b(z,t) - c_s(t)\right) \tag{6}$$

with the initial condition

$$c_b(z,0) = c_0 \tag{7}$$

By using the dimensionless numbers and groups defined previously, and introducing the dimensionless axial coordinate $Z = z/L$, this balance can be made dimensionless as well.

$$\frac{1}{D_g}\frac{\partial C_b(Z,\tau)}{\partial \tau} = -\frac{\partial C_b(Z,\tau)}{\partial Z} - 3St\left(C_b(Z,\tau) - C_s(\tau)\right) \tag{8}$$

with initial condition

$$C_b(Z,0) = 1 \tag{9}$$

The surface diffusion model has been successfully employed to describe the adsorption of phosphate, salicylic acid and arsenate onto GFH (8, 9).

5.1.2 *Parameter estimation*

For the surface diffusion model, the model parameters have to be known in order to predict the effluent concentration profiles of the column. The model parameters that are easily accessible represent the operation conditions and adsorber geometry, including the volumetric flow rate, ϕ_v, influent concentration, c_0, amount of adsorbent, w, density of the bed, ρ_b, grain size, R_0, and grain density, ρ_p.

The model parameters that are more difficult to obtain are the adsorption equilibrium parameters, the effective surface diffusivity and the external film mass transfer coefficient, because they have to be determined in specially designed experiments. The Freundlich equilibrium parameters, a_F and n, were determined from equilibrium adsorption isotherms obtained from batch adsorption experiments at constant temperature. The effective surface diffusivity, D_s, and the external film mass transfer coefficient, k_f, which are part of the dimensionless Biot (*Bi*) and Stanton (*St*) numbers, were estimated previously in batch kinetic experiments performed in a well-mixed basket reactor (7) (see Chapter 3, Table 3).

The external film mass transfer coefficient may also be estimated by one of the many proposed dimensionless correlations that relate the dimensionless Sherwood (*Sh*) number containing k_f, with the Reynolds (*Re*) and Schmidt (*Sc*) numbers. A widely used example is the Wakao and Funazkri correlation (10)

$$Sh = \frac{k_f 2R_0}{D_m} = 2.0 + 1.1 Re^{0.6} Sc^{\frac{1}{3}} \tag{10}$$

where D_m ($m^2\ s^{-1}$) is the molecular diffusivity. Measured molecular diffusivities have not been tabulated for NTMP or any other phosphonates, but may be calculated by using the Stokes-Einstein equation or, better, the semi-empirical modification of this equation, the Wilke-Chang equation (11)

$$D_m = 1.173 \times 10^{-16} \frac{(\xi M_b)^{0.5} T}{\eta_b V_m^{0.6}} \qquad (11)$$

where M_b (18.0×10^{-3} kg mol^{-1}) and η_b (1.015×10^{-3} Pa s) are the molecular weight and the dynamic viscosity of the solvent, respectively, T (K) is the temperature and ξ (-) is the association parameter, which is 2.26 for water. The molar volume, V_m ($m^3\ mol^{-1}$), of NTMP can be calculated using a method based on Traube's additivity principle (12), which gives for NTMP a molar volume of 1.98×10^{-4} m^3 mol^{-1}. From eq 11 the molecular diffusivity of NTMP was calculated to be 1.16×10^{-9} m^2 s^{-1}. Depending on the flow rate, k_f was calculated from eq 10 to be in the range of 2.5×10^{-5} - 3.4×10^{-5} m s^{-1} for the largest grain size (Appendix C, Table C3), which corresponds quite well with the previously measured values of 2.6×10^{-5} - 3.0×10^{-5} m s^{-1}. All input parameters used for modeling the column adsorption experiments are tabulated in Appendix C.

5.2 Materials and methods

5.2.1 Adsorbent

Commercially available granular ferric hydroxide (GFH) was obtained from GEH Wasserchemie (Osnabrück). GFH consists predominantly of the chloride-bearing iron oxy-hydroxide β-FeOOH, or akaganéite (13). The GFH material was sieved wet to 0.5 - 2.0 mm, 0.5 - 1.0 mm, and 0.2 - 0.5 mm to give three different batches of GFH with a more uniform grain size. The water content, particle density, average particle radius, the average bed densities and the bed porosities for the three batches are listed in Table C2 of Appendix C.

5.2.2 *Synthetic membrane concentrates*

The composition of the water used for the adsorption experiments was based on that of concentrates produced by brackish water nano-filtration installations. Different synthetic membrane concentrates (SC) were made in the laboratory, in which the major ions commonly observed in these brackish water concentrates were added (Table 1). The synthetic concentrate solutions were prepared by the simultaneous addition of a 12 mM $CaCl_2.2H_2O$ solution and a 28 mM $NaHCO_3$ solution containing the phosphonate antiscalant NTMP (solution denoted with SC 1). In another set of experiments, KNO_3, Na_2SO_4 and $MgCl_2.6H_2O$ were added as well (solution SC 2).

Table 1. Composition of the used synthetic concentrate solutions compared to that of real membrane concentrates produced by two large-scale brackish water nano-filtration installations located in the Netherlands.

Component	Units	Synthetic concentrates		Real concentrates	
		SC 1	SC 2	A	B
Na^+	g m^{-3}	322	465	110	203
K^+	g m^{-3}	-	12.6	16.3	23
Ca^{2+}	g m^{-3}	240	240	535	322
Mg^{2+}	g m^{-3}	0	40	42.7	43.9
Ba^{2+}	g m^{-3}	-	-	0.45	n.a.
HCO_3^-	kg m^{-3}	0.854	0.854	1.21	0.875
SO_4^{2-}	g m^{-3}	0	300	494	260
NO_3^-	g m^{-3}	-	20	20.5	6.8
Cl^-	g m^{-3}	425	541	176	330
PO_4^{3-}	g m^{-3}	-	-	<0.05	n.a.
NTMP	g m^{-3}	10-15	10-15	10-20	10-20
IS[(a)]	M	0.03	0.04	0.05	0.04
pH	-	7.9	7.9	7.9	7.7

(a) IS = Ionic strength

All solutions were prepared using deionized water. The employed salts were of analytical grade and were obtained from VWR. NTMP was obtained from Sigma Aldrich in its acid form with a purity of > 97 %.

5.2.3 *Packed bed adsorption experiments*

Cyclic adsorption experiments were carried out at 294 ± 1 K in a packed bed column, which involved three steps: adsorption, regeneration and washing. The column with an inner diameter of 8 mm was packed with 2.5 or 4.2 g (dry mass basis) of GFH between two supporting layers of glass beads (diameter 1.1 mm). Before operation, the bed was rinsed with deionized water to ensure that the bed was well packed and free of air bubbles. Fresh concentrate solution was fed to the column continuously in an up-flow mode with a flow of 1.1×10^{-3} or 1.7×10^{-7} m^3 s^{-1}. Samples of the effluent were collected at specified times intervals, diluted with a 1 % HNO_3 solution and analyzed for the phosphorous content with inductively-coupled plasma spectrometry (ICP, Optima 3000XL, Perkin-Elmer). The pH of the effluent was monitored over time. Besides varying the flow rate and the weight of the bed, the NTMP concentration in the feed solution was varied between 10 and 15 g m^{-3}. Virgin GFH material was used in each experiment when an operating parameter was changed. In some cases, after a breakthrough, the saturated particles in the bed were regenerated by recirculating a 0.1 M or a 0.5 M NaOH solution over the bed for 2.5 h. Aliquots of the regeneration solution were removed periodically with a syringe, filtered, diluted with the 1 % HNO_3 solution and analyzed for the phosphorous content with ICP. Following the regeneration step, the particles were washed by pumping 2 dm^3 of deionized water through the column.

5.2.4 *Adsorption isotherms*

Equilibrium adsorption isotherms were obtained by addition of different amounts of powdered adsorbent to 100 ml of synthetic concentrate solution containing 30 mg dm^{-3} of NTMP. The presence of bicarbonate in the synthetic concentrate solutions ensured a constant solution pH of 7.9 ± 0.02. By the addition of 0.1 M HCl solution, an isotherm was also measured at pH 7.2 ± 0.05. The suspensions were stirred for 24 h in screw-capped flasks at 297.5 ± 0.5 K. The smaller grain size allowed for a short equilibration time. The phosphorous content was quantified with ICP as described above.

5.2.5 SDM simulations

The packed bed column modeling was carried out with the software FAST 2.0 (Fixed-bed Adsorption Simulation Tool), which has been developed by Sperlich and Schimmelpfennig (9). This software makes use of the finite differences method to solve the set of partial differential equations as given by eqs 1-5 and 8.

5.2.6 Recovery of NTMP

In order to address the possible recovery of NTMP from the regenerate solution, two methods were investigated. In the first method, NTMP was precipitated with calcium. For this, the regenerate solution was divided into eight plastic bottles of 100 ml. A hydrated lime ($Ca(OH)_2$) suspension was added to four of the bottles in a molar Ca^{2+} / NTMP ratio of 3, 7, 10 and 13, respectively. Next, a $CaCl_2$ solution was added to the other four bottles yielding a similar molar Ca^{2+} / NTMP ratio as those with the added $Ca(OH)_2$ suspension. The formed suspensions were stirred for three hours before filtering over a 0.22 μm filter. The NTMP and Ca^{2+} content of the filtrate were quantified using ICP. The air-dried precipitates were characterized by scanning electron microscopy (Jeol JSM-6480 LV) and Raman spectroscopy (Horiba/Jobin Yvon, Labram HR L/2/719). Raman spectra were recorded with; λ = 785 nm, 5 mW laser power at sample and an acquisition time of 60 s.

In the second method, the 0.1 M NaOH regeneration solution was filtered over a nano-filtration membrane (FilmTec NF270, DOW) in a dead-end stirred filtration cell operated at a pressure of 5.0 bars. About 350 mL of the regenerate solution was filtered up to a recovery of 91 %, and the concentrations of NTMP in the concentrate and the permeate were quantified.

5.3 Results and discussion

5.3.1 Equilibrium adsorption

The equilibrium for the adsorption of NTMP from the synthetic RO membrane concentrate onto GFH is best described by the Freundlich equation.

The adsorption isotherms measured at pH 7.2 and 7.9 are very similar, showing that the capacity of GFH for NTMP in the pH range 7.2 - 7.9 is the same (Figure 1).

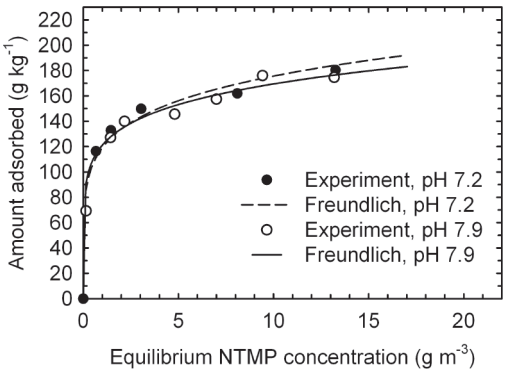

Figure 1. Equilibrium adsorption isotherms for NTMP adsorption onto GFH at different pH described by the Freundlich equation.

The Freundlich parameters a_F and n (eq 5) of the isotherm at pH 7.2 were determined to be 0.383 kg $kg^{-1}[m^3\ kg^{-1}]^n$ and 0.169 (-), respectively. At pH 7.9 these parameters were 0.332 kg $kg^{-1}[m^3\ kg^{-1}]^n$ and 0.146 (-), respectively (dry mass basis).

5.3.2 Packed bed column adsorption experiments

The breakthrough curves measured at various operating conditions are predicted reasonably well by the surface diffusion model (Figure 2). The shape of a breakthrough curve depends on the mass transfer characteristics. If mass transfer is very fast, no adsorbate will appear in the effluent before the bed is completely exhausted and the adsorbent is at equilibrium with the influent concentration. However, the results presented previously, showed that the mass transfer of NTMP into the GFH particles is controlled by the slow intraparticle diffusion process (i.e., Biot > 100) (7). As a result, breakthrough occurs while part of the bed is still far from equilibrium saturation, leading to

the typical asymptotic shape of the breakthrough curves in Figure 2. A smaller grain size can compensate for this (lower Biot number), leading to less NTMP in the effluent at the start of the experiment (Figure 2C & 2D).

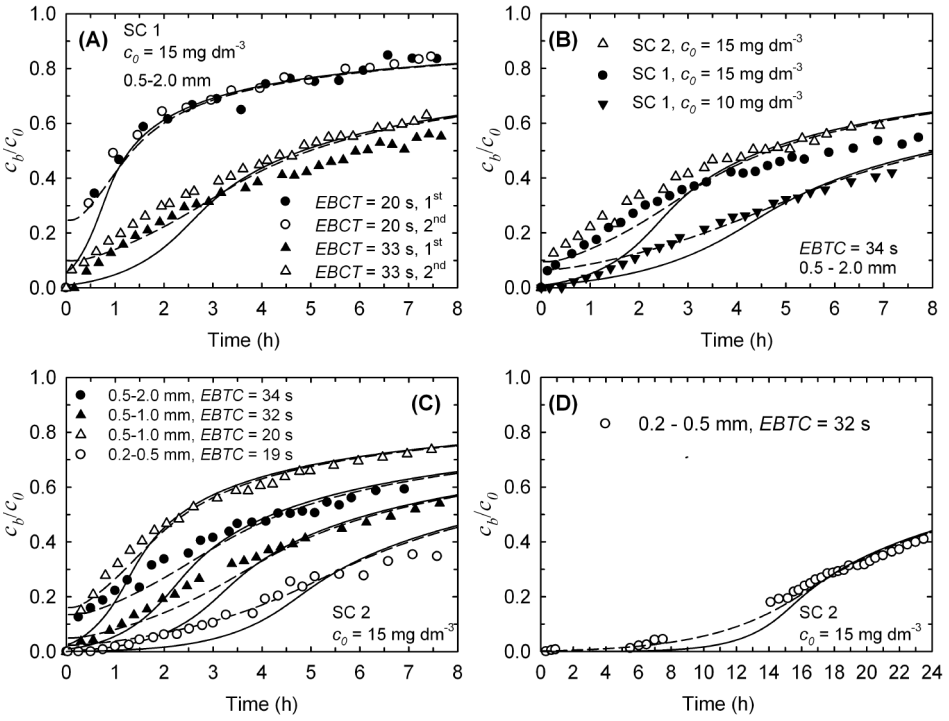

Figure 2. Comparison of experimental and theoretical concentration profiles of NTMP in a continuous operated packed bed column. (A) Effect of empty bed contact time (EBCT = w / [ρ_b/ϕ_v]) and second adsorption after bed regeneration; (B) Effect of concentrate composition; (C) Effect of particle size and EBTC; (D) Long run with small particle size. The solid lines represent the solutions of the surface diffusion model with $k_f = 2.6 \times 10^{-5}$ m s^{-1}. The dashed line represent the solutions of the surface diffusion model with $k_f = 1.3 \times 10^{-5}$ m s^{-1}.

Overall, the results correspond with what can be expected when the empty bed contact time (EBCT) decreases (i.e., lowering the flow rate or increasing the amount of adsorbent) or when the concentration of NTMP in the feed is lower; breakthrough occurs at a lower rate. Thus, a large EBCT and a small grain size are necessary to achieve sufficiently low levels of NTMP in the effluent.

In comparison with the breakthrough curve measured in solution SC 1,

only a slight difference was observed in the breakthrough curve measured in solution SC 2 (Figure 2B). It seems that the higher ionic strength and the presence of sulfate, nitrate, magnesium and potassium in solution SC 2, has a negligible effect on the adsorption process, which is in accordance with previous findings (7).

Although the external mass transfer resistance is not predominant, variation of the external film mass transfer diffusion coefficient in the numerical application of the SDM results in differences in the simulated breakthrough curves. When using the values of 2.6×10^{-5} to 3.0×10^{-5} m s^{-1} for k_f, which were previously estimated in a well-mixed basket reactor (7), the simulated breakthrough curves tend to underestimate the initial effluent concentration. When the k_f values were decreased by about half, however, the fitting improved significantly (dashed lines in Figure 2). This indicates that the external film mass transfer coefficient is lower in the column compared to the well-mixed basket reactor. Possibly, this is due to the low superficial velocity in the column. In fact, when increasing the flow rate (i.e., increasing superficial velocity) less overestimation occurred (Figure 1B). Also, the occurrence of wall effects (i.e., particles at the column wall are less densely packed than at the column centre) may occur, because of the relative low ratio of column to particle diameter. On the other hand, however, the SDM is a considerable simplification of the true adsorption process that involves combined film, pore and surface diffusion apart from sorbate-sorbent and sorbate-sorbate interactions. Therefore, a relatively low value of k_f may be needed to compensate for these and other factors that may influence the column adsorption dynamics as well.

Although the effective surface diffusivity is assumed to be constant in the surface diffusion model, it has been shown that D_s is a function of liquid and solid phase adsorbate concentration and the concentrate composition (7). Estimated values for D_s under comparable conditions ranged from 2.6×10^{-15} to 4.4×10^{-15} m^2 s^{-1}. When using D_s values within this range in the SDM, a best possible fitting of the experimental data is obtained.

5.3.3 Column regeneration

The saturated adsorption bed can be regenerated with a NaOH solution,

which causes desorption of NTMP. The efficiency, H (%), of the (batch) regeneration can be written as

$$H = \frac{\left(\overline{q_{t_e}} w - c_r V_r\right) - \overline{q_{t_e}} w}{\overline{q_{t_e}} w} 100\% \tag{12}$$

where c_r ($kg\ m^{-3}$) is the concentration of NTMP in the regeneration solution, V_r (m^3) is the volume of the regeneration solution and w (kg) is the dry weight of the adsorbent. The average amount adsorbed, $\overline{q_{t_e}}$ ($kg\ kg^{-1}$), at the end of the experiment on time t_e (s), is

$$\overline{q_{t_e}} w = \varphi_v \int_0^{t_e} \left(c_0 - c_b\right) dt \tag{13}$$

Following the desorption step with NaOH, the bed was flushed with deionized water. Apparently, this washing with deionized water removes part of the remainder of adsorbed NTMP from the GFH particles because the second adsorption steps do not deviate significantly from the first ones (Figure 2A), especially when a high regeneration efficiency was reached in the desorption step. The regeneration efficiency improves with increasing solution volume, V_r, to bed volume, V_b, ratio (Figure 3). This indicates that a large volume of a NaOH solution would be needed to approach 100 % efficiency. Therefore, an additional process that can separate the desorbed NTMP from the regeneration solution is mandatory.

5.3.4 Phosphonate recovery

Separation of the NTMP from the regeneration solution may offer a way to recover the phosphonate and reuse it as antiscalant in the RO membrane filtration process. The reuse of regeneration solution is desired from both an economical and an environmental point of view. Therefore, two methods for the removal of the NTMP from the regeneration solution were investigated.

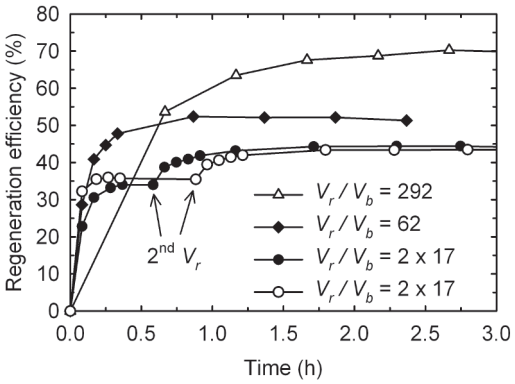

Figure 3. Regeneration efficiency as a function of time in terms of the V_r / V_b ratio. A 0.1 M NaOH solution was used.

In the first method, NTMP was precipitated with different amounts of calcium which was added in the form of either $CaCl_2$ or $Ca(OH)_2$ (Table 2).

Table 2. Results of Ca^{2+}-NTMP precipitation from the regeneration solution at pH 13.

Calcium source	**Ca^{2+}/NTMP solution**	**Ca^{2+}/NTMP precipitate**	**$[NTMP]_{3h}$** ($g\ m^{-3}$)	**$[Ca^{2+}]_{3h}$** ($g\ m^{-3}$)	**NTMP removed (%)**
$CaCl_2$	3 : 1	2.2 : 1	120.7	80.8	60.4
	7 : 1	2.5 : 1	27.2	174.4	91.1
	10 : 1	2.7 : 1	13.1	289.6	95.7
	13 : 1	3.0 : 1	9.4	403.8	96.9
$Ca(OH)_2$	3 : 1	2.6 : 1	134.1	75.2	56.0
	7 : 1	3.8 : 1	35.7	127.6	88.3
	10 : 1	5.9 : 1	22.0	172	92.8
	13 : 1	9.8 : 1	25.2	154.4	91.7

The precipitates formed by addition of $CaCl_2$ have a Ca^{2+} / NTMP molar ratio in the range of 2 : 1 and 3 : 1. On the other hand, the molar ratio of the precipitates seem to increase rapidly with an increasing amount of $Ca(OH)_2$ added. Due to its low solubility, $Ca(OH)_2$ was added as a suspension. Therefore, the Ca^{2+} / NTMP ratio in these precipitates could not be determined accurately, because it

is difficult to distinguish between solid $Ca(OH)_2$ and the Ca^{2+} - NTMP precipitate.

From the SEM analysis it appeared that the Ca^{2+}- NTMP precipitates consisted of round shaped nanoparticles with sizes of approximately 100 nm (Figure 4A). The sharp bands in the Raman spectra (Figure 4B) indicate that the precipitates are crystalline. Considering the great complexity of the Ca^{2+}- NTMP unit cell and the absence of reference spectra, identification of all the vibrational modes is out of question.

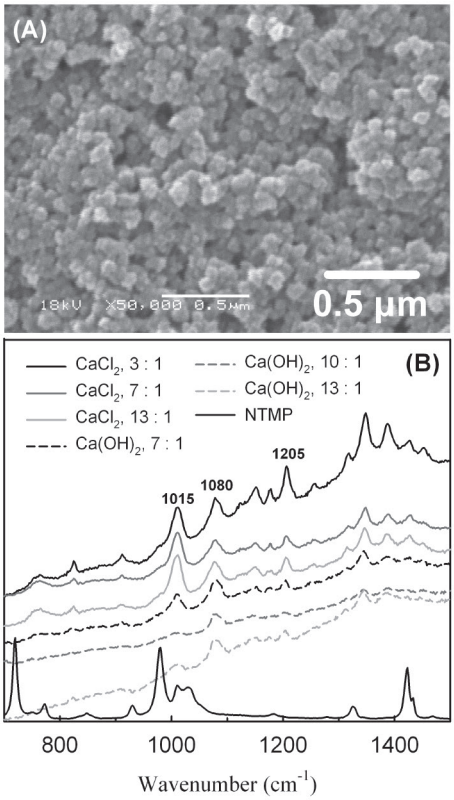

Figure 4. (A) SEM picture of a Ca^{2+}-NTMP precipitate ($CaCl_2$, 3 : 1); (B) Raman spectra of the different Ca^{2+}- NTMP precipitates and pure NTMP.

However, some assignments may be given in the 900 - 1200 cm^{-1} wavenumber range, where the bands associated with various P–O(H) vibrations can be found (14). The two dominating bands at 1015 and 1080 cm^{-1} observed for the Ca^{2+} - NTMP precipitates most likely correspond to asymmetric stretching vibration $\nu_{as}(PO_3^{2-})$ and stretching vibration $\nu_s(PO_3^{2-})$.Compared to the spectrum measured for pure NTMP, these bands are shifted to higher wavenumbers in the presence of calcium. The band at 1205 cm^{-1} corresponds with the P=O bond.

Ca^{2+} - phosphonate precipitation has been investigated before because of its importance in deep well treatment in the production of oil (15, 16). For the phosphonate NTMP, the existence of precipitates with different Ca^{2+} / NTMP molar ratios were reported depending on precipitation conditions (17, 18). Also, the solubility of the Ca^{2+}- NTMP precipitate is known to be dependent on this Ca^{2+} / NTMP ratio and the crystallinity of the precipitate. With increasing Ca^{2+} / NTMP molar ratio and crystallinity, the equilibrium solubility limit decreases. This strongly suggests that a crystalline product with a high Ca^{2+} / NTMP ratio is more suitable for removing NTMP from the regeneration solution.

Although much is known about the precipitation of calcium-phosphonate at pH below 8.5, there is a considerable lack of literature on Ca^{2+}-phosphonate precipitation at high pH values. This work shows that it is possible to precipitate Ca^{2+}- NTMP at high pH. A high pH may facilitate the binding of NTMP with calcium cations, because NTMP is completely deprotonated.

A second method to recover the NTMP from the regenerate solution is by treating the solution with nano-filtration. The nano-filtration membrane is able to retain NTMP in the concentrate up to a recovery of 91 % (Table 3).

Table 3. Results of nano-filtration of the NaOH regeneration solution.

c_0 ($g\ m^{-3}$)	Retention (%)	NTMP conc. concentrate ($g\ m^{-3}$)	NTMP conc. permeate ($g\ m^{-3}$)	NaOH solution recovery (%)
200	99.4	701	1.2	70
200	99.4	2065	1.2	91

The concentrate solution with the increased NTMP concentration may be a suitable source for NTMP antiscalant in the RO desalination process. Nano-filtration seems to be technical more feasible compared to the precipitation method, because the NTMP removal efficiency is highest, and the phosphonates can be recovered without the presence of excess calcium. The calcium that remains in the regeneration solution after the precipitation step (Table 2) might cause Ca^{2+} - NTMP precipitation in the adsorption column when reusing the regeneration solution. A disadvantage of filtering the basic regenerate solution with a nano-filtration membrane is the need of special, hence, expensive, pH stable membranes.

5.4 Conclusions

A packed bed column filled with granular ferric hydroxide (GFH) can be used to recover the phosphonate antiscalant NTMP from RO membrane concentrates. The adsorption dynamics of the column can be predicted reasonably well by a surface diffusion model. The slow intraparticle diffusion process dictates long empty bed contact times and small grain sizes in order to achieve sufficiently low levels of NTMP in the column effluent. The successful regeneration of saturated sorbent particles by using sodium hydroxide solution was demonstrated. This regeneration improves with increasing solution volume to bed volume ratio. The desorbed NTMP in the sodium hydroxide solution can be recovered by precipitation with calcium or by nano-filtration, although the latter seems to be technical more feasible.

5.5 Acknowledgements

This work was performed in the TTIW-cooperation framework of Wetsus, Centre of Excellence for Sustainable Water Technology (www.wetsus.nl). Wetsus is funded by the Dutch Ministry of Economic Affairs, the European Union Regional Development Fund, the Province of Fryslân, the City of Leeuwarden and the EZ/Kompas program of “Samenwerkingsverband Noord-Nederland”. The authors like to thank the participants of the research

theme Concentrates for the discussions and their financial support. We would especially like to thank Arie Zwijnenburg for his assistance with the membrane filtration cell. We gratefully acknowledge GEH Wasserchemie by providing us with a free sample of GFH.

5.6 Nomenclature

a_F	constant in the Freundlich isotherm	kg kg^{-1}(m^3 kg^{-1})^n
c_0	initial liquid-phase concentration	kg m^{-3}
c_b	concentration at any time t	kg m^{-3}
c_r	concentration in regeneration solution	kg m^{-3}
D_m	molecular diffusivity	m^2 s^{-1}
D_s	effective surface diffusivity	m^2 s^{-1}
$EBCT$	empty bed contact time, $EBCT = w/(\rho_b \varphi_v)$	s
ε_b	bed porosity	-
η_b	dynamic viscosity	Pa s
H	efficiency	%
k_f	external film mass transfer coefficient	m s^{-1}
L	length of the bed	m
M_b	molecular weight solvent	kg mol^{-1}
n	exponent in the Freundlich isotherm	-
q	amount adsorbed on the surface	kg kg^{-1}
q_0	value of q corresponding to c_0	kg kg^{-1}
$\overline{q_{t_e}}$	average amount adsorbed at time t_e	kg kg^{-1}
r	radial coordinate of the particle	m
R_0	particle radius	m
ρ	liquid density	kg m^{-3}
ρ_b	bed density	kg m^{-3}
ρ_p	particle density	kg m^{-3}
t	time	s
T	absolute temperature	K
V_b	volume of absorbent bed	m^3
v_f	superficial bed velocity	m s^{-1}

V_m	molar volume	$m^3\ mol^{-1}$
V_r	volume of regeneration solution	m^3
ϕ_v	fluid flow rate	$m^3\ s^{-1}$
w	weight of adsorbent	kg
ξ	association parameter	(-)
z	axial coordinate of the bed	m

Dimensionless variables and groups

Bi	Biot number	$Bi = k_f R_0 c_0 / \rho_p D_s q_0$
C_b	concentration of adsorbate in liquid phase	$C_b = c_b / c_0$
C_s	adsorbate concentration at the sphere surface ($r = R_0$)	$C_s = c_s / c_0$
D_g	solute distribution parameter	$D_g = \rho_b q_0 / (\varepsilon_b c_0)$
Q	amount adsorbed on the surface	$Q = q / q_0$
Re	Particle Reynolds number	$Re = \rho v_f 2R_0 / \eta_b (1 - \varepsilon_b)$
Sc	Schmidt number	$Sc = \eta_b / \rho D_m$
Sh	Sherwood number	$Sh = k_f 2R_0 / D_m$
St	modified Stanton number	$St = k_f w / (\rho_p R_0 \varphi_v)$
τ	time for SDM	$\tau = t \rho_b \varphi_v / (w \varepsilon_b D_g)$
Z	axial coordinate of the bed	$Z = z / L$
R	particle radius	$R = r / R_0$

5.7 References

(1) Squire, D. Reverse osmosis concentrate disposal in the UK. *Desalination* **2000**, *132*, 47-54.

(2) Nederlof, M. M.; van Paassen, J. A. M.; Jong, R. Nanofiltration concentrate disposal: experiences in The Netherlands. *Desalination* **2005**, *178*, 303-312.

(3) Nederlof, M. M.; Hoogendoorn, J. H. Desalination of brackish groundwater: the concentrate dilemma. *Desalination* **2005**, *182*, 441-447.

(4) Lattemann, S.; Höpner, T. Environmental impact and impact assessment of seawater desalination. *Desalination* **2008**, *220*, 1-15.

(5) Hoepner, T.; Lattemann, S. Chemical impacts from seawater desalination plants

a case study of the northern Red Sea. *Desalination* **2003**, *152*, 133-140.

(6) Cordell, D.; Drangert, J.-O.; White, S. The story of phosphorus: global food security and food for thought. *Global Environ. Change* **2009**, *19*, 292-305.

(7) Boels, L.; Keesman, K. J.; Witkamp, G. J. Adsorption of phosphonate antiscalant from reverse osmosis membrane concentrate onto granular ferric hydroxide. *Environ. Sci. Technol.* **2012,** DOI: 10.1021/es302186k.

(8) Badruzzaman, M.; Westerhoff, P.; Knappe, D. R. Intraparticle diffusion and adsorption of arsenate onto granular ferric hydroxide (GFH). *Water Res.* **2004**, *38*, 4002-4012.

(9) Sperlich, A.; Schimmelpfennig, S.; Baumgarten, B.; Genz, A.; Amy, G.; Worch, E.; Jekel, M. Predicting anion breakthrough in granular ferric hydroxide (GFH) adsorption filters. *Water Res.* **2008**, *42*, 2073-2082.

(10) Wakao, N.; Funazkri, T. Effect of fluid dispersion coefficients on particle-to-fluid mass transfer coefficients in packed beds: correlation of sherwood numbers. *Chem. Eng. Sci.* **1978**, *33*, 1375-1384.

(11) Wilke, C. R.; Chang, P. Correlation of diffusion coefficients in dilute solutions. *AIChE J.* **1955**, *1*, 264-270.

(12) Durchschlag, H.; Zipper, P. Calculation of the partial volume of organic compounds and polymers. *Progr. Colloid Polym. Sci.* **1994**, *94*, 20-39.

(13) Schwertmann, U., Cornell, R.M. *Iron Oxides in the Laboratory*, Wiley-VCH Verlag GmbH: Weinheim, Germany, 2001.

(14) Zenobi, M. C.; Luengo, C. V.; Avena, M. J.; Rueda, E. H. An ATR-FTIR study of different phosphonic acids in aqueous solution. *Spectrochim. Acta A* **2008**, *70*, 270-276.

(15) Kan, A. T.; Oddo, J. E.; Tomson, M. B. Formation of two calcium diethylenetriaminepentakis(methylene phosphonic acid) precipitates and their physical chemical properties. *Langmuir* **1994**, *10*, 1450-1455.

(16) Browning, F. H.; Fogler, H. S. Effect of synthesis parameters on the properties of calcium phosphonate precipitates. *Langmuir* **1995**, *11*, 4143-4152.

(17) Pairat, R.; Sumeath, C.; Browning, F. H.; Fogler, H. S. Precipitation and dissolution of calcium-ATMP precipitates for the inhibition of scale formation in porous media. *Langmuir* **1997**, *13*, 1791-1798.

(18) Tantayakom, V.; Fogler, H. S.; de Moraes, F. F.; Bualuang, M.; Chavadej, S.; Malakul, P. Study of Ca-ATMP precipitation in the presence of magnesium ion. *Langmuir* **2004**, *20*, 2220-2226.

SEEDED CALCITE SONOCRYSTALLIZATION

6

The seeded sonocrystallization of calcite was investigated by measuring the volumetric crystallization rate at constant composition conditions. The crystallization rate of calcite was enhanced by 46 % through ultrasonic irradiation (42,150 Hz, 17 W dm^{-3}) of a supersaturated crystal suspension. It was shown that this effect was related to the alteration of the seed crystals' habit and size. During ultrasonic irradiation, disruption of conglomerates and erosion of single crystals occurred, accompanied by the production of many fines. The increased surface area available for crystal growth resulted in the observed crystallization rate enhancement.

This chapter has been published as:

Boels, L.; Wagterveld, R. M.; Mayer, M. J.; Witkamp, G. J. Seeded calcite sonocrystallization. *J. Cryst. Growth* **2010**, *312*, 961-966.

6.1 Introduction

Ultrasound can help controlling the course of crystallization processes. This is also referred to as sonocrystallization. Sonocrystallization received much attention the last decade due to its positive effects in crystallization processes for the synthesis of pharmaceuticals and proteins (1-9), organic compounds (10-12) and inorganic compounds (13-21). Many effects are ascribed to the ultrasonic treatment. Both an increased and a retarded crystal growth rate were reported (2, 4-6, 10, 14, 15, 19). The same holds for the increase (9) and decrease (3, 4, 6, 8, 9, 12, 16-19, 21, 22) of induction periods. A few papers mention a decrease of the metastable zone width (8, 10, 13, 14, 18) as well as an enhanced solubility of a sparingly soluble salt (20). Furthermore, effects are seen on the mean particle size (1, 2, 5-7, 9, 11-13, 16, 21), the particle size distribution and crystal morphology (1, 2, 5-7, 10-14, 16).

Acoustic streaming and cavitation are the most important phenomena that occur when ultrasound is passed through a liquid-solid system. These phenomena can produce a series of unique chemical and physical effects. In acoustic streaming, acoustic waves produce a stirring effect. In the vicinity of the crystal surfaces, this stirring effect causes a reduction of the diffusion layers' thickness, thereby increasing the liquid-solid mass transport (23). In addition, ultrasound produces small imploding cavities that generate high-energy shock waves, which impinge on the particle surface. This can create high velocity interparticle collisions that can alter the particle morphology and size dramatically. It was reported that these interparticle collisions occur with such a great force that even metal particles tend to melt together (24). Microjet formation in the vicinity of the particle surface is another well-established mechanism for accounting the effect of cavitation in solid-liquid systems. However, in literature it is mentioned that this mechanism can only occur if the surface is several times larger than the resonant bubble size (25).

Calcium carbonate is one of the most abundant minerals, and the problem of its scaling propensity is encountered in many industrial water treatment processes. Although the topic of sonocrystallization has received much attention the last decade, the effect of ultrasonic irradiation on the

precipitation of calcium carbonate has hardly been investigated and therefore the literature on this topic is sparse. Dalas (15) reported a retarded crystal growth in the presence of ultrasonic irradiation. No effect of this irradiation on the nature, morphology or the size of the formed calcium carbonate crystals was observed. In the study conducted by Nishida (19), it was observed that the spontaneous precipitation of calcium carbonate was enhanced in the presence of ultrasonic irradiation. It was suggested that this was due to an enhanced nucleation rate during the ultrasonic treatment. Furthermore, this research confirmed the observations of Dalas that neither the morphology nor the size of the calcium carbonate crystals was affected by the ultrasonic irradiation. Berdonosov and co-workers (26) found that the transition of metastable vaterite to calcite can be enhanced by ultrasonic irradiation. It was suggested that this effect was related to energetic collisions between vaterite and calcite particles.

Considering the physical effects that occur due to cavitation, it is reasonable to expect that the habit and size of calcium carbonate crystals can be altered through ultrasonic irradiation. The aim of the present work is to investigate whether or not this occurs. For this purpose the volumetric crystal growth rate (i.e., crystallization rate) of calcite seed crystals during ultrasonic irradiation was measured using the proven constant composition methodology (27, 28). If the habit and/or size of the seed crystals can be indeed affected, the volumetric crystal growth rate should also change. Therefore, the crystallization rate after the irradiation period was also measured.

6.2 Experimental procedure

Only analytical grade reagents, high quality water (Milli-Q Reagent Water System, resistivity > 18 MΩ cm) and grade A glassware were used throughout the experiments. Calcite seed crystals were prepared, using the method described by Reddy and Nancollas (29), by slowly adding 2 dm^3 of a 0.20 M calcium chloride solution to 2 dm^3 0.20 M sodium carbonate solution at 25 °C. The freshly precipitated seed crystals were aged overnight in mother liquor and were subsequently washed with Milli-Q water each day for one week. Afterwards, the washed seed crystals were aged for three weeks before

filtering. The dried crystals were characterized by scanning electron microscopy (Jeol JSM-6480 LV), nitrogen adsorption (Micromeritics Tristar 3000) and ATR-FT-IR spectroscopy (Shimadzu 4800). The specific surface area of the seed crystals was found to be 0.17 m^2 g^{-1} as determined with a five-point BET method (30) on 3 replicate samples. The ATR-FT-IR spectra showed characteristic adsorptions for calcite at 1795, 1392, 871 and 711 cm^{-1}. The characterization confirmed the crystals to be pure calcite and appeared as interpenetrated conglomerates.

A double walled thermostated glass reactor equipped with a floating magnetic stirrer bar to minimize any grinding effects, a by-pass loop and an ultrasonic transducer were used (Figure 1).

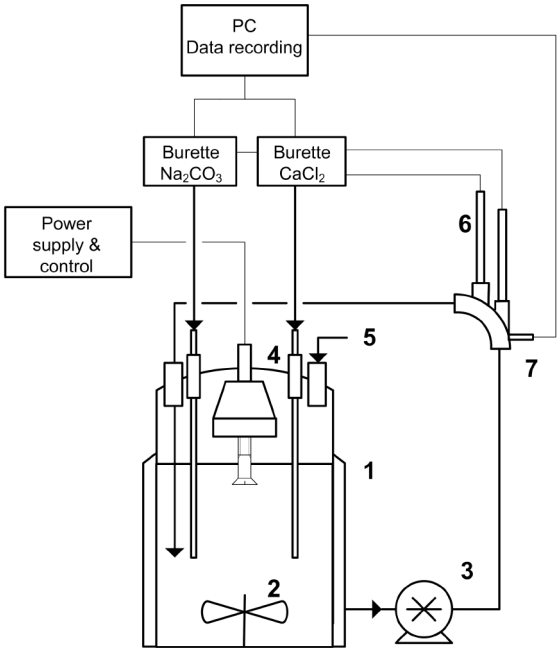

Figure 1. Scheme of the constant-composition experimental set-up consisting of 1) a double walled glass reactor, 2) floating magnetic stirrer bar, 3) membrane pump, 4) ultrasonic transducer, 5) free port for seed addition, 6) pH electrode and reference electrode, 7) and a temperature sensor.

The ultrasonic transducer was part of a dedicated homebuilt system that could be controlled precisely in terms of shape, frequency and amplitude of the alternating current for driving the transducer. For the control of pH, a combined Pt-ring pH electrode and a shielded Ag/AgCl reference electrode in combination with two coupled automatic burettes (Metrohm Titrino 785 and Dosimat 665) were used. In order to avoid any possibility of damaging the electrodes by the ultrasonic irradiation, both electrodes and a temperature sensor were positioned in a glass cell in the by-pass stream. A positive displacement membrane pump was used to pump the crystal suspension with 1.5 dm^3 min^{-1} through the by-pass.

Metastable working solutions were prepared by slow addition of 500 cm^3 of a 4 mM calcium solution to 500 cm^3 of a 4 mM bicarbonate solution in the reactor. Fresh titrant solutions were prepared every day as shown in Table 1. Potassium chloride was added to all solutions to maintain the ionic strength constant at 0.1 M.

Table 1. Composition of the titrant solutions.

Reagent	**Calcium titrant** ***(mM)***	**Carbonate titrant** ***(mM)***
$CaCl_2.2H_2O$	53.0	-
$NaHCO_3$	-	4.0
Na_2CO_3	-	49.0
KCl	38.0	46.0

The working solution was stirred at 500 rpm. The pH of the stable working solution was adjusted to the desired value of 8.500 ± 0.002 using a 0.05 M KOH solution. The stability of the working solution was verified by observing a constant pH for at least 45 min. After the addition of 0.250 g dry seed crystals, the solution pH started to decrease as a result of calcite precipitation. This triggered the automatic burettes to add concurrently equivalent amounts of calcium chloride and sodium carbonate solutions in order to achieve and maintain the pH at the target value (± 0.002 pH units). In this way, a constant degree of supersaturation was maintained throughout the

growth experiment.

After 30 min of normal growth, the ultrasonic irradiation was initiated. The solution was treated with ultrasound for 45 min at a frequency of 42,150 Hz and with an intensity of 17 W or 7.1 W cm^{-2} (real output power intensity pre-determined by measuring the adiabatic temperature rise in time using a similar well isolated glass reactor filled with 1 dm^3 of water). The volume of added titrant solution was monitored over time and this data represented the calcium carbonate precipitation rate. During the experiment, aliquots of solution were rapidly removed, filtered through a 0.2 μm filter and analyzed for the calcium content with inductive-coupled plasma spectrometry (Optima 3000XL, Perkin-Elmer) to verify the constancy of the degree of supersaturation.

After the ultrasonic treatment the crystals were allowed to grow for another 75 min at the same supersaturation. All experiments were conducted at atmospheric pressure with ambient levels of CO_2. By keeping the reactor lid closed and all ports sealed during the experiments, the exchange of atmospheric CO_2 with the reactor solution was minimized. Seed addition and reactor sampling were performed as rapidly as possible. The temperature was maintained constant at 25 ± 0.1 °C by circulating water from a thermo bath through the jacket of the reactor. During the ultrasonic irradiation, the thermo-bath was set to cool in order to keep the reaction mixture temperature at 25 ± 0.1 °C.

In order to investigate the effect of ultrasound on the crystal habit, 0.250 g dry seed crystals were added to a 1 dm^3 saturated calcium carbonate solution and the resulting suspension was stirred and treated with ultrasound in the same way as during the growth experiments. Throughout the experiment, samples of 15 cm^3 of solution were collected and filtered through a 0.2 μm filter. After drying, the samples were analyzed with SEM.

For comparison, the experiment was repeated with a stirred saturated suspension without applying ultrasound (control). Afterwards, both suspensions were transferred to a particle size and shape (video) analyzer equipped with a liquid flow cell (Eyetech, Ankersmid) in order to measure the number distributions of the particle size. Three replicate analyses were

performed in which 5000 particles were analyzed to reach a confidence level above 99 %.

6.3 Results and discussion

The driving force for crystallization can be expressed as

$$\frac{\Delta\mu}{\mathbf{R}T} = \ln(S) \quad (1)$$

where **R** ($J\ mol^{-1}\ K^{-1}$) is the gas constant, T (K) is the absolute temperature, $\Delta\mu$ ($J\ mol^{-1}$) is the change in chemical potential, and S (-) is the supersaturation. For $CaCO_3$, S is best expressed in terms of the solubility product

$$S = (IAP/K_{sol})^{1/\upsilon} \quad (2)$$

where IAP is the ion activity product, K_{sol} (3.36×10^{-9}) (31), is the solubility product, and υ (-) is the number of ions in the formula unit. The supersaturation, S, with respect to calcite of the working solution used here was calculated to be 2.11 (software: Visual Minteq v2.53, model: Davies) and the change in chemical potential, $\Delta\mu$, of transfer from supersaturated solution to equilibrium, measured 1.85 kJ mol^{-1}.

If the surface area of the used seed crystals is known, the constant linear calcite growth rate, R ($mol\ m^{-2}\ s^{-1}$), can be easily obtained from the initial slope of the titrant addition versus time curve. However, growth leads to an increase of crystal volume and an accompanying increase of surface area. This causes the slope of the titrant addition versus time curve to increase over time. The first time derivative of the added volume of Ca^{2+} titrant is denoted here as the (volumetric) crystallization rate ($cm^3\ s^{-1}$).

Figure 2 shows three datasets of constant composition calcite growth experiments (control), and two datasets of similar experiments but with 45 min of ultrasonic treatment (ultrasound).

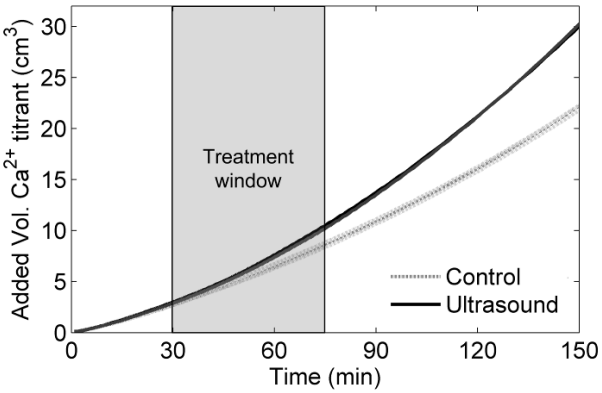

Figure 2. Titrated volume of Ca^{2+} vs. time of constant composition calcite growth experiments: three sets of control experiments and two sets with ultrasonic treatment (start after 30 min) Experimental conditions: S = 2.11, pH = 8.500, T = 25 °C.

A cubic regression was used to fit the control experiments and their average. The linear growth rate can be derived from the first order constant (32, 33). The first 15 min show an initial growth surge. This period is excluded from the fit. The growth rate was estimated to be 1.82×10^{-6} mol m^{-2} s^{-1} (i.e., 6.76×10^{-11} m s^{-1}) (Table 2). The results in Figure 2 and Table 2 reveal that the experiments were highly reproducible. Furthermore, the measured growth rate corresponds well with values found in literature (34). This suggests that the experimental set-up is suitable to study the effect of ultrasound on the crystallization of calcium carbonate.

Table 2. Growth rate derived from a cubic fit of three experimental data sets and their average. Experimental conditions: S = 2.11, [Ca] = [CO_3] = 2 mM, pH = 8.500, T = 25 °C.

Experiment	**Rate, *R*** ***(mol m^{-2} s^{-1})***	**SSE[(a)]**	**R^2**
Control 01	1.77×10^{-6}	0.1170	0.999996
Control 02	1.98×10^{-6}	0.1275	0.999995
Control 03	1.70×10^{-6}	0.1199	0.999995
Average	1.82×10^{-6}	0.0388	0.999999

(a) sum of squares error

After the ultrasonic irradiation is started, the slope of the ultrasound curves starts to increase faster compared to the slope of the control curves (Figure 2). This effect is more clearly seen in Figure 3, where the crystallization rate of the average values of control and ultrasound datasets are plotted as function of time. At the start of the ultrasonic treatment at t = 30 min, the crystallization rate of the ultrasonic treatment shows a clear increase compared to the control curve.

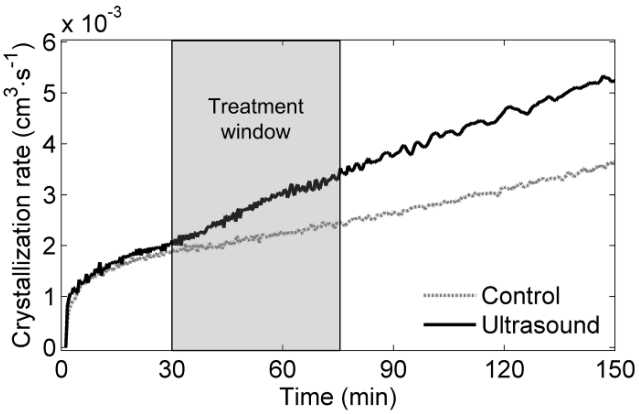

Figure 3. Crystallization rate (volumetric) defined as the time derivative of the added volume of Ca^{2+} titrant ($cm^3\ s^{-1}$). A moving average (span = 15 of 448 data points) was used on all datasets.

After termination of the ultrasonic treatment (t = 75 min), when all conditions are exactly the same compared to the control experiments, the ratio of both crystallization rates remains the same. This is demonstrated in Figure 4 where the ratio between the ultrasound and control crystallization rates is shown. Before the ultrasonic treatment, this ratio is close to 1 during the first 30 min. Then, the figure shows a clear increase of crystallization rate during the treatment and approaches a final value of approximately 46 % after the treatment. After termination of the ultrasonic treatment, there is no decline in precipitation rate. This indicates that the enhanced precipitation rate is caused by permanent physical changes of the seed crystals, and not by a temporarily enhancement of the liquid-solid mass transport.

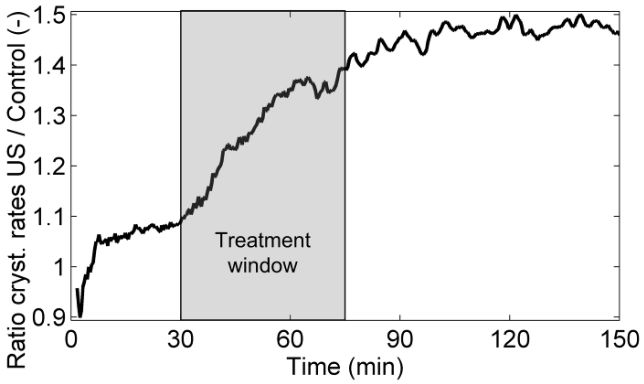

Figure 4. Ratio of crystallization rates: Ultrasound / Control (-). The increase in crystallization rate caused by the ultrasonic irradiation is approx. 46 %.

The retardation effect reported by Dalas (15) was not observed. The precipitation rate already increased during the ultrasonic treatment. It is possible that this suggested retardation effect was camouflaged because of the relatively large increase in crystal reactivity. The used calcite seeds and supersaturation levels in both studies are quite similar. However, the differences in the ultrasonic field applied and the way the pH was measured during the ultrasonic irradiation differed markedly. Therefore, the causes of the contradictory observations remain unclear.

The SEM pictures of the crystals at the end of the growth experiments (t = 150 min) showed no clear difference between the control and ultrasound experiments. Nevertheless, the effect of ultrasonic irradiation on the crystals could easily be observed from the samples taken during the treatment period in a saturated solution (i.e., without growth). In Figures 5 and 6, SEM pictures of respectively untreated and treated seed crystals in a saturated solution are shown. These pictures are a cross selection of 21 pictures taken from 7 samples. The appearance of some fines in Figure 5B can be explained in two ways. First, the introduction of the dry seed crystals probably led to some initial breeding. Second, the seeds may have experienced some attrition due to the pumping and stirring action in the set-up. Attrition may contribute to the increasing slope of the control growth curves. In Figure 6, seed crystals treated with ultrasound are

shown. It can be seen that in the first period the interpenetrated conglomerates were disrupted. At the end of the ultrasound treatment, numerous fine particles and many damaged crystals were observed. Because supersaturation was absent in these experiments, the appearance of these fine particles can be subscribed to the attrition and breakage of the parent crystals during the ultrasonic treatment. Although the same mechanism is expected to have played a pivotal role in the actual growth experiments, it is not possible to exclude nucleation mechanisms driven by supersaturation.

The production of fines and the erosion of the parent seed crystals by the action of the ultrasonic irradiation caused a rapid increase of the total surface area available for growth. It is likely that the rapid healing of the fractured parent crystals and the outgrowth of fines after the ultrasonic irradiation period in the growth experiments camouflaged any differences in crystal habit at the end. Furthermore, the wide crystal size distribution of the seed crystals makes it difficult to distinguish grown particle fragments from original small seeds.

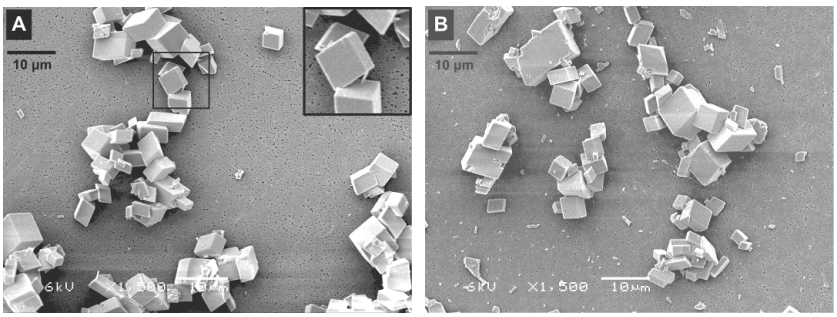

Figure 5. SEM pictures of untreated seed crystals in a saturated solution: (A) Starting seeds; (B) After 60 min stirring and pumping.

Besides calcite, other polymorphs of calcium carbonate are aragonite and vaterite. Although the preference for the calcite polymorph is thermodynamically favored under the experimental conditions of the bulk liquid (i.e., 25 °C & 1 atm pressure) (29), the local conditions in the vicinity of an imploding cavity are significantly different (23). It is questionable, however, if the change in local conditions is maintained for a sufficient time to allow the growth of a different polymorph.

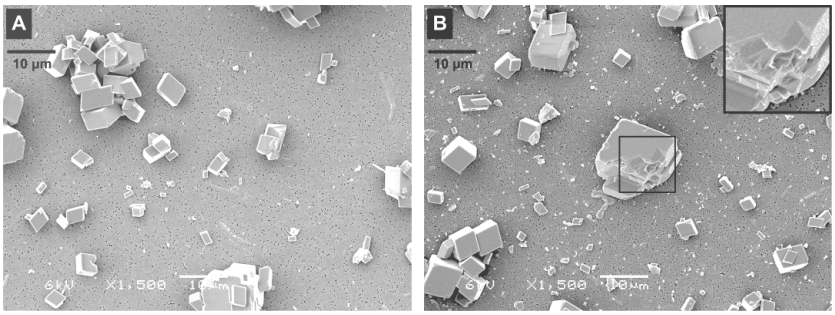

Figure 6. SEM pictures of seed crystals treated with ultrasound in a saturated solution: (A) After 5 min; (B) after 45 min of ultrasonic irradiation.

In addition, the presence of calcite seeds kinetically dictates the growth of this polymorph. Also, ATR-FT-IR spectra of the grown seeds did not show any characteristic adsorptions other than those for calcite. Therefore, it is reasonable to expect that no other polymorphs grew besides calcite.

The particle size distributions by number of the treated and untreated seed crystals are shown in Figure 7. Note that the lower detection limit of the particle size measurement was 1.5 µm. Therefore, the large number of fines present in the treated samples according to the SEM pictures did not contribute to these distributions. Although the small seeds and seed fragments were not counted, there is a shift in the distributions. The arithmetic (number - length) mean of the number distribution (Figure 7A) shifts from 10.3 to 8.9 µm. This indicates that there is a decrease in the number of larger particles (note the drop in the distribution between 10 and 20 µm) and the number of particles in the lower part of the distribution increases (1.5 – 3.2 µm). This shows that the seed crystals are fragmented into smaller parts. These observations are in line with the SEM analysis.

The SEM and particle size analysis showed that the physical effects that occurred during ultrasonic irradiation gave rise to a change in the habit and particle size of the calcite crystals.

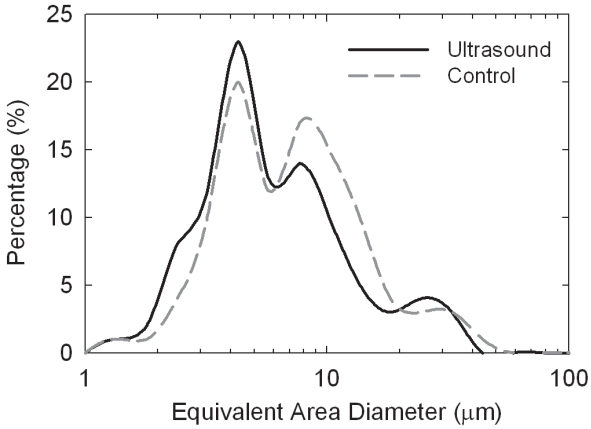

Figure 7. Particle size distribution (equivalent area diameter) by number of the untreated and treated seed crystals.

The resulting increment of the surface area is a major factor in the observed growth rate enhancement. In addition, the much higher density of active growth sites (i.e., kinks) on the fractured crystal surfaces facilitates a higher growth rate compared to the ripened smooth crystal surfaces. It is well known, however, that these fractured crystal surfaces rapidly heal and proceed to grow at a much slower rate (35). This could explain why the ratio between the ultrasound and control crystallization rates in Figure 4 is still increasing right after termination of the ultrasonic treatment before it reaches a constant value.

6.4 Conclusions

The effect of ultrasound on the seeded calcite crystallization was investigated. A dedicated experimental set-up based on the constant composition method gave highly reproducible results. It was shown that the volumetric crystallization rate was increased by 46 % after 45 min of ultrasonic irradiation (17 W dm^{-3}). Control experiments without supersaturation showed that during the irradiation period, seed crystals were disrupted and many fines appeared. SEM and particle size analysis showed that it is possible to alter the habit and size of the calcite crystals through ultrasonic irradiation. The

increased surface area available for crystal growth resulted in the observed crystallization rate enhancement.

6.5 Acknowledgements

This work was performed in the TTIW-cooperation framework of Wetsus, Centre of Excellence for Sustainable Water Technology (www.wetsus.nl). Wetsus is funded by the Dutch Ministry of Economic Affairs, the European Union Regional Development Fund, the Province of Fryslân, the City of Leeuwarden and the EZ/Kompas program of "Samenwerkingsverband Noord-Nederland". The authors like to thank the participants of the research theme "Concentrates" and theme "Sensoring" for the discussions and their financial support.

6.6 References

(1) Abbas, A.; Srour, M.; Tang, P.; Chiou, H.; Chan, H. K.; Romagnoli, J. A. Sonocrystallisation of sodium chloride particles for inhalation. *Chem. Eng. Sci.* **2007**, *62*, 2445-2453.

(2) Dennehy, R. D. Particle engineering using power ultrasound. *Org. Process Res. Dev.* **2003**, *7*, 1002-1006.

(3) Guo, Z.; Zhang, M.; Li, H.; Wang, J.; Kougoulos, E. Effect of ultrasound on anti-solvent crystallization process. *J. Cryst. Growth* **2005**, *273*, 555-563.

(4) Kakinouchi, K.; Adachi, H.; Matsumura, H.; Inoue, T.; Murakami, S.; Mori, Y.; Koga, Y.; Takano, K.; Kanaya, S. Effect of ultrasonic irradiation on protein crystallization. *J. Cryst. Growth* **2006**, *292*, 437-440.

(5) Li, H.; Wang, J.; Bao, Y.; Guo, Z.; Zhang, M. Rapid sonocrystallization in the salting-out process. *J. Cryst. Growth* **2003**, *247*, 192-198.

(6) Li, H.; Li, H.; Guo, Z.; Liu, Y. The application of power ultrasound to reaction crystallization. *Ultrason. Sonochem.* **2006**, *13*, 359-363.

(7) Louhi-Kultanen, M.; Karjalainen, M.; Rantanen, J.; Huhtanen, M.; Kallas, J. Crystallization of glycine with ultrasound. *Int. J. Pharm.* **2006**, *320*, 23-29.

(8) Luque de Castro, M. D.; Priego-Capote, F. Ultrasound-assisted crystallization (sonocrystallization). *Ultrason. Sonochem.* **2007**, *14*, 717-724.

(9) Miyasaka, E.; Ebihara, S.; Hirasawa, I. Investigation of primary nucleation

phenomena of acetylsalicylic acid crystals induced by ultrasonic irradiation—ultrasonic energy needed to activate primary nucleation. *J. Cryst. Growth* **2006**, *295*, 97-101.

(10) Kordylla, A.; Koch, S.; Tumakaka, F.; Schembecker, G. Towards an optimized crystallization with ultrasound: effect of solvent properties and ultrasonic process parameters. *J. Cryst. Growth* **2008**, *310*, 4177-4184.

(11) McCausland, L.; Cains, P. Ultrasound to make crystals. *Chem. Ind.* **2003**, 15-16.

(12) Ruecroft, G.; Hipkiss, D.; Ly, T.; Maxted, N.; Cains, P. W. Sonocrystallization: the use of ultrasound for improved industrial crystallization. *Org. Process Res. Dev.* **2005**, *9*, 923-932.

(13) Amara, N.; Ratsimba, B.; Wilhelm, A.; Delmas, H. Growth rate of potash alum crystals: comparison of silent and ultrasonic conditions. *Ultrason. Sonochem.* **2004**, *11*, 17-21.

(14) Amara, N.; Ratsimba, B.; Wilhelm, A.-M.; Delmas, H. Crystallization of potash alum: effect of power ultrasound. *Ultrason. Sonochem.* **2001**, *8*, 265-270.

(15) Dalas, E. The effect of ultrasonic field on calcium carbonate scale formation. *J. Cryst. Growth* **2001**, *222*, 287-292.

(16) Dodds, J.; Espitalier, F.; Louisnard, O.; Grossier, R.; David, R.; Hassoun, M.; Baillon, F.; Gatumel, C.; Lyczko, N. The effect of ultrasound on crystallisation-precipitation processes: some examples and a new segregation model. *Part. Part. Syst. Char.* **2007**, *24*, 18-28.

(17) Guo, Z.; Jones, A. G.; Li, N. The effect of ultrasound on the homogeneous nucleation of $BaSO_4$ during reactive crystallization. *Chem. Eng. Sci.* **2006**, *61*, 1617-1626.

(18) Lyczko, N.; Espitalier, F.; Louisnard, O.; Schwartzentruber, J. Effect of ultrasound on the induction time and the metastable zone widths of potassium sulphate. *Chem. Eng. J.* **2002**, *86*, 233-241.

(19) Nishida, I. Precipitation of calcium carbonate by ultrasonic irradiation. *Ultrason. Sonochem.* **2004**, *11*, 423-428.

(20) Thompson, L. H.; Doraiswamy, L. K. The rate enhancing effect of ultrasound by inducing supersaturation in a solid–liquid system. *Chem. Eng. Sci.* **2000**, *55*, 3085-3090.

(21) Virone, C.; Kramer, H. J. M.; Van Rosmalen, G. M.; Stoop, A. H.; Bakker, T. W. Primary nucleation induced by ultrasonic cavitation. *J. Cryst. Growth* **2006**, *294*, 9-15.

(22) Kordylla, A.; Krawczyk, T.; Tumakaka, F.; Schembecker, G. Modeling

ultrasound-induced nucleation during cooling crystallization. *Chem. Eng. Sci.* **2009**, 1635-1642.

(23) Shah, Y. T.; Pandit, A. B.; Moholkar, V. S. *Cavitation Reaction Engineering*, Kluwer Academic / Plenum Publishers: New York, 1999.

(24) Doktycz, S. J.; Suslick, K. S. Interparticle collisions driven by ultrasound. *Science* **1990**, *247*, 1067-1069.

(25) Suslick, K. S. Sonochemistry. *Science* **1990**, *247*, 1439-1445.

(26) Berdonosov, S. S.; Znamenskaya, I. V.; Melikhov, I. V. Mechanism of the vaterite-to-calcite phase transition under sonication. *Inorg. Mater.* **2005**, *41*, 1308-1312.

(27) Kazmierczak, T. F.; Tomson, M. B.; Nancollas, G. H. Crystal growth of calcium carbonate - a controlled composition kinetic study. *J. Phys. Chem.* **1982**, *86*, 103-107.

(28) Tomson, M. B.; Nancollas, G. H. Mineralization kinetics - constant composition approach. *Science* **1978**, *200*, 1059-1060.

(29) Reddy, M. M.; Nancollas, G. H. Crystallization of calcium carbonate. 1. Isotopic exchange and kinetics. *J. Colloid Interface Sci.* **1971**, *36*, 166-172.

(30) Brunauer, S.; Emmett, P. H.; Teller, E. *J. Am. Chem. Soc.* **1938**, *60*, 309.

(31) Lide, D. R. *Handbook of Chemistry and Physics*, Taylor & Francis Group, 2006.

(32) Nyvlt, J.; Matuchova, M. Determination of linear growth rates of crystals (II). The shape factors method. *Krist. Tech.* **1976**, *11*, 245-253.

(33) Matuchova, M.; Nyvlt, J. Determination of linear growth rates of crystals (I). Calculation of linear growth rates of individual crystal faces from overall rates. *Krist. Tech.* **1976**, *11*, 149-161.

(34) Hoch, A. R. Calcite crystal growth inhibition by humic substances with emphasis on hydrophobic acids from the Florida Everglades. *Geochim. Cosmochim. Acta* **2000**, *64*, 61-72.

(35) Mullin, J. W. *Crystallization*, Elsevier Butterworth-Heinemann: Burlington, MA, 2001.

VISUALIZATION OF ACOUSTIC CAVITATION EFFECTS ON SUSPENDED CALCITE CRYSTALS

7

The acoustic cavitation (42,080 Hz, 7.1 W cm^{-2} or 17 W) effects on suspended calcite crystals, sized between 5 and 50 μm, have been visualized for the first time using high speed photography. High speed recordings with a duration of 1 second containing up to 300,000 frames per second, revealed the effect of cluster and streamer cavitation on several calcite crystals. Cavitation clusters, evolved from cavitation inception and collapse, cause attrition, disruption of aggregates and deagglomeration, whereas streamer cavitation causes deagglomeration only. Cavitation on the surface gives the crystals momentum. However, it is shown that breakage of accelerated crystals by interparticle collisions is unrealistic because of their small sizes and low velocities. Crystals that are accelerated by bubble expansion, subsequently experience a deceleration much stronger than expected from drag forces, upon bubble collapse. Experiments with pre-dried crystals seemed to support the current theory on bubble nucleation through the presence of pre-existing gas pockets. However, experiments with fully wetted crystals also showed the nucleation of bubbles on the crystal surface. Although microjet impingement on the crystal surface could not be directly visualized with high speed photography, scanning electron microscopy (SEM) analysis of irradiated calcite seeds showed deep circular indentations. It was suggested that these indentations might be caused by shockwave induced jet impingement. Furthermore, the appearance of voluminous fragments with large planes of fracture indicated that acoustic cavitation can also cause the breakage of single crystal structures.

This chapter has been published as:

Wagterveld, R. M.; Boels, L.; Mayer, M. J.; Witkamp, G. J. Visualization of acoustic cavitation effects on suspended calcite crystals. *Ultrason. Sonochem.* **2011**, *18*, 216-225.

7.1 Introduction

When ultrasound is passed through a liquid it produces pressure waves, which cause negative pressure during the rarefaction stage. This negative pressure can lead to rupture of the fluid and is accompanied by the generation of cavities (i.e., microbubbles). The rupture of fluid and the interaction of acoustic waves with these bubbles is called acoustic cavitation. The varying pressure makes the bubbles oscillate in size. These oscillations are low energetic and this phenomenon is called non-inertial cavitation (or stable cavitation). Above a certain negative pressure threshold, this will lead to inertial cavitation (or transient cavitation), which is the high energetic fast growth and collapse of bubbles (1).

Besides the pressure constraint, inertial cavitation can only occur if the radius of the initial cavity lies between a lower and upper critical value for cavitation. With decreasing frequency of the applied ultrasound, this size range increases which results in more inertial cavitation (2).

In many practical systems the inception of cavitation is observed at much lower tensile stress than calculated using the classical cavitation nucleation theory. The generally accepted theory is that the cavitation inception is mediated by cavities already present in the liquid. The existence of these nucleation sites is usually subscribed to gas pockets in crevices on surfaces and particles. The gas pockets arise by the introduction of water in the container, or by introduction of dry particles into liquid. Some reported experiments, however, cannot be explained by this theory (3). Mørch developed a slightly modified theory based on surface structure (4). In this theory it is assumed that in case of concave surface structures, stress arises at the liquid solid interface. Mørch stated that in this situation, the liquid ruptures at lower tensile stress, without the need of gas pockets.

When ultrasound is passed through a liquid-solid system, bubble cavitation causes a series of unique physical phenomena that can affect the solid. Microjets and high energetic shockwaves are produced by inertial cavitation. Shockwaves are formed when cavities rapidly expand or collapse.

Recently, it has been shown experimentally that spherical particles can be accelerated significantly by the shockwave that occurs during the explosive growth of a cavity on the particle surface (i.e., cavitation inception) (5, 6). During the collapse of a cavity, high local temperatures and pressures arise which result in a pressure shockwave (7-12). Shockwaves may cause mechanical damage to close objects and are known to cause material erosion (1). This phenomenon is used in lithotripsy to fragment kidney stones (13-16). The collapse of bubbles close to a large rigid boundary will be asymmetric and leads to microjet formation in the direction of the surface. Microjets can result in erosion and pitting of the surface (17).

These phenomena make ultrasound a powerful tool to influence many physical and chemical processes. In sonocrystallization, ultrasound is used to help controlling the course of crystallization processes. Sonocrystallization received considerable attention in the last decade. Most of the reported positive effects of ultrasound on crystallization processes are related to the process of crystal nucleation (18). Here, the focus is on the physical effects that ultrasound has on existing crystals.

In this paper a distinction is made between agglomerates and aggregates using the following definitions. An agglomerate is an assemblage of particles which are loosely coherent, and an aggregate is an assemblage of particles rigidly joined together (ISO14887 (19)). Shockwaves can reduce agglomeration.

Ultrasonic treatment of crystals might lead to erosion which can change the crystal habit (20, 21). Recently, the authors reported that ultrasound can increase the volumetric crystal growth rate of calcite significantly (22). It was shown that this effect was related to the alteration of the seed crystals' habit and size. Seed crystals seemed to be subjected to attrition and breakage during ultrasonic irradiation. Although it was suggested that the rupture of agglomerates occurs in close proximity of a collapsing bubble (23), no direct visualization of this phenomenon has been reported yet. One attempt was made by Guo et al. (24), who investigated the acoustic effects on large sugar crystals. It was suggested that both the collisions of crystals and vibration and implosion of cavitation bubbles lead to crystal deagglomeration and breakage. However,

the reported observations were recorded with a frame rate of only 4,500 fps. This is far too low to capture the 20,000 Hz acoustic phenomena (i.e., 4 cavitation cycles per frame) that actually caused the observed breakage and deagglomeration of the sugar crystals.

Several in-situ methods have been used to investigate the effect of cavitation on particles or surfaces, like high speed (HS) imaging (in combination with schlieren/shadow imaging (7-10)) and optical beam deflection (OBD) measurements (9, 11). Furthermore, Scanning Electron Microscopy (SEM) analysis can be used to investigate the resulting particles or surfaces after ultrasonic treatment, to show attrition or breakage of solids, deagglomeration and pitting (25-27). In high speed photography, most of the research involved large surfaces (28-34) and relatively large (metal) particles (5, 6, 24, 35). Also, high speed photography was used to study bubble-bubble interaction (36), cavitation clusters (37, 38) and resonant bubbles (39-43).

The aim of the present work is to identify the cavitation phenomena that are responsible for crystal deagglomeration, disruption of aggregates, attrition and breakage that occurs during seeded calcite sonocrystallization. For this purpose, the physical interaction of acoustic cavitation with suspended calcite crystals was visualized using high speed photography. In addition, SEM analysis was used to investigate the habit of treated crystals.

7.2 Experimental

7.2.1 Materials

Two batches of calcite seed crystals were prepared. The first batch was synthesized, using the method described by Nancollas and Reddy (44), by slowly adding 2 dm^3 of a 0.20 M $CaCl_2$ (VWR, 100 %) solution to 2 dm^3 0.20 M Na_2CO_3 (Boom, > 99.5 %) solution at 25 °C. The second batch was synthesized by adding both solutions simultaneously at 25 °C. The batches were denoted as A and B respectively. The freshly precipitated seed crystal batch A and part of batch B, hereafter B1, were aged overnight in mother liquor and were subsequently washed with Milli-Q water each day for one week. Afterwards,

the washed seed crystals were aged for three weeks before filtering. Seeds A were dried at 105 °C, and seeds B were stored in Milli-Q. The other part of batch B, B2, was also washed with Milli-Q by carefully replacing the mother liquid by Milli-Q water leaving the settled crystals always submerged in liquid. After washing the seeds each day for one week, the seeds were stored in Milli-Q water. The crystals were characterized by Scanning Electron Microscopy (Jeol JSM-6480 LV) and ATR-FTIR spectroscopy (Shimadzu 4800).

7.2.2 Experimental set-up and procedures

In a small square glass box, 0.05 g of calcite seeds were suspended in 100 cm^3 of a saturated $CaCO_3$ solution (1.6 mM $NaHCO_3$ (Boom, 99.5 %), 1.6 mM $CaCl_2$, 95 mM KCl (VWR, 100 %). All experiments were performed at ambient conditions. First, the suspension was allowed to equilibrate with the atmosphere for one day at room temperature. The ultrasonic irradiation period did not exceed 10 seconds in order to minimize the degassing and heating effect of the ultrasound. After the experiments, samples of 15 cm^3 of solution were collected and filtered through a 0.2 μm filter. After drying, the samples were analyzed with SEM.

The interaction of cavitation with the calcite seeds was recorded with a high speed camera (Photron Fastcam SA1.1 model 675K-M1), which can take up to 675,000 frames per second (*fps*). The camera was equipped with a 12 x zoom lens (Navitar). The focal point was adjusted just below the transducer tip. A high powered light source (Karl Storz, Techno Light 270) served as back illumination for the high-speed camera (Figure 1).

The ultrasonic transducer was part of a dedicated homebuilt system that could be controlled precisely in terms of shape, frequency and amplitude of the alternating current for driving the transducer. The transducer was operated at 42,080 Hz. The real output power generated from the transducer was estimated by measuring the adiabatic temperature rise of water irradiated with ultrasound. The input power was determined to be 17 W or 7.1 W cm^{-2}.

Just before the experiment was initiated, settled calcite seeds were mixed by filling a syringe with 50 ml of the saturated solution and injecting it back into

the box. When the calcite suspension was irradiated, a 1 s record was made of the suspension. Afterwards, an image was taken of an object with known size (needle) in order to determine the scale of the images.

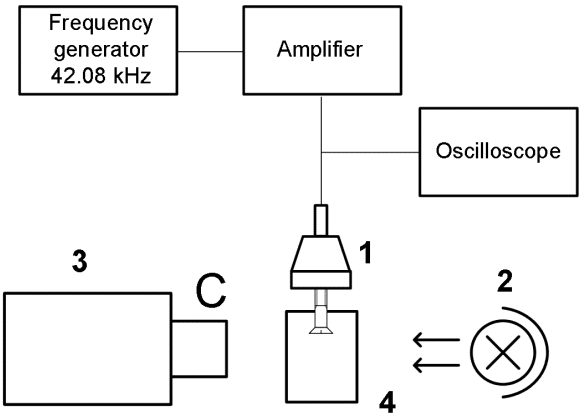

Figure 1. Scheme of the experimental set-up consisting of 1) ultrasonic transducer, 2) high power light, 3) high speed camera with zoom lens, and 4) glass box.

Due to the applied frequency of 42,080 Hz the frame rates were chosen to be at least twice as high, starting with 100,000 fps. At this frame rate, the maximum resolution was 320 × 128 pixels. Increasing the frame rate resulted in a lower image resolution. In order to obtain enough detail of the cavitation effects, a magnifying lens was used. However this reduced the field of view and depth of field. Because the exact location of cavitation interacting with suspended crystals could not be controlled nor predicted, acquiring useful images was rather tedious and required a factor of luck.

The particle velocity, v ($m\ s^{-1}$), and acceleration, a ($m\ s^{-2}$), were determined from the movies. For each frame the centre position of the particle of interest was measured, the displacement from frame to frame was calculated and multiplied by the frame rate, *fps* (s^{-1}), according to:

$$v_{N+0.5} = fps\sqrt{(x_{N+1} - x_N)^2 + (y_{N+1} - y_N)^2} \quad (1)$$

where x (m) is the x-coordinate of the particle of interest and y (m) is the y-coordinate. In a similar fashion the acceleration was determined from the acquired velocities:

$$a_{N+1} = (v_{N+1.5} - v_{N+0.5})\,fps \quad (2)$$

In order to investigate the effect of ultrasound on the crystal habit, 0.5 g seed crystals were added to a 1 dm^3 saturated calcium carbonate solution in a double walled thermostated glass reactor equipped with a floating magnetic stirrer bar to minimize any grinding effects. The seed suspension was stirred at 400 rpm and treated with ultrasound for 45 minutes at 25 °C. After the treatment, samples of 15 cm^3 of solution were collected and filtered through a 0.2 μm filter. After drying, the samples were analyzed with SEM.

7.3 Results and discussion

7.3.1 Seed characterization

The seeds of batch A are the same seeds that were used in the seeded calcite sonocrystallization experiments reported in our previous work (22). These seeds appeared as interpenetrated conglomerates or intergrowths (here after aggregates) made of several small rhombohedral particles (Figure 2A). The seeds of the second batch had a quite different appearance (Figure 2B). In contrary to seeds A, seeds B hardly contained aggregates, but mainly consisted of separate, much larger particles. This proved to be advantageous in the high speed recordings, because of three reasons. First, it is possible to discriminate between deagglomeration and particle breakage/erosion. Secondly, the seeds could be better distinguished from the bubbles, which allowed for better insight in the mechanism of cavity inception and bubble collapse. Thirdly, SEM analysis of larger seeds could reveal more detail on particle erosion. The ATR-

FTIR spectra showed characteristic adsorptions for calcite at 1795, 1392, 871 and 711 cm^{-1} for all batches.

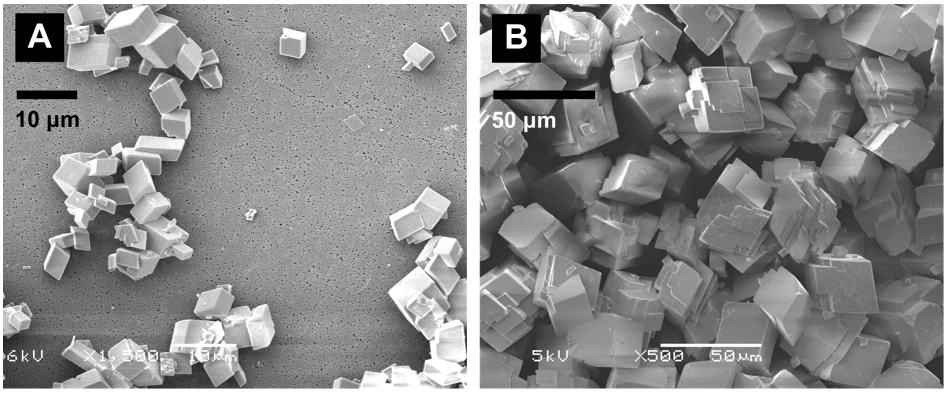

Figure 2. SEM pictures of seed crystals: (A) Seed crystals A (from (22) with permission from Elsevier); (B) seed crystals B.

7.3.2 Bubble structures

It was observed that bubbles can form different structures which are described in literature (37). First, there were streamers, located at the edges of the source and near the surface of the source, accompanied by small clusters (Figure 3A). Secondly, large clusters appeared at some distance away from the source (Figure 3B).

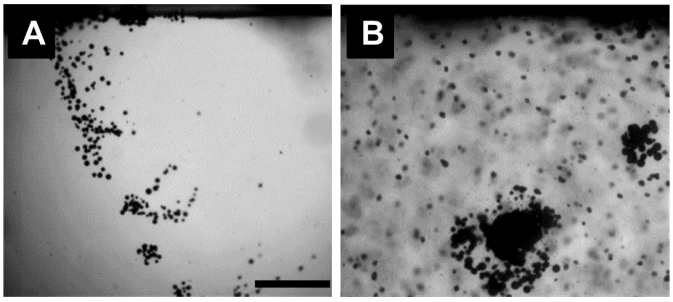

Figure 3. Streamer (A) and large clusters (B). Image A is recorded without seed crystals in the liquid, for better distinction of the bubbles from the seeds. Cluster formation always started on the surface of a particle. Part of the ultrasonic source is visible (dark silhouette) at the top of both images. Scale bar is 500 µm (both images).

Mettin (37) mentions that these clusters probably exhibit large erosion potential but also concluded that there is a lack of experimental data supporting this. In every conducted experiment, it was observed that the formation of a large cluster always starts with the inception of a single cavity on the surface of a particle. Bubbles in streamers did not necessarily start on the surface of seed crystals and the cavitation was also less intense compared to large clusters. Therefore, the influence of cavitation on particles is expected to be much less in case of streamers.

7.3.3 Disruption of aggregates and deagglomeration

In our previous work (22) it was shown that seeds A are easily disrupted upon ultrasonic treatment. The next image series shows the fragmentation of a calcite seed (type A) by a large cluster (Figure 4). In the second frame (t = 8 µs), a trace of a cavity is visible, which is the actual inception of the bubble that evolves into a cluster. The third frame shows the appearance of a small fragment, which indicates that cavitation causes crystal fragmentation. After 32 µs, the imploded cavity splits up, expands again, merges and collapses (t = 40 µs). Now two fragments appear, clearly broken off the crystal. In the next cavitation cycle the first indication of the cluster is visible (last frame) that appears shortly after.

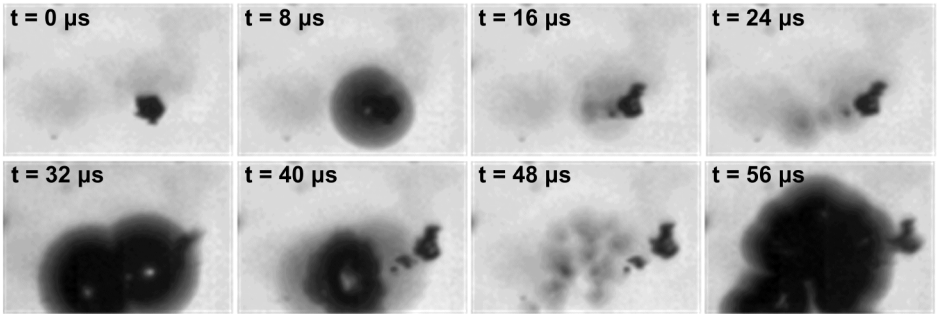

Figure 4. Images of an oscillating cavitation bubble that nucleated on the surface of a type A calcite crystal. The single crystal fragmentizes as a result of the violent collapse of the bubble. Frame rate: 125,000 fps. This movie is available with the online version of the paper.

Occasionally, crystals were caught in the moving cluster and sometimes underwent interparticle collisions. While the velocity of the clusters was approximately 1.5 m s^{-1} (determined by the displacement of the center of the cluster), the velocities of captured crystals inside the cluster ranged from 1.5 to 4.0 m s^{-1}. As soon as the particles were no longer under the influence of cavitation, they lose velocity fast and collisions of these particles were no longer observed.

The crystal shown in Figure 4, was dried before it was submerged in the saturated solution. Probably, small gas cavities already present on the crystal facilitated bubble inception during ultrasonic irradiation. It is interesting to see if this bubble inception also occurs on completely wetted crystals. Several experiments were conducted with crystals B2, and in each experiment much less large cluster formation was encountered (only a few in 1 second of recording) compared to the experiments with initially dry crystals A (hundreds in 1 second of recording). A possible explanation for the inception of clusters on these crystals could be found by the theory developed by Mørch (45) which was proven experimentally (5, 46).

Due to the large size of streamers, they were able to pick up seed crystals from the solution and caused deagglomeration. The mechanism proposed by Kusters (23) has great similarities with the observations shown in Figure 5. A small agglomerate of a seed type B (arrow 1), was picked up by a streamer and moved into the field of view in the first frame. In the second frame (t = 8 μs) a bubble from the streamer expands on the agglomerate causing it to turn. The bubble (arrow 2) collapses between frame 3 and 4 (t = 16 μs & t = 24 μs) and separates the agglomerate in two single crystals. In the following cavitation cycle the bubbles hardly expand. In the subsequent cycle (t = 54 μs) another bubble expands and collapses on the surface of the agglomerate, causing the two parts to move away from each other (arrow 3).

In order to capture the bubble dynamics in more frames, several recordings were made at a frame rate of 300,000 fps. One of these recordings is shown in Figure 6. The images reveal that cavitation does not necessarily have to start on the surface of a particle to cause deagglomeration.

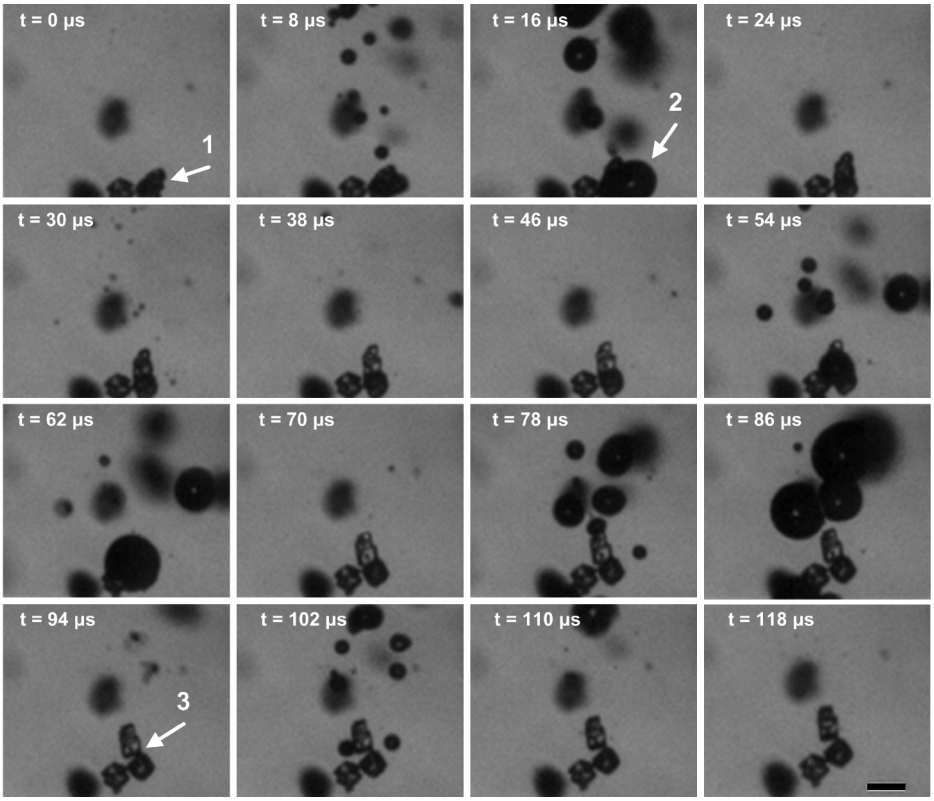

Figure 5. Images of streamer cavitation causing deagglomeration of type B1 calcite crystal (arrow 1). The agglomerate (length: approx. 49 µm) splits up (arrow 3) as a result of the bubble collapse (arrow 2). Frame rate: 125,000 fps; Shutter time: 1 µs, Scale bar is 50 µm. This movie is available with the online version of the paper.

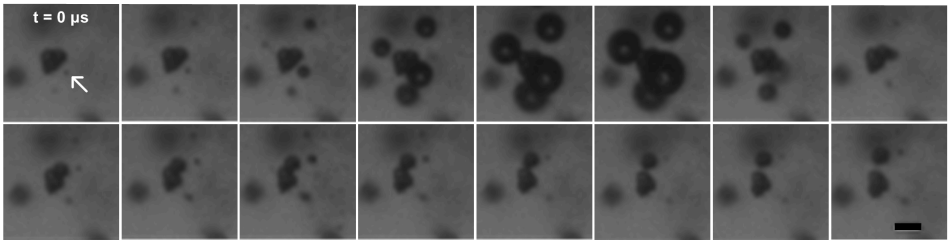

Figure 6. Rupture of type B1 calcite crystal (length: approx. 41 µm), shot at 300,000 fps, scale bar is 53 µm. This movie is available with the online version of the paper.

It is shown that a bubble (arrow in Figure 6) expands close to the surface of a seed B, touches it and collapses in close proximity of the surface. This causes the

particle to separate into two large parts. Although the higher frame rate reveals more of the bubble dynamics, the lower resolution makes it difficult to judge whether the fragments were part of an agglomerate or a single crystal.

7.3.4 Seed acceleration by bubble expansion and collapse

Recently, the acceleration of particles by the inception of cavitation on the surface was reported (5, 6). Figure 7 shows that particle acceleration can also occur by the attachment and detachment of a pre-existing cavitation bubble.

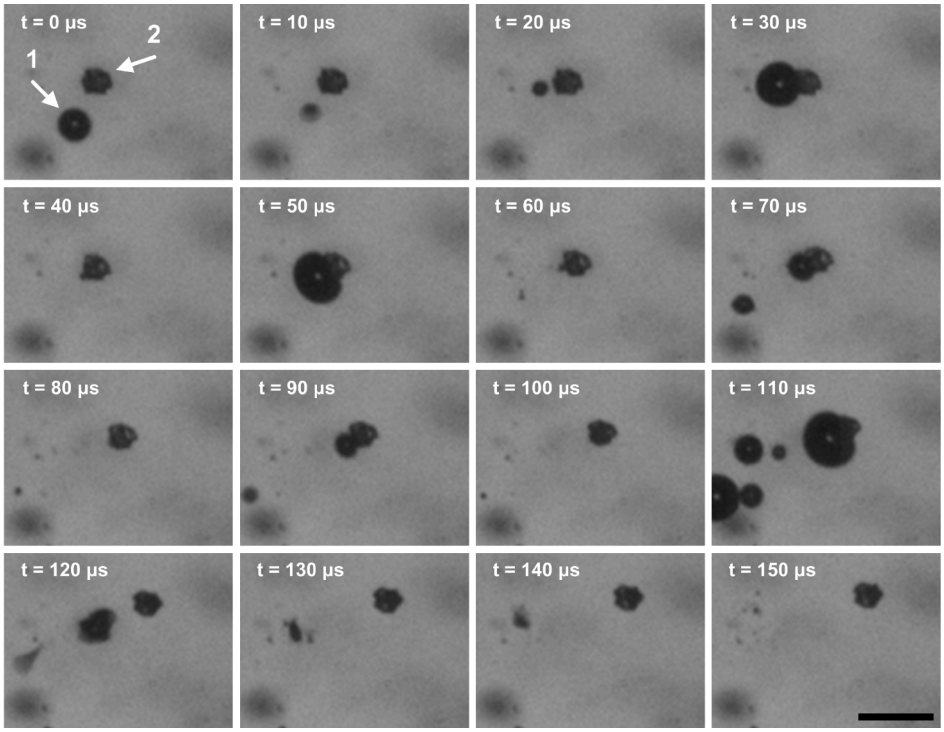

Figure 7. An example of crystal (B1, length: approx. 36 µm, arrow 2) acceleration by bubble (arrow 1) expansion and collapse. Frame rate: 100,000 fps. Scale bar length is 100 µm. The cavitation cycle is 23 µs, which is slightly more than two frames. One frame shows an instant of bubble growth followed by the next frame showing an instant of bubble collapse. This movie is available with the online version of the paper.

In the first frame, a cavitating bubble (arrow 1) approaches a crystal (of type B1, arrow 2). Upon bubble expansion (frames t = 20 µs & t = 30 µs) the bubble wall

pushes the crystal away. The bubble collapses, and remains attached to the surface (frame t = 40 μs). In the next frame, the bubble expands again and the crystal accelerates. After collapse, the bubble splits; part of the bubble moves away from the crystal and another part stays attached to the surface. Both bubbles continue to cavitate, and every expansion of the attached bubble leads to movement of the crystal. After the third expansion (frame t = 110 μs), the bubble completely detaches (frame t = 120 μs) and the crystal obtains its highest average velocity of 1.6 m s^{-1} between these frames, by accelerating with an average of approximately 60,000 m s^{-2}. The particle immediately slows down in the next frame, with an average acceleration of approximately -90,000 m s^{-2}, to an average velocity of 0.7 m s^{-1} (see also Figure 8).

It seems that the strong deceleration is not only caused by drag forces. The drag force on small particles moving through fluids at relatively low speeds, where there is no turbulence, can be described by Stokes's law. From this law, a general equation of motion can be derived, assuming the liquid velocity to be zero (47)

$$v(t) = v_0 e^{-t/\tau} \tag{3}$$

where v_0 ($m\ s^{-1}$) is the initial velocity, t (s) time, and τ (s) the relaxation time. The relaxation time is a constant, defined by material and fluid properties. Using ρ_s ($kg\ m^{-3}$) the density of the solid, η ($Pa\ s$) the liquid viscosity and d (m) the spherical particle diameter gives

$$\tau = \frac{\rho_s d^2}{18\eta} \tag{4}$$

Stokes's law can only be used for Reynolds numbers smaller than 1. At maximum velocity the particle's Reynolds number is 65 and Newton's law has to be applied, resulting in the following relaxation time

$$\tau = \frac{4}{3}\frac{\rho_s d^2}{C_D \eta \mathrm{Re}} \tag{5}$$

$$C_D = \frac{24}{\mathrm{Re}}(1 + 0.15\mathrm{Re}^{0.687}) \tag{6}$$

where Re (-) is Reynolds number and C_D (-) the drag coefficient, described by an empirical relation for 1 < Re < 1000 (Eq. 6). The new relaxation time is no longer constant because Re changes with velocity. However, an outer limit of maximum drag can be defined by assuming Re to be constant at its maximum value. In reality the velocity profile will be between Stokes' law and the outer limit of maximum drag calculated with Newton's law, here defined as the drag window. In Figure 8, the measured velocity profile of the accelerated crystal B1 particle (after frame t = 110 μs) and the profiles calculated according to Stokes and Newton are shown. The initial deceleration from 1.6 to 0.7 m s^{-1} is much faster than calculated and lies far outside the drag window. Therefore this deceleration is not only related to drag, but to an additional external force. Because the crystal is not fixed it may get a superimposed velocity towards the centre of the collapsing bubble within the surrounding liquid (48).

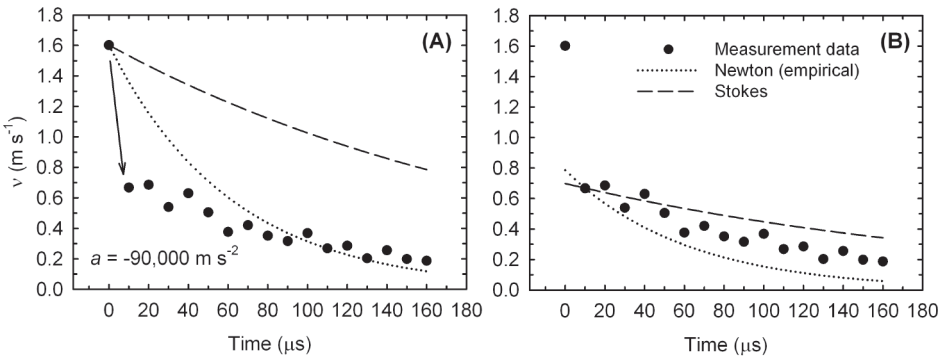

Figure 8. Velocity profile of accelerated crystal B1 from Figure 7. The velocity at t = 0 μs corresponds to the velocity between t = 110 and 120 μs in Figure 7. The arrow indicates the large decrease in velocity right after bubble collapse. The dashed line is calculated with Stokes, the dotted line with Newton (outer limit of maximum drag). Calculation based on the (initial) velocity at, A) t = 0 μs (Re = 65), and B) t = 10 μs (Re = 28).

The detachment of the bubble is probably late in the growth cycle and the particle is prone to the influence of bubble collapse, causing the particle to decelerate fast, which explains the sudden decrease in velocity in Figure 8. After the initial drop in velocity, the profiles can be recalculated (Figure 8B). The experimental values lie inside the drag window, which shows that the gentle decrease in velocity can be subscribed to drag.

7.3.5 Effect of cavitation on crystal habit

In several experiments the appearance of small fragments (i.e., attrition) from single seeds B after a cavitation event could be recorded. Also, many fine fragments can be seen in the SEM images of the treated seeds (Figure 10A), which indicate crystal attrition. On the other hand, several large broken crystal fragments were identified with SEM analysis of seeds B that were irradiated for 45 minutes (Figure 9). These images indicate that 'large breakage' occasionally occurs during ultrasonic irradiation. However, despite our efforts, none of the experiments with seeds B resulted in a recording in which single crystal structures were broken.

Single crystal breakage can only occur, simply stated, if the energy input is higher than the energy required for maximum elastic deformation. Above this barrier, the stress in the crystal is released by plastic deformation and crack growth. In brittle materials, most of the energy goes to crack growth, and the plastic deformation volume is relatively small. During crack growth, material bonds break, and thereby two new surfaces are created. The energy necessary to create a new surface is defined as the fracture surface energy (49). Less energy is required to create small fragments (e.g., breakage of crystal corners, attrition) compared to large fragments (i.e., total crystal breakage). A considerable discrepancy exists between theoretical surface fracture energies, defined by the material bond strength, and experimentally observed surface fracture energies. This is subscribed to Griffith cracks which are small flaws in the material. The number of Griffith cracks increases with increasing particle volume, causing large particles to break more easily than small particles (50).

Particle breakage by collision depends on impact velocity and particle

size. The breakage of gypsum and limestone particles, 100 μm in diameter, was reported to occur at a minimum impact velocity of 13 and 23 m s^{-1}, respectively. Furthermore, when the particle diameter decreases a factor two, the necessary impact velocity is doubled (50). The maximum velocities measured in our experiments are well below these reported values, and the used seeds are also much smaller than 100 μm. In addition, calcite is harder than gypsum (respectively 3 and 2 on Mohs scale (51)) and will be more difficult to break. Although flaws in the crystal structure may cause the crystals to break at reduced impact velocity, it is very unlikely that breakage occurred directly through collision.

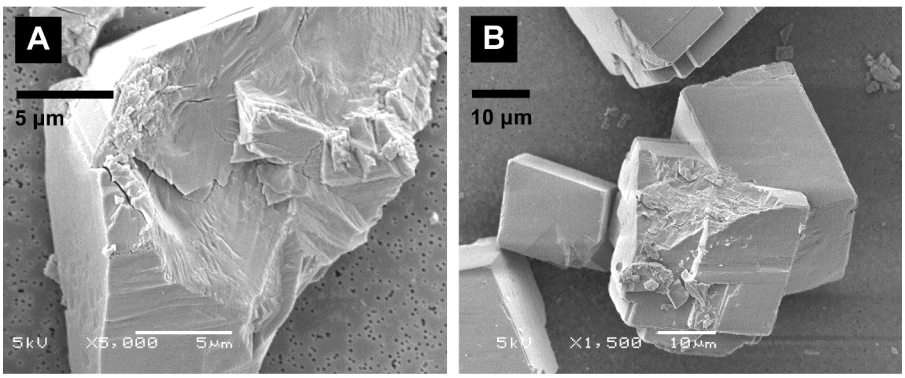

Figure 9. SEM pictures of voluminous fragments of seeds B1 with large planes of fracture.

Two other possible mechanisms can be the cause of crystal breakage; interaction with shockwaves and interaction with microjets (or a combination of both). Shockwaves are produced during inception and at collapse (7-9). If the collapse takes place in the vicinity of a large rigid surface the collapse will be asymmetric leading to microjet formation. When a bubble collapses on a surface, both a microjet and a shockwave are formed simultaneously. According to Shima (8), the mechanism contributing the most to erosion or breakage depends on the shape and the contact angle of the bubble at maximum expansion. Lithotripsy experiments with artificial kidney stones of gypsum showed that the induced shockwave is responsible for total breakage

and that microjets, formed during cavitation, cause pitting (16). The breakage mechanism (brittle breakage) of calcite and kidney stones should be similar. However, the differences in shock intensity and particle size between the reported lithotripsy experiments and the current experiment should not be neglected. In lithotripsy, the shockwave is externally generated and the intensity can be controlled. In the current work (acoustic cavitation), shockwaves were produced by the inception and implosion of cavitating bubbles and the intensity could not be determined. To capture microjet dynamics, very high frame rates are necessary, which consequently results in poor quality recordings with the current experimental equipment.

SEM analysis of treated seeds could provide more information on the breakage mechanisms. The images in Figure 10 and the data that was reported in our previous work (22) suggest that the interaction of calcite seeds with cavitation bubbles results in particle fragmentation. It is reasonable to expect that aggregates break at their weakest points, most likely the points where individual crystals are joined together. Figure 10A and 10B show possible aggregate breakage plains. What is striking in Figure 10B is the circular indentation in the centre of the crystal, which was not subscribed to a growth defect due to its jagged appearance. Also, the morphology of this hole shows a close resemblance with holes produced by laser ablation of calcite (Figure 10C & D, respectively) (52). In the latter case, a circular hole was made by a short, high intensity laser pulse, which removed some material leaving a circular indentation. Although the sizes of the holes are different, the morphology inside the holes is remarkably similar. The appearance of the holes as seen in Figure 10B and C was not very common. Only a handful was noticed on several samples of the treated calcite suspension, containing hundreds of (broken) crystals and larger fragments.

It was shown that high energetic collisions between small calcite particles are unlikely to occur, due to the low particle velocities. Therefore, it is plausible that these holes were caused by one of the inertial cavitation phenomena; shockwave or microjet impingement. Microjet impingement is known to leave behind characteristic microscopic holes in various surfaces (27, 53), resembling

the holes in Figure 10B and C.

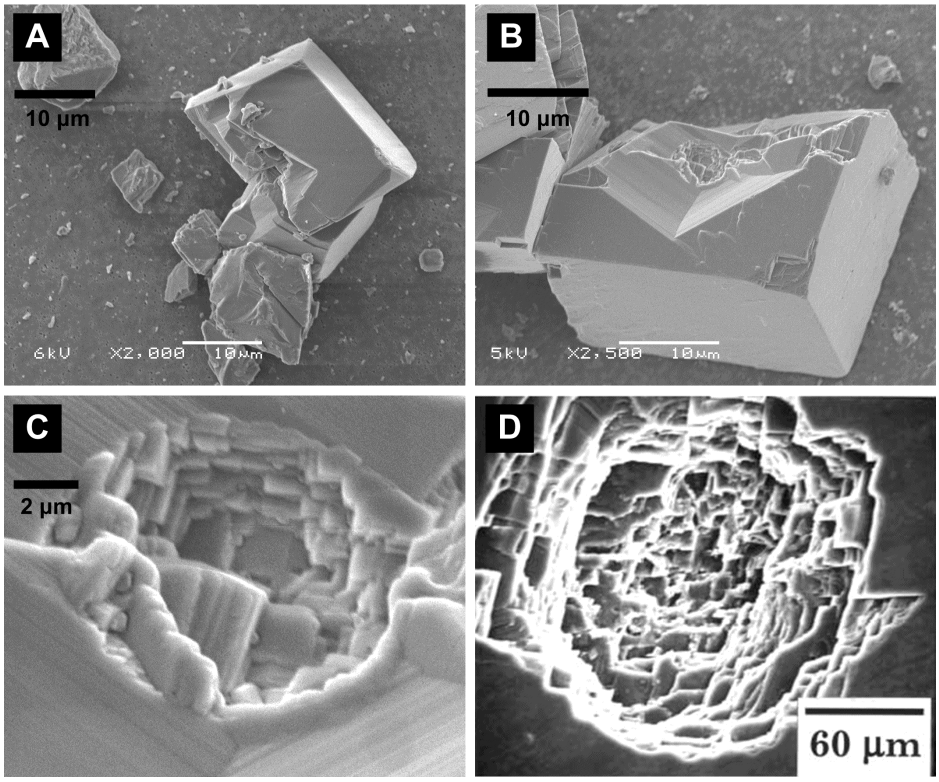

Figure 10. SEM pictures of damaged calcite seeds. Possible broken aggregates (A, B); Circular Indentations caused by ultrasound (B, C) and by laser ablation (D) in calcite (from (52), With kind permission from Springer Science+Business Media).

The majority of these studies, however, comprise jetting on large rigid surfaces. The seed crystals under investigation are smaller than the resonant bubble size, and, therefore, the surface of the crystal cannot induce distortion of bubble collapse leading to jet formation (54). However, it has been shown that jet formation can also occur when cavities collapse under influence of a shock wave (55, 56), irrespective of the presence of a surface (57) (and references therein). Jets produced in this way travel in the direction of the shock. In Figure 11, several jets are shown which were captured at high frame rates (> 250,000 fps).

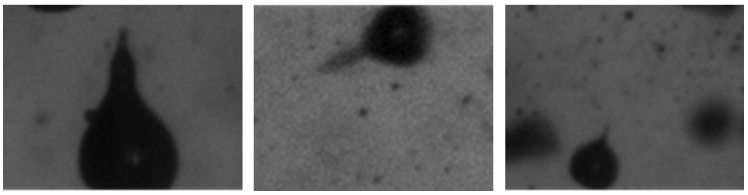

Figure 11. Microjets captured at > 250,000 fps

In each case, no large surfaces or bubbles were present in the direction of the jet. This shows that jets were formed during the ultrasonic irradiation of the crystal suspensions, probably due to shockwaves that originated from other collapsing bubbles nearby. Based on this, it is reasonable to suggest that shockwave induced jetting can also occur from collapsing bubbles attached to small crystal surfaces. If the direction of the shock is towards the surface, the jet impinges on the crystal surface, which might result in the characteristic holes shown in Figure 10. However, despite our efforts, a record of jet impingement on a suspended crystal could not be obtained. Therefore, no direct proof for jetting on the crystals can be presented in the current work, and further research on this topic is required.

7.4 Conclusions

The cavitation phenomena that cause suspended calcite crystals to deagglomerate, disaggregate and accelerate were successfully visualized with high speed photography. Cavitation clusters, evolved from cavitation inception and collapse, caused attrition, disruption of aggregates and deagglomeration. Streamer cavitation was observed to cause deagglomeration and did not show crystal fragmentation potential. Seeds can be accelerated by cavitation on the surface. However, high energetic interparticle collisions between accelerated particles were not observed due to their limited velocity and size. Crystals that were accelerated by bubble expansion, subsequently experienced a deceleration much stronger than expected from drag forces, upon bubble collapse.

Experiments with pre-dried crystals supported the theory of bubble nucleation

through pre-existing gas pockets, however, experiments with fully wetted crystals also showed bubble nucleation on the crystal surface. The appearance of voluminous fragments with large planes of fracture, as shown by SEM, indicated that acoustic cavitation can cause the breakage of single crystal structures. Also, deep circular indentations were discovered.

Although microjet impingement on the crystal surface could not be directly visualized, it is suggested that these indentations might be caused by shockwave induced jet impingement.

7.5 Acknowledgements

This work was performed in the TTIW-cooperation framework of Wetsus, Centre of Excellence for Sustainable Water Technology (www.wetsus.nl). Wetsus is funded by the Dutch Ministry of Economic Affairs, the European Union Regional Development Fund, the Province of Fryslân, the City of Leeuwarden and the EZ/Kompas program of "Samenwerkingsverband Noord-Nederland". The authors like to thank the participants of the research theme "Sensoring" and theme "Concentrates" for the discussions and their financial support.

7.6 References

(1) Leighton, T. G. What is ultrasound? *Prog. biophys. Mol. Bio.* **2007**, *93*, 3-83.

(2) Holland, C. K.; Apfel, R. E. An improved theory for the prediction of microcavitation thresholds. *IEEE T. Ultrason. Ferr.* **1989**, *36*, 204-208.

(3) Caupin, F.; Herbert, E. Cavitation in water: a review. *C. R. Phys.* **2006**, *7*, 1000-1017.

(4) Mørch, K. A. Reflections on cavitation nuclei in water. *Phys. Fluids* **2007**, *19*, 072104-072107.

(5) Arora, M.; Ohl, C. D.; Mørch, K. A. Cavitation inception on microparticles: A self-propelled particle accelerator. *Phys. Rev. Lett.* **2004**, *92*, 174501-174504.

(6) Borkent, B. M.; Arora, M.; Ohl, C. D.; De Jong, N.; Versluis, M.; Lohse, D.; Mørch, K. A.; Klaseboer, E.; Khoo, B. C. The acceleration of solid particles subjected to cavitation nucleation. *J. Fluid Mech.* **2008**, *610*, 157-182.

(7) Philipp, A.; Lauterborn, W. Cavitation erosion by single laser-produced bubbles. *J. Fluid Mech.* **1998**, *361*, 75-116.

(8) Shima, A. Studies on bubble dynamics. *Shock Waves* **1997**, *7*, 33-42.

(9) Petkovsek, R.; Gregorcic, P. A laser probe measurement of cavitation bubble dynamics improved by shock wave detection and compared to shadow photography. *J. Appl. Phys.* **2007**, *102*, 044909.

(10) Brujan, E. A.; Ikeda, T.; Matsumoto, Y. On the pressure of cavitation bubbles. *Exp. Therm. Fluid Sci.* **2008**, *32*, 1188-1191.

(11) Xu, R.; Zhao, R.; Cui, Y.; Lu, J.; Ni, X. The collapse and rebound of gas–vapor cavity on metal surface. *Optik* **2009**, *120*, 115-120.

(12) Lindau, O.; Lauterborn, W. Cinematographic observation of the collapse and rebound of a laser-produced cavitation bubble near a wall. *J. Fluid Mech.* **2003**, *479*, 327-348.

(13) Lokhandwalla, M.; Sturtevant, B. Fracture mechanics model of stone comminution in ESWL and implications for tissue damage. *Phys. Med. Biol.* **2000**, *45*, 1923-1940.

(14) Eisenmenger, W. The mechanisms of stone fragmentation in ESWL. *Ultrasound Med. Biol.* **2001**, *27*, 683-693.

(15) Pishchalnikov, Y. A.; Sapozhnikov, O. A.; Bailey, M. R.; Williams Jr, J. C.; Cleveland, R. O.; Colonius, T.; Crum, L. A.; Evan, A. P.; McAteer, J. A. Cavitation bubble cluster activity in the breakage of kidney stones by lithotripter shockwaves. *J Endourol.* **2003**, *17*, 435-446.

(16) Sapozhnikov, O. A.; Maxwell, A. D.; MacConaghy, B.; Bailey, M. R. A mechanistic analysis of stone fracture in lithotripsy. *J. Acoust. Soc. Am.* **2007**, *121*, 1190-1202.

(17) Franc, J. P.; Michel, J. M. *Fundamentals of Cavitation*, Kluwer Academic: New York, 2004.

(18) Luque de Castro, M. D.; Priego-Capote, F. Ultrasound-assisted crystallization (sonocrystallization). *Ultrason. Sonochem.* **2007**, *14*, 717-724.

(19) Nichols, G.; Byard, S.; Bloxham, M. J.; Botterill, J.; Dawson, N. J.; Dennis, A.; Diart, V.; North, N. C.; Sherwood, J. D. A review of the terms agglomerate and aggregate with a recommendation for nomenclature used in powder and particle characterization. *J. Pharm. Sci.* **2002**, *91*, 2103-2109.

(20) Amara, N.; Ratsimba, B.; Wilhelm, A. M.; Delmas, H. Crystallization of potash alum: effect of power ultrasound. *Ultrason. Sonochem.* **2001**, *8*, 265-270.

(21) Guo, Z.; Zhang, M.; Li, H.; Wang, J.; Kougoulos, E. Effect of ultrasound on anti-solvent crystallization process. *J. Cryst. Growth* **2005**, *273*, 555-563.

(22) Boels, L.; Wagterveld, R. M.; Mayer, M. J.; Witkamp, G. J. Seeded calcite sonocrystallization. *J. Cryst. Growth* **2010**, *312*, 961-966.

(23) Kusters, K. A.; Prastinis, S. E.; Thoma, S. G.; Smith, D. M. Ultrasonic fragmentation of agglomerate powders. *Chem. Eng. Sci.* **1993**, *48*, 4119-4127.

(24) Guo, Z.; Jones, A. G.; Li, N.; Germana, S. High-speed observation of the effects of ultrasound on liquid mixing and agglomerated crystal breakage processes. *Powder Technol.* **2007**, *171*, 146-153.

(25) Jeevanandam, P.; Diamant, Y.; Motiei, M.; Gedanken, A. The effect of ultrasound irradiation on polycrystalline MoO_3. *Phys. Chem. Chem. Phys.* **2001**, *3*, 4107-4112.

(26) Markovic, S.; Mitric, M.; Starcevic, G.; Uskokovic, D. Ultrasonic de-agglomeration of barium titanate powder. *Ultrason. Sonochem.* **2008**, *15*, 16-20.

(27) Haosheng, C.; Jiadao, W.; Darong, C. Cavitation damages on solid surfaces in suspensions containing spherical and irregular microparticles. *Wear* **2009**, *266*, 345-348.

(28) Marmottant, P.; Versluis, M.; de Jong, N.; Hilgenfeldt, S.; Lohse, D. High-speed imaging of an ultrasound-driven bubble in contact with a wall:"Narcissus" effect and resolved acoustic streaming. *Exp. Fluids* **2006**, *41*, 147-153.

(29) Bai, L.; Xu, W.; Tian, Z.; Li, N. A high-speed photographic study of ultrasonic cavitation near rigid boundary. *J. Hydrodyn.* **2008**, *20*, 637-644.

(30) Bremond, N.; Arora, M.; Dammer, S. M.; Lohse, D. Interaction of cavitation bubbles on a wall. *Phys. Fluids* **2006**, *18*, 121505-121501-121505-121510.

(31) Prentice, P.; Cuschieri, A.; Dholakia, K.; Prausnitz, M.; Campbell, P. Membrane disruption by optically controlled microbubble cavitation. *Nat. Phys.* **2005**, *1*, 107-110.

(32) Tomita, Y.; Robinson, P. B.; Tong, R. P.; Blake, J. R. Growth and collapse of cavitation bubbles near a curved rigid boundary. *J. Fluid Mech.* **2002**, *466*, 259-283.

(33) Kodama, T.; Tomita, Y. Cavitation bubble behavior and bubble-shock wave interaction near a gelatin surface as a study of in vivo bubble dynamics. *Appl. Phys. B - Lasers O.* **2000**, *70*, 139-149.

(34) Blake, J. R.; Robinson, P. B.; Shima, A.; Tomita, Y. Interaction of two cavitation bubbles with a rigid boundary. *J. Fluid Mech.* **1993**, *255*, 707-707.

(35) Soh, W. K.; Willis, B. A flow visualization study on the movements of solid particles propelled by a collapsing cavitation bubble. *Exp. Therm. Fluid Sci.* **2003**, *27*, 537-544.

(36) Yasui, K.; Iida, Y.; Tuziuti, T.; Kozuka, T.; Towata, A. Strongly interacting bubbles under an ultrasonic horn. *Phys. Rev. E* **2008**, *77*, 16609.

(37) Mettin, R. Bubble structures in acoustic cavitation. *Bubble and Particle Dynamics in Acoustic Fields: Modern Trends and Applications, Research Signpost, Kerala (India)* **2005**, 1-36.

(38) Takashi, K.; Kuwabara, M.; Jian, Y. Visualization of acoustically induced cavitation bubbles and microjets with the aid of a high-speed camera. *Jpn. J. Appl. Phys.* **2005**, *44*, 4647-4652.

(39) Koyama, D.; Barbier, N.; Watanabe, Y. Shell effects on vibration behavior of a microcapsule in an acoustic field. *Jpn. J. Appl. Phys* **2003**, *42*, 6700-6704.

(40) Ohl, C. D. Cavitation inception following shock wave passage. *Phys. Fluids* **2002**, *14*, 3512-3521.

(41) Lauterborn, W.; Hentschel, W. Cavitation bubble dynamics studied by high speed photography and holography, pt. 1. *Ultrasonics* **1985**, *23*, 260-268.

(42) Lauterborn, W.; Hentschel, W. Cavitation bubble dynamics studied by high speed photography and holography: part two. *Ultrasonics* **1986**, *24*, 59-65.

(43) Olson, H. G.; Hammitt, F. G. High-speed photographic studies of ultrasonically induced cavitation. *J. Acoust. Soc. Am* **1969**, *46*, 1272-1283.

(44) Reddy, M. M.; Nancollas, G. H. The crystallization of calcium carbonate: I. Isotopic exchange and kinetics. *J. Colloid Interface Sci.* **1971**, *36*, 166-172.

(45) Mørch, K. A. Cavitation nuclei and bubble formation: A dynamic liquid-solid interface problem. *J. Fluids Eng.* **2000**, *122*, 494-498.

(46) Marschall, H. B.; Mørch, K. A.; Keller, A. P.; Kjeldsen, M. Cavitation inception by almost spherical solid particles in water. *Phys. Fluids* **2003**, *15*, 545-553.

(47) Hinds, W. C. *Aerosol Technology: Properties, Behavior, and Measurement of Airborne Particles*, Wiley-Interscience: New York, 1998.

(48) Chahine, G. L. Experimental and asymptotic study of nonspherical bubble collapse. *Appl. Sci. Res.* **1982**, *38*, 187-197.

(49) Roylance, D. *Introduction to Fracture Mechanics*, Massachusetts Institute of Technology: Cambridge, 2001.

(50) Yashima, S.; Kanda, Y.; Sano, S. Relationships between particle size and fracture energy or impact velocity required to fracture as estimated from single particle crushing. *Powder Technol.* **1987**, *51*, 277-282.

(51) Broz, M. E.; Cook, R. F.; Whitney, D. L. Microhardness, toughness, and modulus of Mohs scale minerals. *Am. Mineral.* **2006**, *91*, 135-142.

(52) Park, H. K.; Haglund Jr, R. F. Laser ablation and desorption from calcite from ultraviolet to mid-infrared wavelengths. *Appl. Phys. A - Mater.* **1997**, *64*, 431-438.

(53) Karimi, A.; Avellan, F. Comparison of erosion mechanisms in different types of

cavitation. *Wear* **1986**, *113*, 305-322.

(54) Suslick, K. S. Sonochemistry. *Science* **1990**, *247*, 1439-1445.

(55) Chaudhri, M. M.; Field, J. E. Role of rapidly compressed gas pockets in initiation of condensed explosives. *P. Roy. Soc. Lond. A Mat.* **1974**, *340*, 113-128.

(56) Dear, J. P.; Field, J. E.; Walton, A. J. Gas-compression and jet formation in cavities collapsed by a shock-wave. *Nature* **1988**, *332*, 505-508.

(57) Tomita, Y. in *Shock Wave Science and Technology Reference Library*. Van Dongen, M.E.H. (ed), Springer: Heidelberg, 2007, 35-66.

ULTRASONIC REACTIVATION OF PHOSPHONATE POISONED CALCITE DURING CRYSTAL GROWTH

8

The effect of ultrasonic irradiation (42,150 Hz, 17 W dm^{-3} / 7.1 W cm^{-2}) on the growth of calcite in the presence of the inhibitor nitrilotris(methylenephosphonic acid) (NTMP) was investigated at constant composition conditions. In seeded growth experiments, it was found that the inhibiting effect of NTMP on crystal growth could be seriously mitigated under influence of ultrasonic irradiation. An approximately twofold increase in volumetric growth rate was achieved during ultrasonic irradiation, and recovery of the growth rate following inhibition was strongly enhanced compared to growth experiments without ultrasonic irradiation. The results could be explained in part by the physical effect of ultrasound that causes breakage and attrition of poisoned crystals, which resulted in an increase in fresh surface area. Mass spectroscopy analysis of sonicated NTMP solutions revealed that there is also a chemical effect of ultrasound that plays an important role. Several breakdown products were identified, which showed that ultrasound caused the progressive loss of phosphonate groups from NTMP, probably by means of physicochemically generated free radicals and/or pyrolysis in the hot bubble-bulk interface.

This chapter has been published as:

Boels, L.; Wagterveld, R. M.; Witkamp, G. J. Ultrasonic reactivation of phosphonate poisoned calcite during crystal growth. *Ultrason. Sonochem.* **2011**, *18*, 1225-1231.

8.1 Introduction

The presence of sparingly soluble inorganic compounds that tend to form scale layers on surfaces of, for example, membranes and heat exchange equipment, like calcium carbonate, imposes limitations to the efficiency of many industrial water treatment processes. With the aid of growth inhibitors (or antiscalants), primarily comprising polyelectrolytes such as phosphonates or polycarboxylates, the precipitation (scaling) of these inorganic compounds from aqueous solutions can be prevented or retarded at far substoichiometric inhibitor concentrations. One example of a phosphonate growth inhibitor is nitrilotris(methylenephosphonic acid) (NTMP), which is widely used in many technical applications for scale and corrosion inhibition (1-7).

Unfortunately, the presence of growth inhibitors also hinders the desirable downstream removal of scaling salts from waste brines (8-11). Therefore, these inhibitors should be removed (11, 12) or degraded (13) in order to facilitate scaling salt removal. Recently, ozonation has been applied (13) to degrade growth inhibitors in reverse osmosis concentrates followed by the unseeded precipitation of calcium carbonate through sodium bicarbonate dosing.

Removal of calcium carbonate by means of seeded crystallization offers several technical and economical benefits compared to the unseeded precipitation technique. In the first place, because a preferential surface area for heterogeneous nucleation and growth is provided, which can significantly improve crystallization kinetics (9, 10, 14). In the second place, because selection of seeds with a suitable size can significantly improve the solid-liquid separation efficiency. The reactivity of the seed crystals, the degree of supersaturation and the solution composition dictate the growth rate and hence, the calcium carbonate removal efficiency. The presence of growth inhibitors like NTMP can markedly decrease the reactivity of seed crystals by blocking the active growth sites through adsorption of these compounds onto the crystal surface (2, 3, 6, 15). The question is whether or not ultrasound can be used to improve the reactivity of poisoned seed crystals during growth.

The unique physical phenomena that occur when ultrasound is passed

through a liquid-solid system might help reactivate poisoned seed crystals in two ways. First, there is the physical effect of ultrasound, which can enhance the reactivity of the crystals by enlarging the surface area. Previous research on seeded calcite crystallization has demonstrated that the volumetric growth rate of calcite can be enhanced significantly by the action of inertial cavitation (16). High speed recordings revealed the mechanism of deagglomeration, attrition and crystal breakage by acoustic cavitation (17). Among others, potash alum (18), sugar (19), roxithromycin (20) and potassium dihydrogen phosphate (21) crystals were reported to erode upon ultrasonic treatment as well. Second, there is the chemical effect of ultrasound that might cause degradation of the growth inhibitor. It is well known that inertial cavitation in water leads to the formation of highly reactive species including hydroxyl (·OH), hydrogen (·H) and hydroperoxyl ($\cdot HO_2$) radicals, and hydrogen peroxide (22, 23). The most important of which are the hydroxyl radicals. This is due to the very short-lived extreme conditions that occur during bubble collapse. It has been stated that, locally, the temperature and pressure may reach up to 5000 K and 1000 atm, respectively (24-26). In general, this so called 'hot-spot' theory has been adopted in most sonochemical studies to explain experimental results. According to this theory, the harsh conditions inside a collapsing bubble provide the activation energy required for homolytic bond cleavage of solvent and substrate molecules that diffused into the bubble. The radicals generated in this way either react with each other or diffuse into the bulk liquid to serve as oxidants. In the hot interfacial zones of cavitation bubbles, which have been estimated to heat up to approximately 2000 K (26) during bubble collapse, both pyrolysis and free-radical reactions can occur.

Ultrasound has been extensively investigated as an advanced oxidation process for degrading various pollutants including aromatic compounds, chlorinated aliphatic hydrocarbons, explosives, herbicides and pesticides, organic dyes, organic and inorganic gaseous pollutants, organic sulfur compounds, oxygenates and alcohols, pharmaceuticals, personal care products, pathogens and bacteria in water (27). Sonochemical oxidation works best for volatile hydrophobic compounds, which can diffuse and degrade inside the

collapsing bubble. Only few reports deal with non-volatile hydrophilic compounds, including natural organic matter in groundwater (28) and humic acids (29). No reports are available on the sonochemical degradation of phosphonates.

In the present work, the effect of ultrasound on the growth of calcite in the presence of nitrilotris(methylenephosphonic acid) (NTMP) was investigated. The aim was to improve in situ the reactivity of poisoned calcite seed crystals by using ultrasound. The calcite crystal growth was measured using the constant composition method (30) at various NTMP concentrations with and without ultrasonic irradiation at low supersaturation. With this method, any change in reactivity of the calcite crystals by ultrasonic irradiation can be measured directly.

8.2 Experimental

8.2.1 Chemicals

All solutions were prepared using high quality water (MilliQ Reagent Water System, resistivity >18 MΩ cm) saturated in air. Sodium bicarbonate ($NaHCO_3$), calcium chloride ($CaCl_2.2H_2O$) and potassium chloride (KCl) were of analytical grade and were obtained from Boom (Meppel, The Netherlands).

Nitrilotris(methylenephosphonic acid) (NTMP) was obtained from Fluka in its acid form with a purity of > 97 %. From this, a stock solution with a concentration of 1.00 g dm^{-3} (3.34 mM) and neutral pH (after KOH addition) was prepared and stored without exposure to light at 277 K.

8.2.2 Calcite seed crystals

The preparation of the calcite seed crystals has been described previously (16). The dry crystals were characterized by scanning electron microscopy (Jeol JSM-6480 LV), ATR-FT-IR spectroscopy (Shimadzu 4800) and nitrogen adsorption (Micromeritics Tristar 3000). The specific surface area of the seed crystals was found to be 0.17 ± 0.04 m^2 g^{-1} as determined with a five-point BET method (31) on 3 replicate samples. The ATR-FT-IR spectra confirmed that the

crystals were pure calcite with characteristic adsorptions at 1795, 1392, 871, and 711 cm^{-1}. The crystals appeared as interpenetrated conglomerates with a size of around 10 μm (Figure 1).

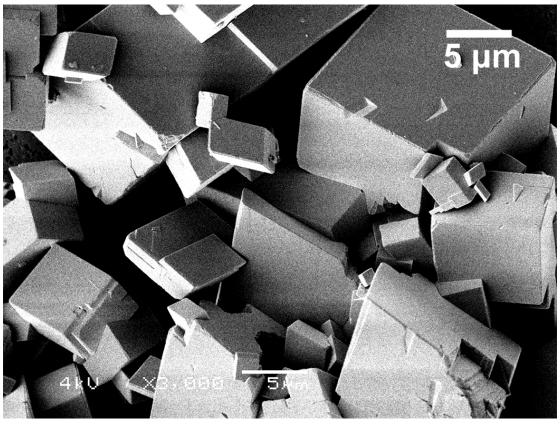

Figure 1. Scanning electron microscopy picture of the employed calcite seed crystals. The crystals appeared as interpenetrated conglomerates with a size of around 10 μm.

8.2.3 Experimental set-up

A scheme of the constant composition experimental set-up used to measure the volumetric crystal growth rate of calcite during ultrasonic irradiation is shown in Figure 2. A double walled glass reactor was used, equipped with a floating magnetic stirrer (Nalgene) to minimize grinding of the seed crystals, a by-pass loop and an ultrasonic transducer. For the control of pH, a combined Pt-ring pH electrode and a shielded Ag/AgCl reference electrode (Syntrode, Metrohm) in combination with two coupled automatic burettes (Metrohm Titrino 785 and Dosimat 665) were used. In order to avoid damaging or influencing the electrodes by the ultrasonic irradiation, both electrodes and a temperature sensor were positioned in a glass cell in the by-pass stream. The ultrasonic transducer was part of a dedicated homebuilt system that could be controlled precisely in terms of shape, frequency and amplitude of the alternating current for driving the transducer. The transducer was operated at 42,150 Hz. The actual value of the ultrasound power delivered to the medium by the stainless

steel horn was determined by measuring the adiabatic temperature rise of water irradiated with ultrasound. For this purpose a similar well isolated glass reactor filled with 1 kg water was used. The input power was determined to be 17 W or 7.1 W cm^{-2}.

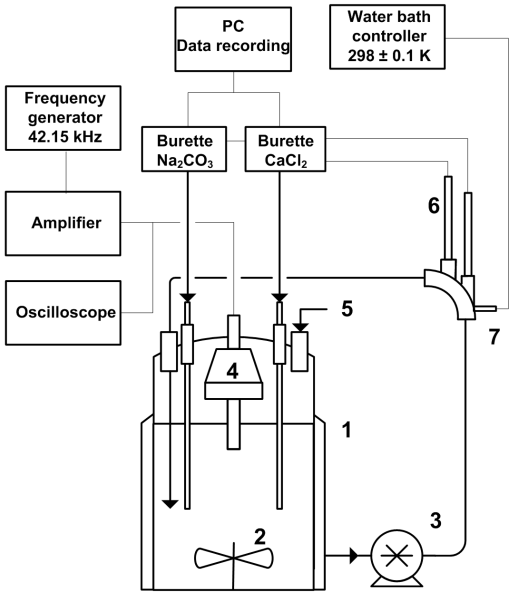

Figure 2. Scheme of the constant-composition experimental set-up consisting of 1) a double walled glass reactor, 2) a floating magnetic stirrer bar, 3) a pump, 4) an ultrasonic transducer, 5) a free port for seed addition, 6) a pH electrode and reference electrode and 7) a temperature sensor.

8.2.4 Experimental procedures

Metastable working solutions were prepared by slow addition of 500 cm^3 of a 4 mM $CaCl_2$ solution to a stirred 500 cm^3 of a 4 mM $NaHCO_3$ solution in the reactor. Before addition of the calcium solution, an aliquot of the NTMP standard solution was injected to the carbonate solution to obtain the desired NTMP concentration in the range of 0.01 – 0.05 mg dm^{-3}. The working solution was stirred at 400 rpm. The solution pH was adjusted to the desired value of

8.650 ± 0.002 using a 0.05 M KOH solution. The stability of the working solution was verified by observing a constant pH for at least 45 min.

Experiments were started by the addition of 0.250 ± 0.002 g seed crystals as a slurry: the dry seed crystals were weighed into a syringe and a small amount of working solution was drawn up into the syringe, and then the content was injected back into the growth solution with several rinses. After the addition of the seed crystals, the solution pH started to decrease as a result of calcite growth. This triggered the automatic burettes to add concurrently equivalent amounts of calcium chloride and sodium carbonate solutions in order to achieve and maintain the pH at 8.650 ± 0.002. In this way, a constant degree of supersaturation was maintained throughout the growth experiment. Fresh titrant solutions were prepared every day with a sevenfold higher calcium and carbonate concentration compared to the working solution. Potassium chloride was added to all solutions to maintain the ionic strength constant at 0.1 M.

Constant ultrasonic irradiation was initiated after 15 min of normal growth and lasted for 45 min. After that, the seeds were allowed to grow further until 25 cm^3 of titrant was consumed. In this way, dilution of the NTMP inhibitor by the addition of NTMP free titrant was kept to a minimum (< 5 %). Depending on the employed inhibitor concentration, total growth times ranged from 2 to 15 h. Also, experiments were conducted in which several fresh doses of NTMP (0.03 mg dm^{-3}) were added to the same growth solution. Ultrasonic irradiation was initiated 15 minutes after each fresh NTMP dose.

The temperature was maintained constant at 298 ± 0.1 K by circulating water from a thermobath through the jacket of the reactor. During the ultrasonic irradiation, the thermobath was set to cool in order to keep the reaction mixture temperature at 298 ± 0.1 K. During the experiment, aliquots of solution were rapidly removed through a septum, filtered by a 0.2 μm filter and analyzed for the calcium content with inductive-coupled plasma spectrometry (Optima 3000XL, Perkin-Elmer) to verify the constancy of the degree of supersaturation.

All experiments were conducted at atmospheric pressure with ambient

levels of CO_2. By keeping the reactor lid closed and all ports sealed during the experiments, the exchange of CO_2 between the atmosphere and the reactor solution was minimized. Ultrasonic irradiation of metastable working solutions without the addition of seed crystals did not result in a change in pH compared to the control. This indicates that any degassing effects were negligible in the sealed reactor. Also, no spontaneous $CaCO_3$ precipitation was observed within 24 h.

In order to investigate whether or not the employed ultrasonic irradiation was able to affect the NTMP molecules chemically, control experiments were carried out by irradiating a fresh 5.0 mg dm^{-3} NTMP solution in pure water at neutral pH. Duplicate samples were injected immediately after the experiment into a triple-quad mass spectrometer (Agilent 6410).

8.3 Results and Discussion

8.3.1 $CaCO_3$ supersaturation and growth mechanism

For $CaCO_3$, the supersaturation ratio, S, is best expressed in terms of activities:

$$S = (IAP / K_{sp})^{1/\upsilon} \quad (1)$$

where IAP is the ion activity product, K_{sp} is the thermodynamic solubility product, and υ is the number of ions in the formula unit (32). The supersaturation ratio, S, with respect to calcite of the working solution used here was calculated to be 2.48 (software: Visual Minteq v2.53, model: Davies). At this relatively low supersaturation ratio, a metastable solution can be obtained in which precipitation is thermodynamically possible, but spontaneous precipitation is improbable due to slow kinetics. The metastable solutions used in this study, showed a constant pH for at least 24 h, indicating that no spontaneous $CaCO_3$ precipitation occurred.

Preliminary growth experiments at different supersaturation ratios

(2.11 > S < 2.91) revealed a second-order dependence of growth rate on the supersaturation ratio, indicating a spiral growth mechanism (32).

8.3.2 Seeded calcite growth experiments

The inhibiting effect of NTMP on the crystal growth of calcite can be described in terms of the values of reduced (or inhibited) growth rates and the length of the inhibition period caused by the addition of NTMP to the growth solution. This is illustrated in Figure 3 where the amount of added Ca^{2+} (n) versus time (t) curves and the first and second derivative plots of these curves for one ultrasound and two control experiments are shown.

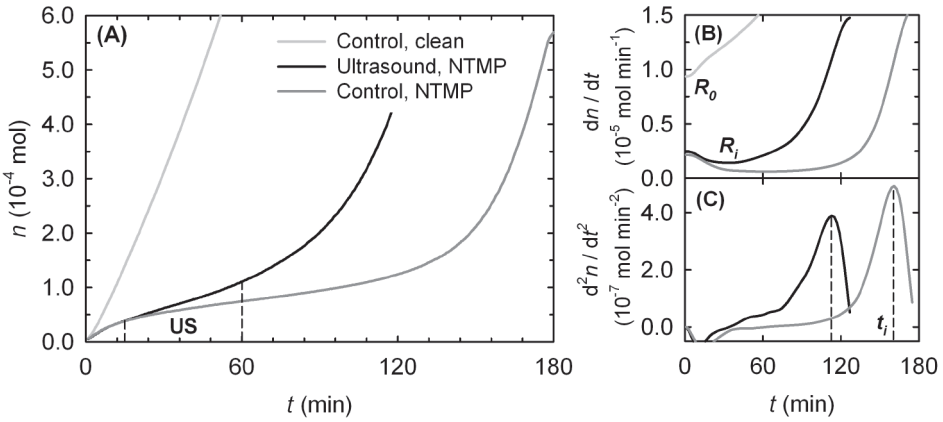

Figure 3. Effect of ultrasonic irradiation on the inhibition of calcite growth by NTMP (0.03 mg dm^{-3}): (A) moles of added Ca^{2+} (n) versus time curves of an ultrasound experiment and two control experiments; (B) derivative plots of the same experiments. The inhibited growth rate R_i and normal growth rate R_0 regions are shown; (C) Second derivative plots used for determining the inhibition period t_i. A smoothing spline method was applied for the curves in graphs B and C.

Without the presence of NTMP, an almost linear curve was obtained (Figure 3A). The slope of this titrant addition versus time curve increases over time. Growth leads to an increase of crystal volume and surface and the volumetric growth rate increases with the size of the growth spirals, and hence the number of growth sites. Therefore, a cubic regression must be used to fit the control experiments. The linear growth rate can be derived from the first order constant (33, 34). In presence of NTMP, the addition rate of titrant rapidly

decreases to a minimum value due to NTMP adsorption, followed by a period of constant (inhibited) growth (R_i) (Figure 3B). This period is the inhibition period (t_i), which was determined from the second order derivative plot (Figure 3C). A linear regression was used to fit this period. After a while, the growth rate increases rapidly again to a value (R_0) similar to that expected for uninhibited growth (control). If ultrasound is applied for 45 min, however, the Ca^{2+} addition rate increases during the inhibition period, and strikingly, the rate recovers much faster to the uninhibited value. It is not possible to determine a linear growth rate after ultrasonic treatment owing to the increase of total surface area by deagglomeration, attrition and crystal breakage. For this reason, only the volumetric growth rate, R ($mol\ g^{-1}\ min^{-1}$) can be determined. Hereafter, the term "growth rate" always refers to the volumetric growth rate. These experiments have been done over a range of NTMP concentrations at the same supersaturation ratio. In Figure 4, the length of the inhibition period and the values of the inhibited growth rates caused by addition of NTMP are shown (see table D1 in Appendix D for all data).

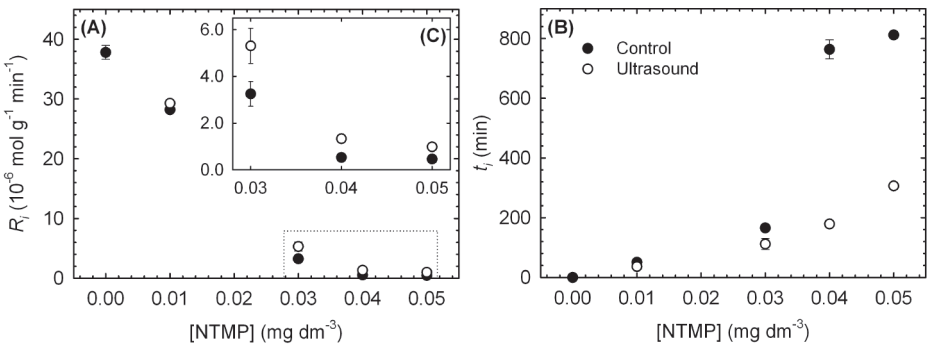

Figure 4. Effect of ultrasonic irradiation on the growth rates (A) and inhibition times (B) as a function of NTMP concentration. (C) Insert showing the effect of ultrasonic irradiation at an NTMP concentration above 0.03 mg dm^{-3}.

From the strong decrease in growth rate, it can be deduced that the presence of NTMP markedly decreased the reactivity of calcium carbonate crystals (Figure 4A). At low NTMP concentrations (0.00 – 0.03 mg dm^{-3}), the decrease in growth

rate is directly proportional to the NTMP concentration, while at higher concentrations, the growth rate approaches a minimum. A similar trend was observed for the growth inhibitors sodium triphosphate and polymaleic acid (35). Ultrasonic irradiation causes a strong enhancement of growth rate. An approximately twofold increase can be seen compared to the control experiments for 0.03, 0.04 and 0.05 mg dm^{-3} NTMP, respectively. The inhibition period of 36.4 min for 0.01 mg dm^{-3} NTMP is much shorter than the irradiation period of 45 min (Figure 4B). Therefore, the period of inhibited growth did not receive the full 45 min of irradiation. This explains why the growth rate enhancement is much smaller as opposed to the other experiments.

The recovery of growth rate following inhibition was strongly enhanced by ultrasonic irradiation (Figure 4B). While the reduction of the inhibition period by ultrasonic irradiation is relatively small at low NTMP concentrations, this reduction is much more profound at higher NTMP concentrations.

The observed enhancement of growth rate and reduction of inhibition period after ultrasonic irradiation, can be explained in part by the physical effect that ultrasound has on the crystals. From previous research using identical calcite crystals and equipment, it has been demonstrated that crystal deagglomeration, attrition and breakage occurs (16, 17). Consequently, the total surface area available for growth increases, and therefore the growth rate increases. Although broken crystal planes tend to have a lower linear growth rate because of their higher surface energy and hence higher solubility, it is likely that newly created crystal faces grow much faster as opposed to faces poisoned with NTMP.

In the experiments shown in Figure 5, fresh doses of NTMP (i.e., 0.03 mg dm^{-3}) were added after the inhibition period. This was done three times with and without ultrasonic irradiation. The rate recovered to the uninhibited value even after four equal doses of NTMP. Also, the inhibition periods for successive equal doses were very similar after the second NTMP dose. Furthermore, after each successive ultrasound treatment, the growth rate for the ultrasound experiment was approximately twice as high compared to the control experiment.

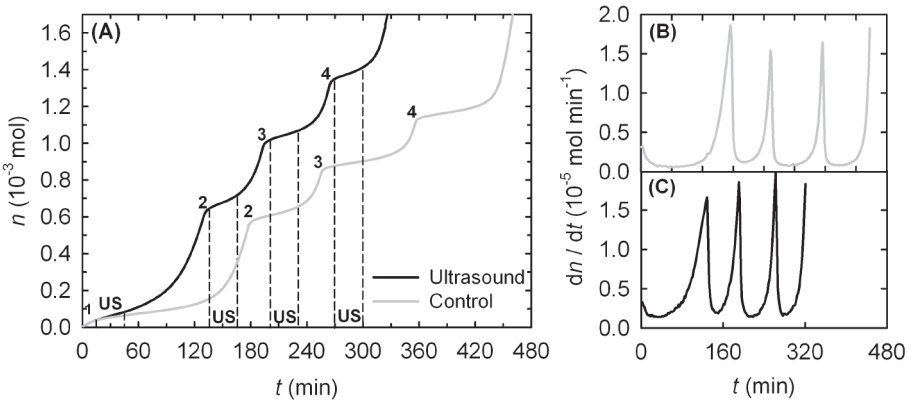

Figure 5. Effect of multiple doses of NTMP and multiple ultrasonic irradiations on calcite growth: (A) raw data of an ultrasound and a control experiment. At 1, 2, 3, and 4, a fresh dose of NTMP (0.03 mg dm^{-3}) was added; (B) derivative plot for control experiment; (C) derivative plot for ultrasound experiment. A smoothing spline method was applied for the curves in graphs B and C.

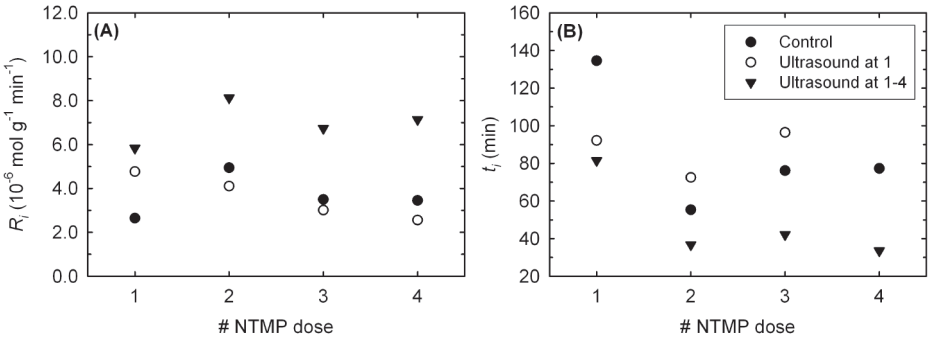

Figure 6. Effect of multiple doses of NTMP and multiple ultrasonic irradiations on calcite growth rate R_i and inhibition time t_i: (A) R_i as a function of NTMP dose for experiments with 0, 1, and 4 successive irradiation periods, respectively; (B) t_i as a function of NTMP dose for experiments with 0, 1 and 4 successive irradiation periods, respectively.

Without ultrasonic irradiation, multiple doses of NTMP caused t_i to increase and R_i to decrease (Figure 6). This suggests that NTMP had some permanent effect on the growing crystals. This effect was not observed when ultrasound was applied after each NTMP dose. With ultrasound, the growth rate and inhibition period are quite similar for each successive irradiation period. This suggests that the ultrasonic irradiation affected not only the crystals, but also the NTMP molecules.

8.3.3 *Mass spectroscopy: detection of breakdown products*

The mass spectra of the treated and untreated NTMP solution revealed the appearance of two distinctive peaks that increased with irradiation time (Figure 7).

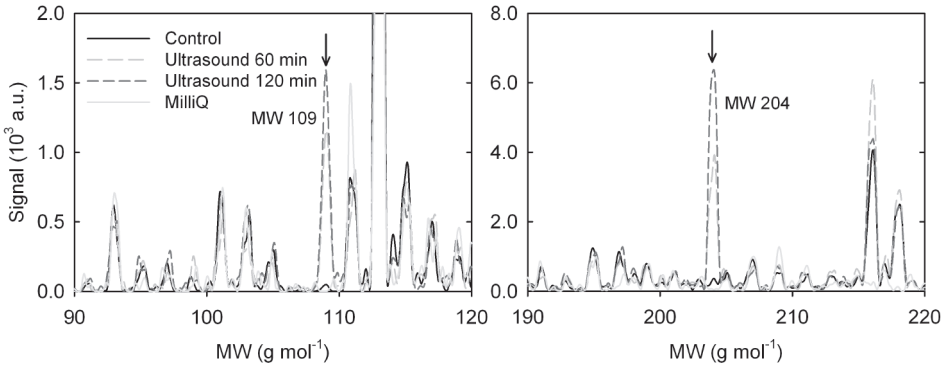

Figure 7. Mass spectra of MilliQ, control and sonicated samples, showing the appearance of two compounds with molecular weights (MW) of 109 and 204 only for the sonicated samples. For each sample, the average of two spectra was plotted.

The peak with molar weight 204 corresponds to the weight of the well known breakdown product imino(dimethylene)phosphonic acid (MW 205) (36-38). It is not clear however, if the peak at MW 109 corresponds to aminomethylphosphonic acid (MW 111) or hydroxymethylphosphonic acid (MW 112), because both have a similar molar mass. The spectra indicate that the stable C-P bond in NTMP can be cleaved by means of ultrasonic irradiation. Progressive loss of ligand-donor groups eventually generates products that do not effectively coordinate surface Ca^{2+} ions, and consequently, the reactivity of the crystals increases. In Figure 8, a tentative scheme of the sonochemical NTMP degradation is shown.

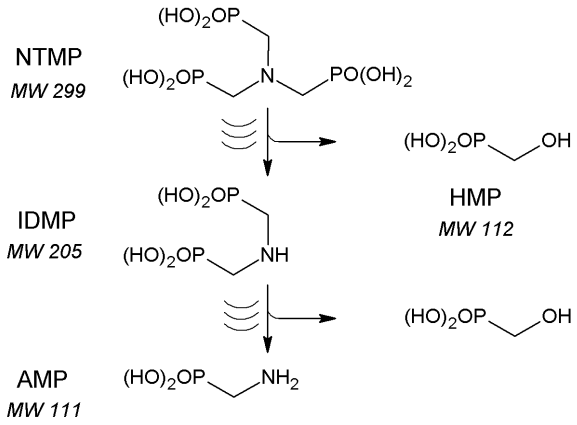

Figure 8. Tentative scheme of sonolytical NTMP degradation into imino(dimethylene)phosphonic acid (IDMP), aminomethylphosphonic acid (AMP) and hydroxymethylphosphonic acid (HMP). MW = Molar Weight.

No significant decrease in the NTMP peak was detected, showing that not all NTMP molecules where oxidized, even after 120 min of irradiation. This is supported by the growth experiments. The 45 min irradiation at, for example, 0.04 mg dm^{-3} NTMP, does not yield a similar or lower growth rate compared to the average growth rate measured at 0.03 mg dm^{-3} NTMP. This indicates that only a small amount of NTMP has been degraded.

In general, oxidation of dissolved species in the bulk solution by free radicals produced by sonochemical decomposition of water molecules, is not very efficient, especially in the presence of radical scavengers like HCO_3^- (28). Only a small portion of the total energy supplied to the system results in useful free-radical reactions.

On the other hand, pyrolysis in the hot bubble-bulk interface has been reported to be much less affected by other chemical components (39). Such pyrolysis might have played an important role, all the more since the estimated temperature of the bubble-bulk interface is sufficient to degrade NTMP, which already hydrolytically degrades at 533 K (36). Since cavitation primarily takes place on the particle surface (17, 40-43) where adsorbed NTMP is also present, most NTMP degradation is expected to occur on the crystal surface. To

conclude, the use of ultrasound for the reactivation of poisoned calcite seed crystals in water has been shown to be technically feasible and could improve the downstream removal of calcium carbonate from waste brines containing phosphonate growth inhibitors. However, the limitation of using ultrasound for this application on a large scale is that it is relatively inefficient with respect to the input energy. This drawback, which is encountered in basically all sonochemical waste water treatment applications, might be partially circumvented by using hybrid oxidation techniques (44). For example, a synergistic effect has been reported for the degradation of phenol in water by using ultrasound in combination with ozone (45). Another option would be to implement less energy consuming techniques for producing inertial cavitation, such as hydrodynamic cavitation (46).

8.4 Conclusions

It has been demonstrated that the use of ultrasound for the reactivation of poisoned calcite crystals in water is technically feasible. The inhibiting effect of NTMP on calcite crystal growth could be markedly mitigated under influence of ultrasonic irradiation. Recovery of growth rate following inhibition was strongly enhanced by the applied ultrasonic irradiation. In addition, a twofold increase of the inhibited growth rate was observed when ultrasound was applied. The results could be explained in part by the physical effect of ultrasound that causes breakage and attrition of poisoned crystals, which results in fresh surface area. Mass spectroscopy analysis of treated NTMP revealed that there is also a chemical effect of ultrasound that plays an important role. Several breakdown products were identified in NTMP solutions treated with ultrasound. This showed that the C-P bonds in NTMP can be cleaved, probably by means of physicochemically generated free radicals and/or pyrolysis in the hot bubble-bulk interface.

8.5 Acknowledgements

This work was performed in the TTIW-cooperation framework of

Wetsus, Centre of Excellence for Sustainable Water Technology (www.wetsus.nl). Wetsus is funded by the Dutch Ministry of Economic Affairs, the European Union Regional Development Fund, the Province of Fryslân, the City of Leeuwarden, and the EZ/Kompas program of "Samenwerkingsverband Noord-Nederland". The authors like to thank the participants of the research theme Concentrates for the discussions and their financial support. We would especially like to thank Ton van der Zande for the mass spectroscopy analysis.

8.6 References

(1) Knepper, T. P. Synthetic chelating agents and compounds exhibiting complexing properties in the aquatic environment. *TrAC, Trends Anal. Chem.* **2003**, *22*, 708-724.

(2) Reddy, M. M.; Nancollas, G. H. Calcite crystal growth inhibition by phosphonates. *Desalination* **1973**, *12*, 61-73.

(3) Jonasson, R. G.; Rispler, K.; Wiwchar, B.; Gunter, W. D. Effect of phosphonate inhibitors on calcite nucleation kinetics as a function of temperature using light scattering in an autoclave. *Chem. Geol.* **1996**, *132*, 215-225.

(4) Nakayama, N. Inhibitory effects of nitrilotris(methylenephosphonic acid) on cathodic reactions of steels in saturated $Ca(OH)_2$ solutions. *Corros. Sci.* **2000**, *42*, 1897-1920.

(5) Demadis, K. D.; Katarachia, S. D.; Koutmos, M. Crystal growth and characterization of zinc-(amino-tris-(methylenephosphonate)) organic-inorganic hybrid networks and their inhibiting effect on metallic corrosion. *Inorg. Chem. Commun.* **2005**, *8*, 254-258.

(6) Tang, Y. M.; Yang, W. Z.; Yin, X. S.; Liu, Y.; Yin, P. W.; Wang, J. T. Investigation of $CaCO_3$ scale inhibition by PAA, ATMP and PAPEMP. *Desalination* **2008**, *228*, 55-60.

(7) Demadis, K. D.; Mantzaridis, C.; Lykoudis, P. Effects of structural differences on metallic corrosion inhibition by metal-polyphosphonate thin films. *Ind. Eng. Chem. Res.* **2006**, *45*, 7795-7800.

(8) Rahardianto, A.; Gaoa, J.; Gabelich, C. J.; Williams, M. D.; Cohen, Y. High recovery membrane desalting of low-salinity brackish water: integration of accelerated precipitation softening with membrane RO. *J. Membr. Sci.* **2007**, *289*, 123-137.

(9) Yang, Q. F.; Liu, Y. Q.; David, H.; Semiat, R. Scaling salt removal by addition of inorganic particles. *J. Chem. Eng. Jpn.* **2008**, *41*, 6-12.

(10) Bremere, I.; Kennedy, M. D.; Johnson, A.; van Emmerik, R.; Witkamp, G. J.; Schippers, J. C. Increasing conversion in membrane filtration systems using a desupersaturation unit to prevent scaling. *Desalination* **1998**, *119*, 199-204.

(11) Sperlich, A.; Warschke, D.; Wegmann, C.; Ernst, M.; Jekel, M. Treatment of membrane concentrates: phosphate removal and reduction of scaling potential. *Water Sci. Technol.* **2010**, *61*, 301-306.

(12) Boels, L.; Tervahauta, T.; Witkamp, G. J. Adsorptive removal of nitrilotris(methylenephosphonic acid) antiscalant from membrane concentrates by iron-coated waste filtration sand. *J. Hazard. Mater.* **2010**, *182*, 855-862.

(13) Greenlee, L. F. Effect of antiscalant degradation on salt precipitation and solid/liquid separation of RO concentrate. *J. Membr. Sci.* **2010**, *366*, 48-61.

(14) Sluys, J. T. M.; Verdoes, D.; Hanemaaijer, J. H. Water treatment in a membrane-assisted crystallizer (MAC). *Desalination* **1996**, *104*, 135-139.

(15) Tomson, M. B. Effect of precipitation inhibitors on calcium carbonate scale formation. *J. Cryst. Growth* **1983**, *62*, 106-112.

(16) Boels, L.; Wagterveld, R. M.; Mayer, M. J.; Witkamp, G. J. Seeded calcite sonocrystallization. *J. Cryst. Growth* **2010**, *312*, 961-966.

(17) Wagterveld, R. M.; Boels, L.; Mayer, M. J.; Witkamp, G. J. Visualization of acoustic cavitation effects on suspended calcite crystals. *Ultrason. Sonochem.* **2011**, *18*, 216-225.

(18) Amara, N.; Ratsimba, B.; Wilhelm, A. M.; Delmas, H. Crystallization of potash alum: effect of power ultrasound. *Ultrason. Sonochem.* **2001**, *8*, 265-270.

(19) Guo, Z.; Jones, A. G.; Li, N.; Germana, S. High-speed observation of the effects of ultrasound on liquid mixing and agglomerated crystal breakage processes. *Powder Technol.* **2007**, *171*, 146-153.

(20) Guo, Z.; Zhang, M.; Li, H.; Wang, J.; Kougoulos, E. Effect of ultrasound on anti-solvent crystallization process. *J. Cryst. Growth* **2005**, *273*, 555-563.

(21) Sayan, P.; Sargut, S. T.; Kiran, B. Effect of ultrasonic irradiation on crystallization kinetics of potassium dihydrogen phosphate. *Ultrason. Sonochem.* **2011**, *18*, 795-800.

(22) Weiss, J. Radiochemistry of aqueous solutions. *Nature* **1944**, *155*, 748-750.

(23) Makino, K.; Mossoba, M. M.; Riesz, P. Chemical effects of ultrasound on aqueous solutions. Evidence for hydroxyl and hydrogen free radicals (•OH and •H) by spin trapping. *J. Am. Chem. Soc.* **1982**, *104*, 3537-3539.

(24) Suslick, K. S. Sonochemistry. *Science* **1990**, *247*, 1439-1445.

(25) Flint, E. B.; Suslick, K. S. The temperature of cavitation. *Science* **1991**, *253*, 1397-

1399.

(26) Kenneth, S. S. The sonochemical hot spot. *J. Acoust. Soc. Am.* **1991**, *89*, 1885-1886.

(27) Adewuyi, Y. G. Sonochemistry: environmental science and engineering applications. *Ind. & Eng. Chem. Res.* **2001**, *40*, 4681-4715.

(28) Olson, T. M.; Barbier, P. F. Oxidation kinetics of natural organic matter by sonolysis and ozone. *Water Res.* **1994**, *28*, 1383-1391.

(29) Sierka, R. A.; Amy, G. L. Catalytic effects of ultraviolet light and or ultrasound on the ozone oxidation of humic acid and trihalomethane precursors. *Ozone-Sci. Eng.* **1985**, *7*, 47-62.

(30) Kazmierczak, T. F.; Tomson, M. B.; Nancollas, G. H. Crystal growth of calcium carbonate. A controlled composition kinetic study. *J. Phys. Chem.* **1982**, *86*, 103-107.

(31) Brunauer, S.; Emmett, P. H.; Teller, E. *J. Am. Chem. Soc.* **1938**, *60*, 309.

(32) Mullin, J. W. *Crystallization*, Elsevier Butterworth-Heinemann: Burlington, MA, 2001.

(33) Matuchova, M.; Nyvlt, J. Determination of linear growth rates of crystals (I). Calculation of linear growth rates of individual crystal faces from overall rates. *Krist. Tech.* **1976**, *11*, 149-161.

(34) Nyvlt, J.; Matuchova, M. Determination of linear growth rates of crystals (II). The shape factors method. *Krist. Tech.* **1976**, *11*, 245-253.

(35) Kavanagh, A. M.; Rayment, T.; Price, T. J. Inhibitor effects on calcite growth at low supersaturations. *J. Chem. Soc. Faraday Trans.* **1990**, *86*, 965-972.

(36) Martell, A. E.; Motekaitis, R. J.; Fried, A. R.; Wilson, J. S.; Macmillan, D. T. Thermal-decomposition of EDTA, NTA, and nitrilotrimethylenephosphonic acid in aqueous solution. *Can. J. Chem.* **1975**, *53*, 3471-3476.

(37) Schowanek, D.; Verstraete, W. Hydrolysis and free radical mediated degradation of phosphonates. *J. Environ. Qual.* **1991**, *20*, 769-776.

(38) Nowack, B.; Stone, A. T. Degradation of nitrilotris(methylenephosphonic acid) and related (amino)phosphonate chelating agents in the presence of manganese and molecular oxygen. *Environ. Sci. Technol.* **2000**, *34*, 4759-4765.

(39) Cost, M.; Mills, G.; Glisson, P.; Lakin, J. Sonochemical degradation of p-nitrophenol in the presence of chemical components of natural waters *Chemosphere* **1993**, *27*, 1737-1743.

(40) Caupin, F.; Herbert, E. Cavitation in water: a review. *C. R. Phys.* **2006**, *7*, 1000-1017.

(41) Mørch, K. A. Reflections on cavitation nuclei in water. *Phys. Fluids* **2007**, *19*,

072104-072101-072104-072107.

(42) Mørch, K. A. Cavitation nuclei and bubble formation: A dynamic liquid-solid interface problem. *J. Fluids Eng.* **2000**, *122*, 494-498.

(43) Marschall, H. B.; Mørch, K. A.; Keller, A. P.; Kjeldsen, M. Cavitation inception by almost spherical solid particles in water. *Phys. Fluids* **2003**, *15*, 545-553.

(44) Gogate, P. R. Treatment of wastewater streams containing phenolic compounds using hybrid techniques based on cavitation: A review of the current status and the way forward. *Ultrason. Sonochem.* **2008**, *15*, 1-15.

(45) Lesko, T.; Colussi, A. J.; Hoffmann, M. R. Sonochemical decomposition of phenol: evidence for a synergistic effect of ozone and ultrasound for the elimination of total organic carbon from water. *Environ. Sci. Technol.* **2006**, *40*, 6818-6823.

(46) Jyoti, K. K.; Pandit, A. B. Water disinfection by acoustic and hydrodynamic cavitation. *Biochem. Eng. J.* **2001**, *7*, 201-212.

CARBOXYMETHYL INULIN BIOPOLYMERS: A GREEN ALTERNATIVE FOR PHOSPHONATE CALCIUM CARBONATE GROWTH INHIBITORS

9

There is a growing demand for environmentally friendly alternatives for phosphonate-based crystal growth inhibitors (or antiscalants) used in reverse osmosis desalination, which are nontoxic, biodegradable and free of phosphorous. The effectiveness of such an alternative, carboxymethyl inulin (CMI) biopolymers, in inhibiting calcium carbonate crystallization ($CaCO_3$), was compared to nitrilotris(methylenephosphonic acid) (NTMP) and 1-hydroxyethane-1,1-diphosphonate (HEDP). Their inhibiting effect on the seeded growth of calcite was investigated using the constant composition method at different solution compositions. The values of inhibited growth rates could be related well to a Temkin adsorption isotherm. Compared to HEDP and NTMP, CMI-20 and CMI-25 biopolymers exhibited an equally stronger inhibitory effect on the seeded growth of calcite, despite their different degrees of carboxylation. The ability of the inhibitor molecules to mitigate the spontaneous precipitation of $CaCO_3$ in a synthetic membrane concentrate was investigated as well. The results show that the ability of the biopolymers to mitigate precipitation is controlled by their degree of carboxylation. About 2.7 times more NTMP than CMI-25 is needed to achieve a similar precipitation inhibition. At high concentrations, both NTMP and CMI-25 induced twinning in the precipitating calcite crystals. This demonstrates that CMI biopolymers are effective $CaCO_3$ growth inhibitors, indicating their potential as a green alternative for phosphonates.

This chapter has been published as:

Boels, L.; Witkamp, G. J. Carboxymethyl inulin biopolymers: a green alternative for phosphonate calcium carbonate growth inhibitors. *Cryst. Growth Des.* **2011**, *11*, 4155-4165

9.1 Introduction

Scaling imposes limitations to the efficiency and yield of many industrial water treatment processes. With the aid of growth inhibitors (or antiscalants), primarily comprising polyelectrolytes such as phosphonates or polycarboxylates, scaling of inorganic compounds (e.g., $CaCO_3$) from aqueous solutions can be prevented or retarded at far substoichiometric antiscalant concentrations (1-8).

Phosphonates are very effective antiscalants and, therefore, widely used in reverse osmosis desalination processes (9). Unfortunately, the discharge of a membrane concentrate, or waste brine, containing phosphonates is problematic, especially in those cases where large surface water is absent (10-12). Phosphonates contribute to the total phosphate content and are considered to be compounds that promote eutrophication of the receiving surface water (13). In addition, the phosphonates used as antiscalant have not been identified to occur naturally and, despite their resistance against degradation, release aminomethylphosphonic acid as a metabolite (14-16).

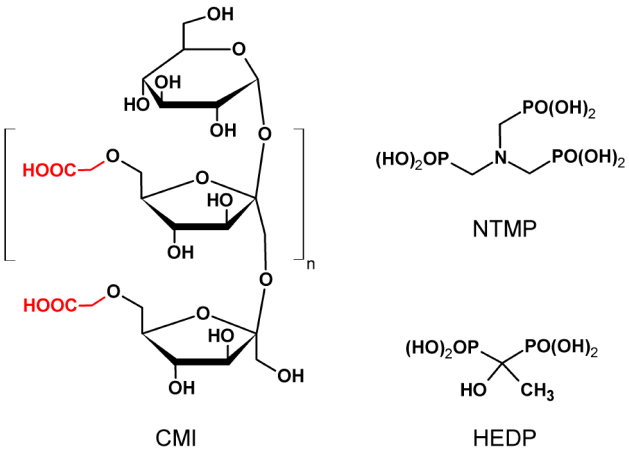

Figure 1. Chemical structures of carboxymethyl inulin (CMI) biopolymer, nitrilotris(methylene phosphonic acid) (NTMP) and 1-hydroxyethane-1,1-diphosphonate (HEDP), used in this study. The added carboxylate moieties of CMI are highlighted in red.

Increased government awareness of this environmental problem rapidly imposes more and more severe restrictions on concentrate disposal. As a result, the downstream treatment of concentrates has received considerable attention in order to improve water recoveries and reduce the size and impact of concentrate streams before discharge (17-22). However, the best way to avoid the discharge of phosphonates is by eliminating their use.

A promising alternative for phosphonates may be found in carboxymethyl inulin (CMI) biopolymers (Figure 1). CMI is produced by carboxymethylation of inulin, the latter extracted from the roots of chicory plants (23, 24). Inulin is a linear polydisperse fructan (i.e., polysaccharide of fructose) consisting mainly, if not exclusively, of fructose molecules which are linked by β (2←1) bonds. A glucose molecule typically, but not necessarily, resides at the end of the fructose chain linked by an α (1←2) bond. The chain lengths of these fructans range from 2 to 60 units, with an average degree of polymerization of 10 (25). Inulin has many food related usages, such as sweetener, dietary fiber and fat substitute (25, 26).

CMI biopolymers are, in contrast to other phosphonate-free antiscalants (polyacrylic acids), nontoxic and inherently biodegradable. It has been shown that the toxicity of CMI is negligible and comparable with those of other polycarboxylates used in food applications (27, 28).

Recently, the use of CMI biopolymers in controlling crystallization processes has become an active field of research (29). The inhibitory effects of CMI biopolymers on the growth of hydroxy apatite (30) and calcium oxalate (31) were reported. Also, Verraest et al. reported that a CMI biopolymer and a commercial copolymer of acrylate and maleate have a comparable inhibitory effect on $CaCO_3$ crystallization (32). On the other hand, the performance of the CMI biopolymer was reported to be far inferior compared to that of the phosphonate diethylenetriaminepenta(methylenephosphonic acid) as $CaCO_3$ scale inhibitor for oil-field well bores (33). The applicability of modified inulin biopolymers to control silica scaling has been investigated as well (34, 35).

The principal aim in the present work is to investigate whether or not CMI biopolymers can replace phosphonate $CaCO_3$ growth inhibitors. For this,

the inhibition of $CaCO_3$ crystallization by CMI biopolymers with different degrees of carboxylation and the phosphonates nitrilotris(methylene-phosphonic acid) (NTMP) and 1-hydroxyethane-1,1-diphosphonate (HEDP) (Figure 1) was investigated. First, their inhibitory effect on the seeded crystal growth of calcite was measured using the constant composition method (36). Second, their ability to delay the spontaneous precipitation of $CaCO_3$ in a synthetic membrane concentrate was investigated.

9.2 Experimental section

9.2.1 Materials

All solutions were prepared using high quality water (Milli-Q Reagent Water System, resistivity > 18 MΩ cm). Sodium bicarbonate ($NaHCO_3$), calcium chloride ($CaCl_2.2H_2O$) and potassium chloride (KCl) were of analytical grade and were obtained from Boom (Meppel, The Netherlands). Nitrilotris(methylenephosphonic acid) (NTMP) and 1-hydroxyethane-1,1-diphosphonate (HEDP) were obtained from Sigma Aldrich in their acid form with a purity of > 97 % and 95 %, respectively.

Two purified CMI biopolymer aqueous solutions were obtained from Aquacare Europe ('s Hertogenbosch, The Netherlands), with an average degree of polymerization of 10 and an average number of 2 (CMI-20) and 2.5 (CMI-25) carboxylate moieties per fructose unit (Table 1).

Table 1. Properties of CMI biopolymer solutions as received. The numbers in the identification labels indicate the degree of substitution of the CMI biopolymer (i.e., -20 denotes 2 carboxylate moieties per fructose unit). Glucose and fructose are considered to be impurities.

Polymer name	M_w [(a)] **(*g mol*$^{-1}$)**	**Polymer (*wt* %)**	**Glucose (*wt* %)**	**Fructose (*wt* %)**
CMI-20	3221	40.03	0.20	0.40
CMI-25	3626	40.87	0.12	0.09

(a) average molar weight

Stock solutions of each growth inhibitor with a concentration of 3.35×10^{-4} M were prepared every week and stored without exposure to light at 277 K.

9.2.2 Calcite seed crystals

Calcite seed crystals were prepared by slowly adding 2 dm^3 of a 0.20 M calcium chloride solution to 2 dm^3 0.20 M sodium carbonate solution at 298 K (37). The freshly precipitated seed crystals were aged overnight in mother liquor and were subsequently washed with Milli-Q water each day for one week. Afterward, the washed seed crystals were aged for 3 weeks. Then the crystals were filtered, washed with 600 ml of Milli-Q water and two portions of 50 mL pure ethanol, and dried under vacuum at room temperature. The dried crystals were characterized by scanning electron microscopy (Jeol JSM-6480 LV), high resolution Raman spectroscopy (Horiba/Jobin Yvon, Labram HR L/2/719) and nitrogen adsorption (Micromeritics Tristar 3000).

The specific surface area of the seed crystals was found to be 0.264 ± 0.014 $m^2\ g^{-1}$ as determined with a five-point BET method (38) on three replicate samples. The Raman spectra confirmed that the crystals were pure calcite with characteristic absorption bands at 1085 and 712 cm^{-1}. SEM pictures revealed that the seeds consisted of interpenetrated conglomerates of rhombohedral shaped crystals with an edge length of around 15 μm (Figure 2). Seeds from the same batch were used throughout all experiments.

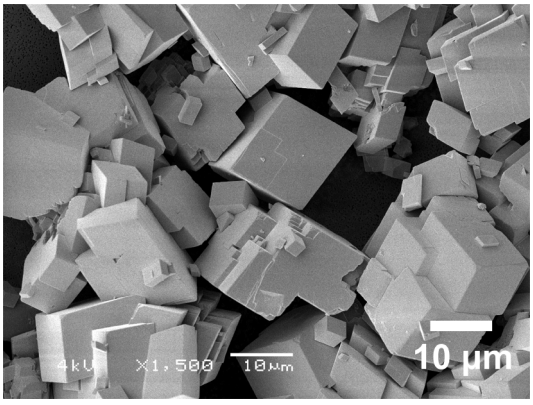

Figure 2. SEM picture of the employed calcite seed crystals. The crystals appeared as interpenetrated conglomerates with a size of around 15 μm.

9.2.3 Constant composition calcite growth experiments

A double walled thermostated (298 ± 0.1 K) glass reactor equipped with a floating magnetic stirrer bar (Nalgene) to minimize any grinding effects was used. For the control of pH, a combination pH electrode (Syntrode, Metrohm) in combination with two coupled automatic burets (Metrohm Titrino 785 and Dosimat 665) was used. The pH electrode was calibrated every day using 3 standard buffer solutions.

Metastable working solutions (Table 2) were prepared by addition of 500 cm^3 calcium solution to a 500 cm^3 bicarbonate solution, stirred at 400 rpm, in the reactor. Before addition of the calcium solution, an aliquot of inhibitor stock solution was injected to the carbonate solution to obtain the desired inhibitor concentration in the range of $0.20 \times 10^{-7} – 1.35 \times 10^{-7}$ M. Potassium chloride was added to all solutions to maintain the ionic strength constant at 0.1 M.

Table 2. Solution compositions examined in this study.

Solution	**[$CaCl_2$]** (*mM*)	**[$NaHCO_3$]** (*mM*)	**[KCl]** (*mM*)	$a_{Ca^{2+}}$ / $a_{CO_3^{2-}}$ [a]	**pH**	*S*[b]	**IS**[c] (*M*)
1	4	4	88	84.5	8.10	2.7	0.1
2	2	4	94	20.9	8.40	2.7	0.1
SC[d]	12	18	0	99.0	7.9	8.5	0.05

(a) activity ratio; (b) *S* = supersaturation ratio with respect to calcite; (c) IS = ionic strength; (d) SC = synthetic concentrate.

The pH of the stable working solution was adjusted to the desired value using a 0.05 M KOH or HCl solution. Experiments were started by the addition of 0.25 ± 0.01 g seed crystals as a slurry: the dry seeds were weighed into a syringe and a small amount of growth solution was drawn up into the syringe, and then the content was injected back into the growth solution with several rinses. After seed addition, the solution pH started to decrease as a result of calcite growth. This triggered the automatic burets to add concurrently equivalent amounts of calcium chloride and sodium carbonate solutions in order to achieve and maintain the pH at the target value (± 0.002 pH units). In this way, a constant degree of supersaturation was maintained throughout the growth experiment.

The seeds were allowed to grow until 30 cm^3 of titrant was consumed. In this way, dilution of inhibitor by the addition of inhibitor free titrant was kept to a minimum (< 5 %). Depending on the inhibitor concentration, total growth times ranged from 1 to 15 h.

During the experiment, aliquots of solution were rapidly removed through a septum, filtered by a 0.2 μm filter, and analyzed for the calcium content with inductive-coupled plasma spectrometry (Optima 3000XL, Perkin-Elmer) to verify the constancy of the degree of supersaturation. Growth experiments with inhibitor were done in duplicate, control experiments in triplicate.

All experiments were conducted at atmospheric pressure with ambient levels of CO_2. By keeping the reactor lid closed and all ports sealed during the experiments, the exchange of CO_2 between the atmosphere and the reactor solution was minimized.

9.2.4 Spontaneous $CaCO_3$ precipitation experiments

Spontaneous precipitation experiments were conducted using a nonseeded pH-drift method in a solution with a $CaCO_3$ supersaturation ratio comparable to that in real brackish water membrane concentrates (19). The synthetic concentrate solution was prepared by the simultaneous addition of 500 cm^3 of a 24 mM $CaCl_2.2H_2O$ solution and 500 cm^3 of a 36 mM $NaHCO_3$ solution (Table 2). Before preparation, both solutions were stored in a water bath at 298 K ± 0.1 K, and the inhibitor under investigation was added to the carbonate solution. The synthetic concentrate solution was stirred at 400 rpm and kept at 298 K ± 0.1 K, while the pH was measured continuously (Orbisint CPS11, Endress + Hauser). Throughout the experiments, aliquots of solution were removed through a septum, filtered by a 0.2 μm filter, and analyzed for the calcium content. The calcium concentration and pH reading were used to estimate the decrease in supersaturation ratio over time. The filtered crystals were analyzed with SEM and Raman spectroscopy (785 nm laser).

9.3 Results and discussion

9.3.1 $CaCO_3$ supersaturation and growth mechanism

The driving force for crystallization is defined as

$$\frac{\Delta\mu}{\mathbf{R}T} = \nu \ln(S) \qquad (1)$$

where **R** (*J mol*$^{-1}$ *K*$^{-1}$) is the gas constant, *T* (*K*) is the absolute temperature, $\Delta\mu$ (*J mol*$^{-1}$) is the change in chemical potential, υ is the number of ions in the formula unit, and *S* is the supersaturation ratio. For $CaCO_3$, the supersaturation ratio, *S*, is best expressed in terms of activities (39)

$$S = (IAP/K_{sp})^{1/\upsilon} \qquad (2)$$

where *IAP* is the ion activity product (defined as $a\mathrm{Ca}^{2+} \cdot a\mathrm{CO}_3^{2-}$) and K_{sp} (3.36×10^{-9}) is the thermodynamic solubility product (40). The chemical speciation of each solution was computed from the measured pH and the total concentration of salts ($CaCl_2$, $NaHCO_3$, and KCl), using a computer program (Visual Minteq v2.53) containing mass-action equations, mass balance equations, charge-balance equations, and the Bronsted-Guggenheim-Scatchard specific ion interaction theory (SIT) (41-43) model for calculating activity coefficients.

At the relatively low supersaturation ratio (*S* = 2.7) used in the seeded calcite growth experiments, a metastable solution can be obtained in which precipitation is thermodynamically possible, but spontaneous precipitation is improbable due to slow kinetics. The metastable solutions used in this study showed a constant pH for at least 24 h, indicating that no spontaneous $CaCO_3$ precipitation occurred.

Direct observations of calcite growth by atomic force microscopy have confirmed that growth occurs by spiral growth (44, 45) or by two-dimensional surface nucleation (46, 47). However, these studies report different relationships between growth mechanisms and supersaturation ratio. Therefore, the exact

growth mechanism in the present study is not fully clear, even though preliminary growth experiments revealed a second-order dependence of growth rate on supersaturation, indicating a spiral growth mechanism according to classical crystal growth theory (39).

The observed linear dependence of the volumetric growth rate (R_v, mol min^{-1}) on the amount of inoculating seeds verified that calcite growth was primarily induced by added calcite crystals without interference from nucleation (Figure 3).

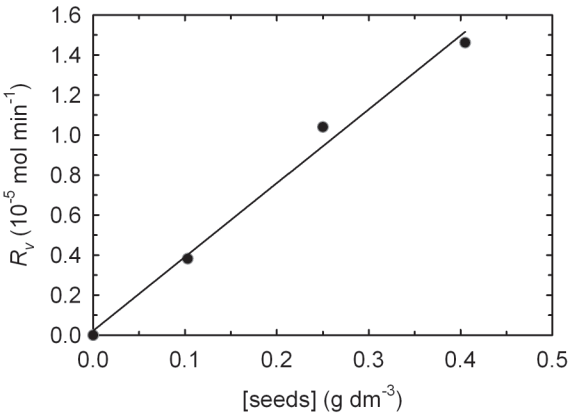

Figure 3. Plot of the volumetric growth rate (R_v) versus the amount of inoculating seeds. The data points can be fitted with a linear fit, which indicates the absence of interference from nucleation throughout the process of crystal growth. Conditions: $a\mathrm{Ca}^{2+}/a\mathrm{CO}_3^{2-}$ = 84.5, pH = 8.10, T = 298 K.

9.3.2 Growth rate and inhibition period determination

The effect of a growth inhibitor on the crystal growth of calcite can be described in terms of the values of reduced (or inhibited) growth rates and the length of the inhibition period. This is illustrated in Figure 4, where the added amount of Ca^{2+} ions (n) versus time (t) curves and the first and second order derivative plots of these curves for a control experiment and two experiments with inhibitor are shown.

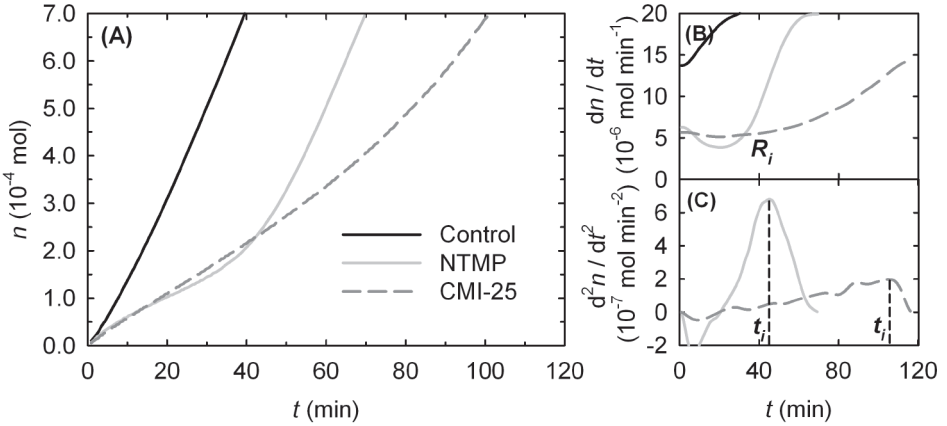

Figure 4. Effect of inhibitor addition to the calcite growth solution: (A) raw data of a control experiment and experiments with 2.93 × 10^{-8} M NTMP and 6.83 × 10^{-8} M CMI-25; (B) first order derivative plots; (C) second order derivative plots for determining the inhibition period t_i. n = amount of added Ca^{2+} ions. Conditions: $a$$Ca^{2+}$/ $a$$CO_3^{2-}$ = 20.9, pH = 8.40, T = 298 K. A smoothing spline method was applied for the curves in graphs B and C.

In the absence of growth inhibitors, an almost linear curve was obtained. The slope of this titrant addition versus time curve increases over time. Growth leads to an increase of crystal volume and surface, and the volumetric growth rate increases with the number of growth sites. For a single cubic crystal with ribs of length L, which grows with a linear growth rate, R ($m\ s^{-1}$) perpendicular to each side, the increase in crystal volume can be expressed as

$$V - V_0 = (L + 2Rt)^3 - L^3 = 6L^2Rt + 12L(Rt)^2 + 8(Rt)^3 \quad (3)$$

where V is the volume of the crystal and V_0 is the initial volume of the crystal. For a collection of differently sized crystals, eq 3 becomes

$$V - V_0 = A_0Rt + B(Rt)^2 + C(Rt)^3 = \frac{nM_W}{\rho} \quad (4)$$

where A_0 (m^2) is the initial surface area of the crystals, B and C are constants, n

(*mole*) is the amount of $CaCO_3$ grown, M_w (100.087 × 10^{-3} kg mol^{-1}) is the molar mass of calcite, and ρ (2710 kg m^{-3}) is the density of calcite (40).

Equation 4 shows that a cubic regression must be used to fit the control experiments (48, 49). The linear growth rate can be derived from the first order constant if A_0 is known.

Despite the equal supersaturation ratio, the linear growth rates measured in solutions 1 and 2 (no inhibitor) were 0.097 ± 0.005 and 0.152 ± 0.011 nm s^{-1}, respectively. This means that the driving force for crystallization alone is not adequate to fully describe the calcite growth kinetics. The $a Ca^{2+}$/ $a CO_3^{2-}$ activity ratio, for instance, is known to play a pivotal role in the kinetics of calcite growth (50, 51). In fact, a decreasing growth rate with an increasing $a Ca^{2+}$ / $a CO_3^{2-}$ ratio has been reported previously (50, 52).

In the presence of a growth inhibitor, the addition rate of titrant rapidly decreases to a minimum value, due to inhibitor adsorption, followed by a period of inhibited growth (R_i). This period will be called the inhibition period (t_i). After the inhibition period, the growth rate increases rapidly again to a value similar to that expected for uninhibited growth (R_0, control). Both CMI-25 and NTMP have a strong effect on the growth rate, but they exhibit a distinct difference in their behavior (Figure 4). In the case of NTMP (and also HEDP), inhibition is achieved quickly after addition of the seeds and lasts for a well-defined period, after which the rate rises rapidly to that of the control experiment. In contrast, the rate in the presence of CMI-25 biopolymer decreases somewhat more slowly, and at the end of the inhibition period (Figure 4C), recovery of the growth rate proceeds slowly. In fact, the rate after the inhibition period never attained that of the control. An identical behavior was observed for CMI-20.

9.3.3 Growth inhibitor adsorption mechanism

The growing calcite faces consist of steps with statistically formed kinks. As in the case of solute ions, these energetically favorable sites are preferential sites for the adsorption of inhibitor molecules. Once adsorbed, they inhibit growth by suppressing, or even blocking, the movement of kinks (i.e., the attachment of ions onto the kink sites) along the step. Suppressing the

propagation of kinks along the step hinders step displacement and poisons the crystal surface, inhibiting its growth. In situ measurements by atomic force microscopy of calcite have shown such poisoning by phosphates (46, 53) and phosphonates (54). Furthermore, related studies have shown that maximum growth inhibition can already be achieved when a small fraction of the crystal surface is covered by inhibitor, suggesting the preferential adsorption of inhibitor molecules at the most active growth sites (55, 56). If the faces of the crystal grow by the spiral growth mechanism, the coverage θ_l of kink sites in steps by inhibitor molecules may be related to the relative growth rate by (57).

$$\left(\frac{R_0 - R_i}{R_0}\right)^n = \alpha^n \theta_l \tag{5}$$

where α is the effectiveness factor for inhibitor adsorption at kinks. The exponent n = 1 represents the case in which inhibitor adsorption occurs at kink sites in steps as in the Kubota-Mullin model (58), whereas n = 2 represents adsorption on surface terraces. In the case of adsorption at kinks, the coverage θ_l of kink sites is proportional to the fractional coverage θ_s of the surface, which may be described by the Temkin (59) or well-known Langmuir (60) adsorption isotherms

$$\theta_s = Z(\ln C_0 + \ln C_i) \qquad \textit{Temkin} \tag{6a}$$

$$\theta_s = \frac{KC_i}{1 + KC_i} \qquad \textit{Langmuir} \tag{6b}$$

where K (M^{-1}), Z, and C_0 are constants and C_i (M) is the inhibitor concentration. In the Langmuir isotherm, the heat of adsorption is assumed to be constant and independent of θ_s. In the Temkin isotherm, however, the heat of adsorption decreases linearly with the increase of θ_s. The constant C_0 is expressed as

$$C_0 = \exp(Q^0_{diff} / \mathbf{R}T) \quad (7)$$

where Q^0_{diff} ($J\ mol^{-1}$), a positive quantity, is the initial differential heat of adsorption corresponding to a θ_s approaching zero. Both isotherms (eqs 6) may be combined with eq 5

$$\left(\frac{R_0 - R_i}{R_0}\right) = \alpha Z(\ln C_0 + \ln C_i) \quad (8a)$$

$$\left(\frac{R_0}{R_0 - R_i}\right) = \alpha^{-1}\left(1 + \frac{1}{KC_i}\right) \quad (8b)$$

Equation 8a shows that the Temkin model predicts a linear relationship between $(R_0 - R_i)/R_0$ and $\ln(C_i)$. The Langmuir model (eq 8b) predicts a linear relationship between $R_0/(R_0 - R_i)$ and $1/C_i$.

9.3.4 Calcite growth kinetics in the presence of inhibitor

The inhibitory effect of HEDP, NTMP, CMI-20, and CMI-25 on calcite growth was studied for two different solution compositions (Table 2) with the same degree of supersaturation (S = 2.7) at 298 K.

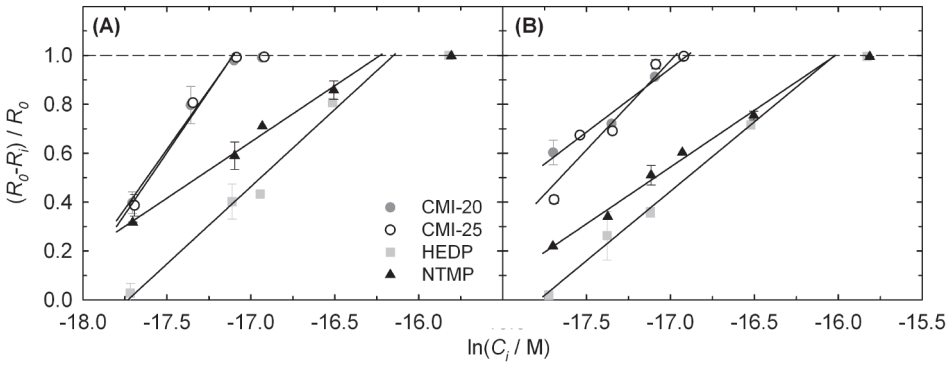

Figure 5. Calcite growth kinetics in the presence of CMI-25, CMI-20, NTMP, and HEDP. Data is plotted according to the dependences predicted by the Temkin model: (A) Solution 1, $a\mathrm{Ca}^{2+}/a\mathrm{CO}_3^{2-}$ = 84.5, pH = 8.10; (B) Solution 2, $a\mathrm{Ca}^{2+}/a\mathrm{CO}_3^{2-}$ = 20.9, pH = 8.40. At $(R_0 - R_i)/R_0 = 1$, "zero" growth occurs.

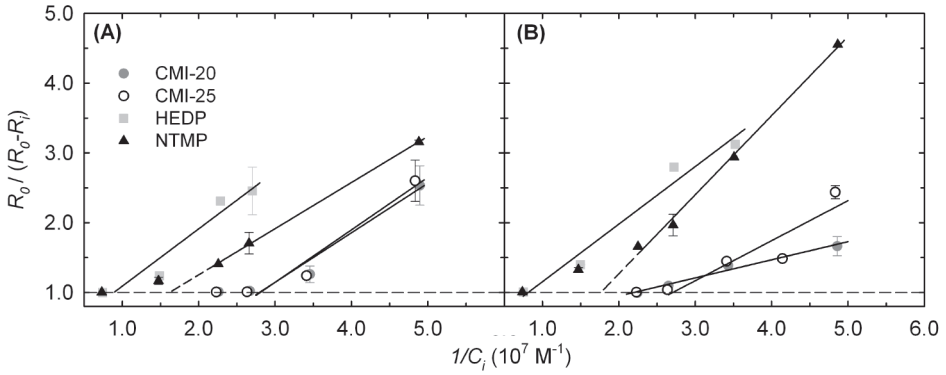

Figure 6. Calcite growth kinetics in the presence of CMI-25, CMI-20, NTMP, and HEDP. Data is plotted according to the dependences predicted by the Langmuir model; (A) Solution 1, $a\mathrm{Ca}^{2+}$/ $a\mathrm{CO}_3^{2-}$ = 84.5, pH = 8.10; (B) Solution 2, $a\mathrm{Ca}^{2+}$/ $a\mathrm{CO}_3^{2-}$ = 20.9, pH = 8.40. At $R_0/(R_0 - R_i) = 1$, "zero" growth occurs.

Temkin's model produced good fitting (Figure 5), which is in agreement with previous results of CMI biopolymer adsorption on hydroxyapatite crystals (30). Although the Langmuir model has often been used (6, 61, 62), it seems that, in comparison, the Temkin model does a better data fitting at the highest inhibitor concentrations (Figure 6). Especially the Langmuir fits on the data obtained for NTMP are poor. This may be related to the fact that the Langmuir model fails to account for the dependency of the heat of adsorption on surface coverage.

The linearity of the plots of Figure 5 for calcite growth in the presence of CMI biopolymers and phosphonates suggests that the inhibitory effect of both types of growth inhibitors is due to adsorption at kink sites in steps. Equation 8a predicts that, above a certain inhibitor concentration, C_i^*, zero growth rate will occur independent of C_i (i.e., $(R_0 - R_i)/R_0 = 1$). Experimentally, however, it was observed that, even at inhibitor concentrations above this threshold value, C_i^*, a very low residual growth rate occurs. From the slopes of the resulting straight lines, the initial differential heats of adsorption were evaluated according to eq 7. The values of C_i^*, Q_{diff}^0, and the correlation factors for each fit are listed in Table 3.

Table 3. Inhibitor adsorption (Temkin) parameters for the growth of calcite in solutions 1 and 2.

Inhibitor	$C_i^*{}_1$(a) ×10^{-7} (*M*)	$C_i^*{}_2$(b) ×10^{-7} (*M*)	$Q^0_{diff\ 1}$(a) (*kJ mol*$^{-1}$)	$Q^0_{diff\ 2}$(b) (*kJ mol*$^{-1}$)	**CC**$_1$(c)	**CC**$_2$
HEDP	0.974	1.11	43.92	44.05	0.9802	0.9939
NTMP	0.895	1.11	45.60	45.01	0.9904	0.9865
CMI-20	0.375	0.459	44.92	46.61	0.9843	0.9731
CMI-25	0.373	0.426	44.83	45.44	0.9816	0.9264

(a,b) The subscripts 1 and 2 denote solution 1 and 2, respectively. Solution 1: aCa^{2+}/ aCO$_3^{2-}$ = 84.5, pH = 8.10. Solution 2: aCa^{2+}/ aCO$_3^{2-}$ = 20.9, pH = 8.40; (c) correlation coefficient.

The relatively high positive values of Q^0_{diff} suggest that the adsorption is an exothermic reaction. This indicates that the energy gain in inhibitor binding is larger than the loss of energy from the dehydration process that accompanies the adsorption of inhibitor onto the calcite surface. Remarkably, there is no large difference between the values of Q^0_{diff} for the phosphonates and biopolymers. The inhibitory effect of CMI biopolymer molecules is markedly stronger in comparison to both phosphonates. This difference becomes larger with decreasing aCa^{2+}/ aCO$_3^{2-}$ ratio and increasing pH (Figures 5B and 6B).

The inhibitory effect of an inhibitor is strongly related to its ability of adsorbing and binding to the crystal surface. A positive surface charge facilitates the transport of anionic inhibitor molecules toward the calcite surface. Even at the highest employed pH value of 8.40, the calcite crystals most likely exhibited a positive surface charge (63). The CMI biopolymers and the phosphonates under investigation adsorb on the calcite surface by binding their carboxylic or phosphonate groups to the surface. Partially protonated groups are able to form strong complexes with surface calcium ions. Therefore, a comparison of the Ca^{2+} complexation constants for NTMP (Ca^{2+} + H$_1$NTMP = 4.0) (64, 65) and HEDP (Ca^{2+} + H$_1$HEDP = 3.3) (65, 66) may be used to explain the higher inhibitory effect of NTMP compared to HEDP. At the pH values investigated here (8.10 - 8.40), NTMP can form stronger complexes with (surface) calcium ions (64). In addition, NTMP contains one phosphonate group more than HEDP.

Besides the nature and number of functional groups, also the size of the

inhibitor molecule is of importance. The length of the biopolymer backbone allows many carboxylate groups to bind with surface ions over a wider area, binding the biopolymer very strongly to the calcite surface. Once adsorbed, a large molecule exhibits much steric hindering for approaching growth layers. This may account for the higher effectiveness of the biopolymers compared to the smaller phosphonates. In general, the effectiveness of a polyelectrolyte inhibitor will be served by a high anionic charge density obtained at high pH and low ionic strengths (67). This might explain the observed increase of the Q^0_{diff} values for CMI-20 and CMI-25 in solution 2, where the pH was 8.40.

The similar performance of CMI-20 and CMI-25 indicates that a higher number of carboxylate groups in the polymer does not necessarily cause a higher growth rate inhibition. If a large polymer molecule adsorbs on the calcite surface, remaining (unbound) carboxylate groups carry a negative charge, which may impede the approach of other negatively charged molecules. In addition, the configuration of adsorbed polymer will probably be not entirely flat, but instead a large part of the segments will be in tails or loops sticking out of the surface (67). This repulsive electrostatic potential can reduce the interaction between the calcite surface and polymer and, subsequently, lower its inhibition effectiveness (68). In addition, this effect can lead to the preferential adsorption of a narrow fraction with intermediate molar mass of molecules, which arrived first at the calcite surface (69). On the other hand, tails and/or loops sticking out of the surface are very difficult or even impossible for the crystal to overgrow, owing to the large steric hindering.

The molecular weights of the biopolymers are 1 order of magnitude higher than they are for both phosphonates. Therefore, a relatively higher amount of carboxylic acid groups in the fructan chain seems to be required for effective growth inhibition. Table 3 shows that the difference between the molar threshold value C_i^* of the biopolymers and the phosphonates is about a factor 2.5.

In Figure 7 plots of t_i (inhibition period) and C_i for each inhibitor in both working solutions are shown.

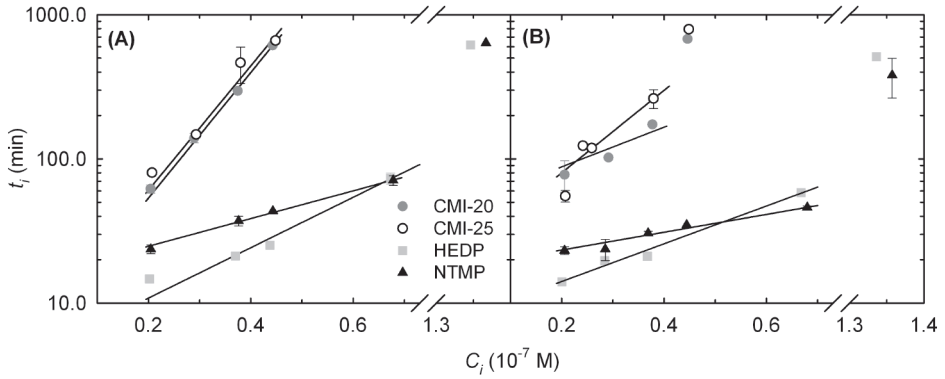

Figure 7. Calcite growth inhibition times of CMI-25, CMI-20, NTMP, and HEDP: (A) Solution 1, $a\mathrm{Ca}^{2+}/\ a\mathrm{CO}_3^{2-} = 84.5$, pH = 8.10; (B) Solution 1, $a\mathrm{Ca}^{2+}/\ a\mathrm{CO}_3^{2-} = 20.9$, pH 8.40. The graphs have semilog axis, which reveals that, at inhibitor concentrations below C_i^*, the inhibition period is an exponential function of C_i.

At inhibitor concentrations below C_i^*, the inhibition period seems to be an exponential function of C_i. Both biopolymers exhibit much longer inhibition times compared to those observed for the phosphonates at equal molar concentrations. The plots in Figure 7 show a similar sequence of effectiveness for the inhibitors as was observed in Figure 5. This shows that, for a particular inhibitor, the degree of growth rate inhibition is closely related to the length of the inhibition period. The inhibition periods measured in solution 2 are somewhat lower, which is probably due to the higher growth rate of calcite measured in solution 2 and the somewhat lower inhibitor effectiveness.

To understand why the growth inhibitors lose their growth inhibitory effect after a certain period is difficult, owing to the multitude of plausible mechanisms and to the complexity of the calcite surface structure (70). The free enthalpy involved in the incorporation of biopolymer or phosphonate inhibitor is so large that they are not incorporated in the crystal lattice by direct substitution for calcium or carbonate ions. A possible explanation for the existence of a distinct period of inhibition may be related to the formation of additional growth sites via two-dimensional surface nucleation. Even if growth is expected to be controlled by a spiral growth mechanism in absence of inhibitor, it might change from spiral growth into two-dimensional surface

nucleation growth in its presence. Inhibited growth rates are observed until all available inhibitor molecules are adsorbed on the newly created growth sites. At this point, newly created growth sites are not being poisoned anymore and the overall growth rate increases again, corresponding to the end of the inhibition period.

9.3.5 Spontaneous $CaCO_3$ precipitation inhibition in a synthetic membrane concentrate

Non-seeded, spontaneous precipitation experiments were performed at different inhibitor concentrations at 298 K in a synthetic membrane concentrate (Table 2). In the absence of an inhibitor, immediate and fast $CaCO_3$ precipitation occurred, as shown by the fast desupersaturation of the concentrate (Figure 8). Conversely, the presence of inhibitor caused a strong decrease in the precipitation rate (Figure 8). In analogy with the seeded growth experiments, the inhibitors inhibit precipitation only for a certain period of time, after which the precipitation rate strongly increases (inhibition period, t_i).

At the high initial supersaturation ratio (S = 8.5 and 4.4 with respect to calcite and vaterite, respectively) of the synthetic concentrate, precipitation proceeds through the formation of precursor phases, and consequently, kinetics rather than thermodynamics predominantly determine the properties of the precipitating crystals. In general, this leads to very different crystal morphologies when equal molar concentrations of growth inhibitors with a different degree of effectiveness are used. If the rate of precipitation is kept constant, however, it may become clear if phosphonate and CMI biopolymer molecules inhibit precipitation in a similar way.

To obtain a comparable inhibitory effect, the molar concentration of NTMP needs to be approximately 2.7 times higher than the concentration CMI-25 (Figure 8). This value corresponds well with the factor between the molar threshold value C_i^* of the biopolymers and the phosphonates in the seeded calcite growth experiments, which was approximately 2.5.

Some minor turbidity was observed within seconds after mixing, even at the highest employed inhibitor concentrations (4.48×10^{-6} M NTMP and 1.67×10^{-6} M CMI-25), indicating that the inhibitors primarily act by blocking growth

and not by inhibiting primary nucleation.

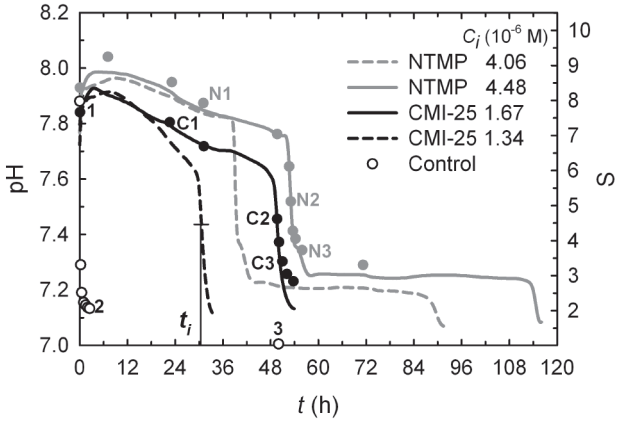

Figure 8. Inhibitory effect of CMI-25 and NTMP on the spontaneous precipitation of $CaCO_3$ in synthetic membrane concentrate. Recordings of the decline of solution pH (lines) and supersaturation S (dots) in time. A comparable degree of precipitation inhibition was achieved when 4.48×10^{-6} M NTMP and 1.67×10^{-6} M CMI-25 were added. The labeled positions indicate where collected crystals were characterized with SEM (Figure 10).

Some differences can be seen in the course of the pH curves for CMI-25 and NTMP. In contrast with the case of CMI-25, the slope of the NTMP curves in the inhibition period does not change with increasing inhibitor concentration; only the length of the inhibition period increases. Also, after the inhibition period the courses of the pH curves are quite different. Whereas the curves of CMI-25 decrease smoothly, the curves of NTMP have a shoulder at around pH 7.3. For both types of inhibitors, equilibrium (S = 1) is not attained for a long period after the inhibition period.

In Figure 9, measured inhibition periods versus inhibitor concentration of all inhibitors are shown. The results show that the ability of the biopolymers to mitigate precipitation is strongly controlled by their degree of carboxylation. The effectiveness of CMI-25 is superior compared to that of CMI-20, which demonstrates the importance of polyelectrolyte charge density for effective

precipitation inhibition under these conditions.

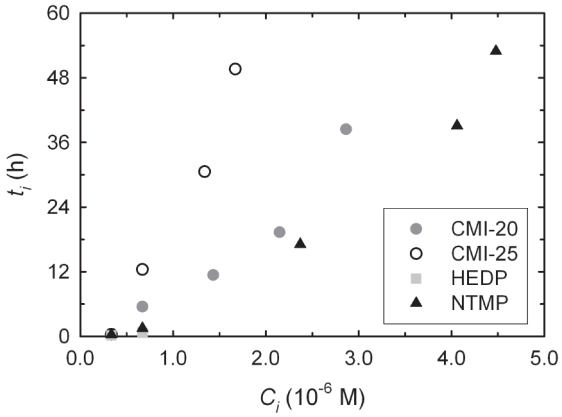

Figure 9. Inhibition periods as a function of CMI-25, CMI-20, HEDP, and NTMP concentration. Measurements were conducted in a synthetic concentrate: $a\mathrm{Ca}^{2+}$/ $a\mathrm{CO}_3^{2-}$ = 99.0, pH = 7.9, S = 8.5.

Furthermore, CMI-25 may complex more strongly to surface calcium ions by the presence of more partially deprotonated (lower acidity) carboxylic acid groups, since the deprotonation in CMI-25 may be suppressed more due to charge repulsion between neighboring groups. This positive relationship between the inhibitory effectiveness and an increasing charge density in CMI biopolymers has also been observed for the inhibition of calcium oxalate growth (31). In analogy with the trends observed in the seeded calcite growth experiments, both phosphonates are markedly less effective in comparison to the biopolymers, and NTMP seems to be more effective than HEDP.

The morphology and habit of the precipitating crystals were monitored in time in the experiments where a comparable precipitation inhibition was obtained in the presence of 1.67×10^{-6} M CMI-25 and 4.48×10^{-6} M NTMP respectively. The examined crystals collected in these experiments grew for a similar period, in which a comparable amount of $CaCO_3$ precipitated in time. This allows for a true evaluation of the effect that CMI-25 and NTMP, two very different inhibitor molecules, have on the morphology and habit of the precipitating crystals.

The SEM pictures revealed the formation of small amorphous shaped particles during the inhibition period in the presence of CMI-25 or NTMP (Figure 10 C1/N1). It appeared that, in the presence of CMI-25, higher order assemblies of temporarily stabilized round shaped nanoparticles with sizes of approximately 100 nm formed. This can be seen more clearly at higher magnifications (Figure 11A). Crystals grown in the presence of NTMP were larger in size and appeared to have roughened faces (Figure 11B).

After the inhibition period, when fast growth occurred, the crystals primarily comprised, surprisingly, twinned calcite crystals recognizable by the doubly terminated scalenohedron structures with a notch in the middle and crystals with blocky chevrons (Figure 10 C2-C3 & N2-N3). Both CMI-25 and NTMP inhibitors induced this twinning, and the only clear recognizable difference between the crystals grown in the presence of NTMP and CMI-25 is the number and size of the holes in the same faces of these twinned calcite crystals. This suggests that both inhibitors inhibit crystal growth in a similar way. Twinning was not observed at low inhibitor concentrations ($C_i < 1.0 \times 10^{-6}$ M).

The formation of holes is caused by blockage of step displacement by adsorbed inhibitor, which is known to facilitate step bunching (71, 72), and thus the development of very high macro steps during crystal growth. CMI-25 seems to cause fewer larger holes, while NTMP causes many small holes in the same crystal planes. Probably, this is related to their different molecular sizes causing a different degree of steric hindrance for approaching growth layers. As mentioned previously, it is highly unlikely that inhibitor molecules are being incorporated in the crystal lattice by direct substitution for calcium or carbonate ions. However, at the higher driving force for crystallization applied here, poisoned surface areas may be overgrown once the height of the macrosteps becomes large enough (i.e., inclusion formation).

A wide variety of crystal morphologies have been obtained through the addition of various block copolymers and biopolymers (73). For example, hollow shells (74), dumbbells (74), ellipsoids, plates, stacks of rhombohedra (75), and disks and rosettes (75) have been reported. Little is known about

twinning induced by additives, and only recently the formation of twinned calcite artificially grown from a solution to which Caspartin protein was added has been reported (76).

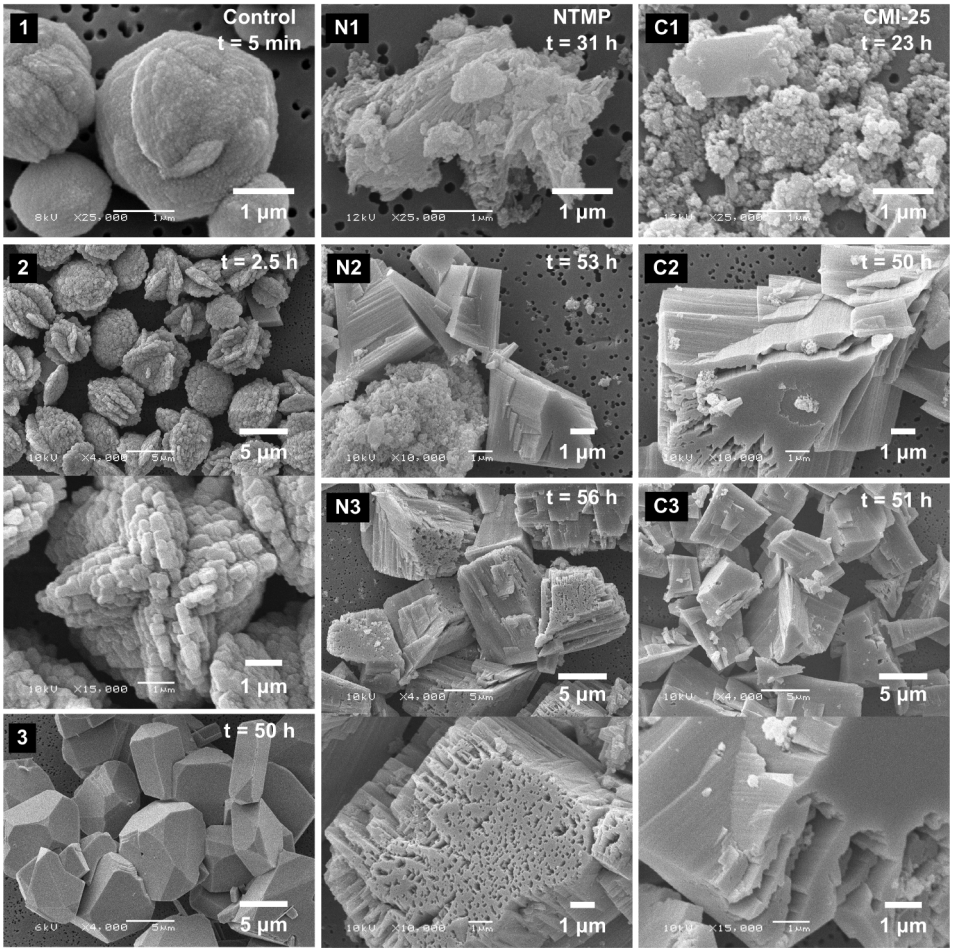

Figure 10. SEM pictures of crystals precipitated over time from synthetic membrane concentrate both in the absence and presence of NTMP and CMI-25 inhibitors. The NTMP and CMI-25 inhibitor concentrations were adjusted as such that a comparable degree of precipitation inhibition was observed (see Figure 8). Both CMI-25 and NTMP inhibitors induce twinning of the calcite crystals and cause holes in the same crystal faces. (1-3) Control experiment without growth inhibitor; (C1-C3) Experiment with 1.67×10^{-6} M CMI-25; (N1-N3) Experiment with 4.48×10^{-6} M NTMP.

The precipitates grown in the absence of inhibitor showed typical spherullitic

formations of vaterite that eventually transformed to the thermodynamically more stable calcite (Figure 10, picture 1-3). This was confirmed by Raman spectroscopy (Figure 12A). The spectra of the precipitates in the first 2.5 h showed the presence of multiple vaterite-specific bands at 1090 and 1074 cm^{-1} and 740 and 751 cm^{-1}. These bands are respectively attributed to the characteristic symmetrical stretching and in plane bending modes of the carbonate ion (77).

The formation of these polycrystalline vaterite spheres under similar conditions (298 K and S = 5.0 with respect to vaterite) has been reported before (78). In contrast with the calcite crystals formed in the presence of 1.67×10^{-6} M CMI-25 and 4.48×10^{-6} M NTMP, the calcite crystals had a regular rhombic shape with well-defined (104) faces and no twinning was observed (Figure 10, picture 3).

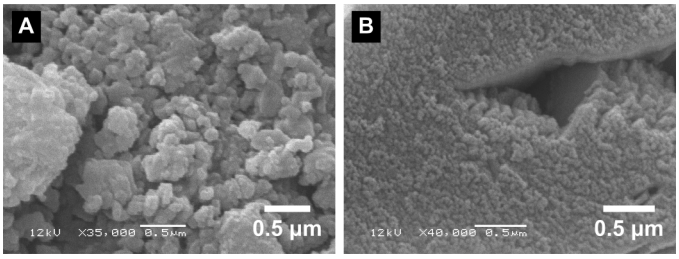

Figure 11. SEM pictures of roughened crystal surfaces precipitated from synthetic membrane concentrate during the inhibition period in the presence of (A) 1.67×10^{-6} M CMI-25 and (B) 4.48×10^{-6} M NTMP.

Raman analysis showed that in the presence of an inhibitor the initially formed precipitates are not fully amorphous and some characteristic absorptions bands for calcite at 712 and 1085 cm^{-1} (77) could be detected (Figure 12 B, C). Also, an absorption band at 1002 cm^{-1} in presence of NTMP was detected corresponding with phosphonate P-O vibrations (Figure 12 B). After the inhibition period, calcite seems to be the primary crystal phase because of the strong absorptions at 712 and 1085 cm^{-1}. The bands in the region 100 - 300 cm^{-1} that arise from translational and rotational modes of lattice vibration shift to higher wavenumbers over time due to an increasing degree of crystallinity.

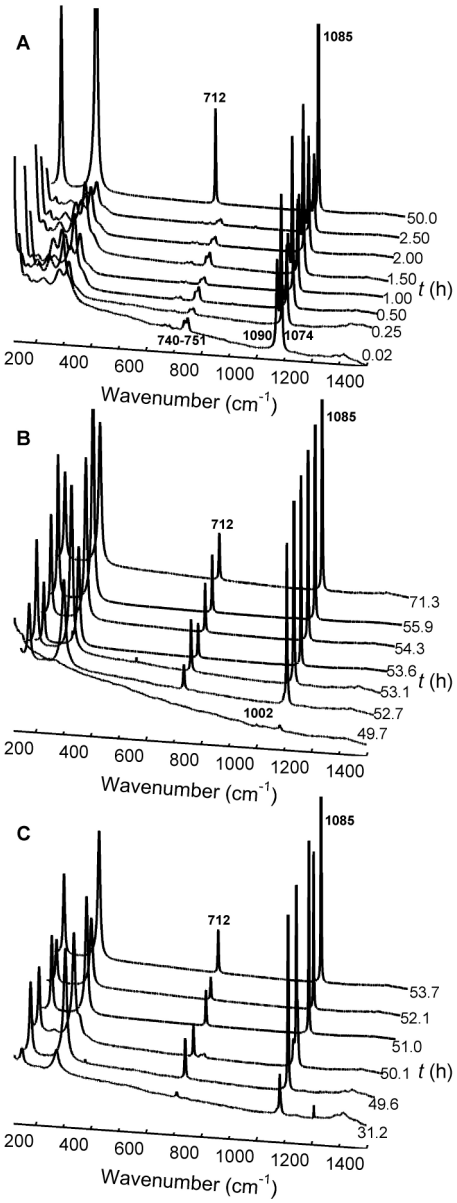

Figure 12. Raman spectra of the precipitates collected over time showing the appearance of characteristic absorption bands for calcite at 712 and 1085 cm^{-1} in the presence of (B) 4.48×10^{-6} M NTMP and (C) 1.67×10^{-6} M CMI-25. The control (A) shows characteristic absorptions for vaterite at 740 - 751 cm^{-1} with a final transition into pure calcite.

Our experimental results showed that the biopolymer molecules are more effective $CaCO_3$ crystallization inhibitors than the phosphonates NTMP and HEDP. Note that the development of scale in reverse osmosis desalination processes is a multistage process and is affected by a number of factors, these include supersaturation, pH, temperature, and flow velocity. In addition, the presence of other organic and inorganic contaminations may also influence the effectiveness of an antiscalant. Finally, the stability of both inhibitors toward (bio)degradation inside the process equipment might be an important factor as well. Therefore, additional research is needed to fully understand the behavior and applicability of CMI biopolymers as scale inhibitor.

9.4 Conclusions

The effectiveness of carboxymethyl inulin (CMI) biopolymer in inhibiting $CaCO_3$ crystallization was compared to that of nitrilotris(methylenephosphonic acid) (NTMP) and 1-hydroxyethane-1,1-diphosphonate (HEDP). The effect of each inhibitor on the seeded growth kinetics of calcite was investigated using the constant composition method. The inhibited growth rates could be related well by a Temkin adsorption isotherm. Under the experimental conditions of the present work (inhibitor concentration range 0.20×10^{-7} – 1.35×10^{-7} M, supersaturation ratio 2.7, and temperature 298 K), all inhibitors dramatically reduced the rate of calcite growth in the order CMI-25 ≈ CMI-20 > NTMP > HEDP. At the same supersaturation ratio, the difference between the inhibitory effect of CMI biopolymers and phosphonates became larger at higher pH and decreasing $a\mathrm{Ca}^{2+} / a\mathrm{CO}_3^{2-}$ ratio.

The spontaneous precipitation of $CaCO_3$ in a synthetic membrane concentrate could be mitigated best by CMI biopolymer. Unlike the negligible effect of the biopolymers' different degree of carboxylation on the seeded calcite growth kinetics, a higher degree of carboxylation strongly improved their ability to mitigate the spontaneous precipitation of $CaCO_3$. At equal molar concentrations, the inhibitors mitigated the spontaneous precipitation of $CaCO_3$ in the order CMI-25 > CMI-20 > NTMP > HEDP. At inhibitor concentrations of 1.67×10^{-6} M CMI-25 and 4.48×10^{-6} M NTMP, respectively, a similar 50 h period

of precipitation inhibition could be achieved. Scanning electron microscopy and Raman spectroscopy revealed that CMI-25 and NTMP inhibit precipitation in a similar way, and both inhibitors can induce twinning in the precipitating calcite crystals.

These results indicate that CMI biopolymers are an effective green alternative for nitrilotris(methylene phosphonic acid) (NTMP) and 1-hydroxyethane-1,1-diphosphonate (HEDP) in inhibiting $CaCO_3$ crystallization.

9.5 Acknowledgements

This work was performed in the TTIW-cooperation framework of Wetsus, Centre of Excellence for Sustainable Water Technology (www.wetsus.nl). Wetsus is funded by the Dutch Ministry of Economic Affairs, the European Union Regional Development Fund, the Province of Fryslân, the City of Leeuwarden, and the EZ/Kompas program of "Samenwerkingsverband Noord-Nederland". The authors would like to thank the participants of the research theme Concentrates for the discussions and their financial support. We would especially like to thank Ton van der Zande for the Raman analysis, Monika Jarzembowska for her assistance in the laboratory, and Martijn Wagterveld for his valuable comments. Also, we would like to thank Koos Baas for kindly donating the CMI biopolymer solutions and Arjen Postma for his support.

9.6 References

(1) Hasson, D.; Semiat, R.; Bramson, D.; Busch, M.; Limoni-Relis, B. Suppression of $CaCO_3$ scale deposition by anti-scalants. *Desalination* **1998**, *118*, 285-296.

(2) Reddy, M. M.; Nancollas, G. H. Calcite crystal growth inhibition by phosphonates. *Desalination* **1973**, *12*, 61-73.

(3) Dalas, E.; Koutsoukos, P. G. Calcium carbonate scale formation and prevention in a flow-through system at various temperatures. *Desalination* **1990**, *78*, 403-416.

(4) Xyla, A. G.; Mikroyannidis, J.; Koutsoukos, P. G. The inhibition of calcium carbonate precipitation in aqueous media by organophosphorus compounds. *J. Colloid Interface Sci.* **1992**, *153*, 537-551.

(5) Tang, Y. M.; Yang, W. Z.; Yin, X. S.; Liu, Y.; Yin, P. W.; Wang, J. T. Investigation of $CaCO_3$ scale inhibition by PAA, ATMP and PAPEMP. *Desalination* **2008**, *228*, 55-60.

(6) Reddy, M. M.; Hoch, A. R. Calcite crystal growth rate inhibition by polycarboxylic acids. *J. Colloid Interface Sci.* **2001**, *235*, 365-370.

(7) Wada, N.; Kanamura, K.; Umegaki, T. Effects of carboxylic acids on the crystallization of calcium carbonate. *J. Colloid Interface Sci.* **2001**, *233*, 65–72.

(8) Tzotzi, C.; Pahiadaki, T.; Yiantsios, S. G.; Karabelas, A. J.; Andritsos, N. A study of $CaCO_3$ scale formation and inhibition in RO and NF membrane processes. *J. Membr. Sci.* **2007**, *296*, 171-184.

(9) Knepper, T. P. Synthetic chelating agents and compounds exhibiting complexing properties in the aquatic environment. *TrAC, Trends Anal. Chem.* **2003**, *22*, 708-724.

(10) Nederlof, M. M.; van Paassen, J. A. M.; Jong, R. Nanofiltration concentrate disposal: experiences in The Netherlands. *Desalination* **2005**, *178*, 303-312.

(11) Squire, D. Reverse osmosis concentrate disposal in the UK. *Desalination* **2000**, *132*, 47-54.

(12) Greenlee, L. F.; Lawler, D. F.; Freeman, B. D.; Marrot, B.; Moulin, P. Reverse osmosis desalination: water sources, technology, and today's challenges. *Water Res.* **2009**, *43*, 2317-2348.

(13) Correll, D. L. The role of phosphorus in the eutrophication of receiving waters: a review. *J. Environ. Qual.* **1998**, *27*, 261-266.

(14) Steber, J.; Wierich, P. Properties of aminotris(methylenephosphonate) affecting its environmental fate, degradability, sludge adsorption, mobility in soils and bioconcentration. *Chemosphere* **1987**, *16*, 1323-1337.

(15) Nowack, B.; Stone, A. T. Degradation of nitrilotris(methylenephosphonic acid) and related (amino)phosphonate chelating agents in the presence of manganese and molecular oxygen. *Environ. Sci. Technol.* **2000**, *34*, 4759-4765.

(16) Demadis, K. D. Chemistry of organophosphonate scale inhibitors, part 4: stability of amino-tris-(methylene phosphonate) towards degradation by oxidizing biocides. *Phosphorus Sulfur* **2006**, *181*, 167-176.

(17) Gabelich, C. J.; Williams, M. D.; Rahardianto, A.; Franklin, J. C.; Cohen, Y. High-recovery reverse osmosis desalination using intermediate chemical demineralization. *J. Membr. Sci.* **2007**, *301*, 131–141.

(18) Rahardianto, A.; Gao, J.; Gabelich, C. J.; Williams, M. D.; Cohen, Y. High recovery membrane desalting of low-salinity brackish water: Integration of accelerated precipitation softening with membrane RO. *J. Membr. Sci.* **2007**, *289*, 123-137.

(19) Boels, L.; Tervahauta, T.; Witkamp, G. J. Adsorptive removal of nitrilotris(methylenephosphonic acid) antiscalant from membrane concentrates by iron-coated waste filtration sand. *J. Hazard. Mater.* **2010**, *182*, 855-862.

(20) Greenlee, L. F.; Testa, F.; Lawler, D. F.; Freeman, B. D.; Moulin, P. Effect of antiscalant degradation on salt precipitation and solid/liquid separation of RO concentrate. *J. Membr. Sci.* **2010**, *366*, 48-61.

(21) Sperlich, A.; Warschke, D.; Wegmann, C.; Ernst, M.; Jekel, M. Treatment of membrane concentrates: phosphate removal and reduction of scaling potential. *Water Sci. Technol.* **2010**, *61*, 301-306.

(22) Yang, Q.; Liu, Y.; Hasson, D.; Semiat, R. Removal of $CaCO_3$ scaling salt from RO concentrates by air-blow and inorganic inducers. *J. Chem. Eng. Jpn.* **2008**, *41*, 13-20.

(23) Verraest, D. L.; Peters, J. A.; van Bekkum, H. Oxidation an carboxymethylation of sucrose and inulin. *Zuckerindustrie* **1995**, *120*, 799-803.

(24) Verraest, D. L.; Peters, J. A.; Batelaan, J. G.; van Bekkum, H. Carboxymethylation of inulin. *Carbohydr. Res.* **1995**, *271*, 101-112.

(25) Niness, K. R. Inulin and oligofructose: what are they? *J. Nutr.* **1999**, *129*, 1402.

(26) Roberfroid, M. B. Inulin-type fructans: functional food ingredients. *J. Nutr.* **2007**, *137*, 2493S-2502S.

(27) Johannsen, F. R. Toxicological profile of carboxymethyl inulin. *Food Chem. Toxicol.* **2003**, *41*, 49-59.

(28) Coussement, P. A. A. Inulin and oligofructose: safe intakes and legal status. *J. Nutr.* **1999**, *129*, 1412.

(29) Hasson, D.; Shemer, H.; Sher, A. State of the art of friendly "green" scale control inhibitors: a review article. *Ind. Eng. Chem. Res.* **2011**, *50*, 7601-7607.

(30) Özlem, D.; Öner, M.; Cinel, Ö. The inhibitory effects of inulin biopolymers on the seeded growth of hydroxyapatite. *J. Ceram. Soc. Jpn.* **2010**, *118*, 579-586.

(31) Akin, B.; Öner, M.; Bayram, Y.; Demadis, K. D. Effects of carboxylate-modified, "green" inulin biopolymers on the crystal growth of calcium oxalate. *Cryst. Growth Des.* **2008**, *8*, 1997-2005.

(32) Verraest, D. L.; Peters, J. A.; van Bekkum, H.; van Rosmalen, G. M. Carboxymethyl inulin: a new inhibitor for calcium carbonate precipitation. *J. Am. Oil Chem. Soc.* **1996**, *73*, 55-62.

(33) Baraka-Lokmane, S.; Sorbie, K.; Poisson, N.; Kohler, N. Can green scale inhibitors replace phosphonate scale inhibitors?: carbonate coreflooding experiments. *Petrol. Sci. Technol.* **2009**, *27*, 427-441.

(34) Ketsetzi, A.; Stathoulopoulou, A.; Demadis, K. D. Being "green" in chemical water

treatment technologies: issues, challenges and developments. *Desalination* **2008**, *223*, 487-493.

(35) Demadis, K. D.; Mavredaki, E.; Stathoulopoulou, A.; Neofotistou, E.; Mantzaridis, C. Industrial water systems: problems, challenges and solutions for the process industries. *Desalination* **2007**, *213*, 38-46.

(36) Kazmierczak, T. F.; Tomson, M. B.; Nancollas, G. H. Crystal growth of calcium carbonate. a controlled composition kinetic study. *J. Phys. Chem.* **1982**, *86*, 103-107.

(37) Reddy, M. M.; Nancollas, G. H. Crystallization of calcium carbonate. 1. Isotopic exchange and kinetics. *J. Colloid Interface Sci.* **1971**, *36*, 166-172.

(38) Brunauer, S.; Emmett, P. H.; Teller, E. Adsorption of fases in multimolecular layers. *J. Am. Chem. Soc.* **1938**, *60*, 309.

(39) Mullin, J. W. *Crystallization*, Elsevier Butterworth-Heinemann: Burlington, MA, 2001.

(40) Lide, D. R. *Handbook of Chemistry and Physics*, Taylor & Francis Group, 2006.

(41) Brönsted, J. N. Studies on solubility IV. The principle of the specific interaction of ions. *J. Am. Chem. Soc.* **1922**, *44*, 877-898.

(42) Guggenheim, E. A.; Turgeon, J. C. Specific interaction of ions. *T. Faraday Soc.* **1955**, *51*, 747-761.

(43) Scatchard, G. Concentrated solutions of strong electrolytes. *Chem. Rev.* **1936**, *19*, 309-327.

(44) Hillner, P. E.; Gratz, A. J.; Manne, S.; Hansma, P. K. Atomic-scale imaging of calcite growth and dissolution in real time. *Geology* **1992**, *20*, 359-362.

(45) Gratz, A. J.; Hillner, P. E.; Hansma, P. K. Step dynamics and spiral growth on calcite. *Geochim. Cosmochim. Acta* **1993**, *57*, 491-495.

(46) Dove, P. M.; Hochella Jr, M. F. Calcite precipitation mechanisms and inhibition by orthophosphate: in situ observations by scanning force microscopy. *Geochim. Cosmochim. Acta* **1993**, *57*, 705-714.

(47) Teng, H. H.; Dove, P. M.; De Yoreo, J. J. Kinetics of calcite growth: surface processes and relationships to macroscopic rate laws. *Geochim. Cosmochim. Acta* **2000**, *64*, 2255-2266.

(48) Matuchova, M.; Nyvlt, J. Determination of linear growth rates of crystals (I). Calculation of linear growth rates of individual crystal faces from overall rates. *Krist. Tech.* **1976**, *11*, 149-161.

(49) Nyvlt, J.; Matuchova, M. Determination of linear growth rates of crystals (II). The shape factors method. *Krist. Tech.* **1976**, *11*, 245-253.

(50) Larsen, K.; Bechgaard, K.; Stipp, S. L. S. The effect of the Ca^{2+} to CO_3^{2-} activity

ratio on spiral growth at the calcite {1014} surface. *Geochim. Cosmochim. Acta* **2010**, *74*, 2099-2109.

(51) Stack, A. G.; Grantham, M. C. Growth rate of calcite steps as a function of aqueous calcium-to-carbonate ratio: independent attachment and detachment of calcium and carbonate ions. *Cryst. Growth Des.* **2010**, *10*, 1409-1413.

(52) Lin, Y. P.; Singer, P. C. Effects of seed material and solution composition on calcite precipitation. *Geochim. Cosmochim. Acta* **2005**, *69*, 4495-4504.

(53) Gratz, A. J.; Hillner, P. E. Poisoning of calcite growth viewed in the atomic force microscope (AFM). *J. Cryst. Growth* **1993**, *129*, 789-793.

(54) Reyhani, M. M.; Oliveira, A.; Parkinson, G. M.; Jones, F.; Rohl, A. L.; Ogden, M. I. In situ characterisation of calcite growth and inhibition using atomic force microscopy. *Int. J. Mod. Phys. B* **2002**, *16*, 25-33.

(55) Leung, W. H.; Nancollas, G. H. Nitrilotris(methylenephosphonic acid) adsorption on barium sulfate crystals and its influence on crystal growth. *J. Cryst. Growth* **1978**, *44*, 163-167.

(56) Zieba, A.; Sethuraman, G.; Perez, F.; Nancollas, G. H.; Cameron, D. Influence of organic phosphonates on hydroxyapatite crystal growth kinetics. *Langmuir* **1996**, *12*, 2853-2858.

(57) Sangwal, K. Kinetic effects of impurities on the growth of single crystals from solutions. *J. Cryst. Growth* **1999**, *203*, 197-212.

(58) Kubota, N.; Mullin, J. W. A kinetic model for crystal growth from aqueous solution in the presence of impurity. *J. Cryst. Growth* **1995**, *152*, 203-208.

(59) Temkin, M. I.; Pyzhev, V. Kinetics of ammonia synthesis on promoted iron catalysts. *Acta Physicochem. USSR* **1940**, *12*, 217-222.

(60) Langmuir, I. The constitution and fundamental properties of solids and liquids. Part I. Solids. *J. Am. Chem. Soc.* **1916**, *38*, 2221-2295.

(61) Lin, Y. P.; Singer, P. C. Inhibition of calcite crystal growth by polyphosphates. *Water Res.* **2005**, *39*, 4835–4843.

(62) Lin, Y. P.; Singer, P. C. Inhibition of calcite precipitation by orthophosphate: Speciation and thermodynamic considerations. *Geochim. Cosmochim. Acta* **2006**, *70*, 2530-2539.

(63) Eriksson, R.; Merta, J.; Rosenholm, J. B. The calcite/water interface: I. Surface charge in indifferent electrolyte media and the influence of low-molecular-weight polyelectrolyte. *J. Colloid Interface Sci.* **2007**, *313*, 184-193.

(64) Deluchat, V.; Bollinger, J.-C.; Serpaud, B.; Caullet, C. Divalent cations speciation with three phosphonate ligands in the pH-range of natural waters. *Talanta* **1997**,

44, 897-907.

(65) Popov, K.; Rönkömäki, H.; Lajunen, L. H. J. Critical evaluation of stability constants of phosphonic acids (IUPAC Technical Report). *Pure Appl. Chem.* **2001**, *73*, 1641-1677.

(66) Claessens, R. A. M. J.; van der Linden, J. G. M. Stability constants of tin(II) and calcium diphosphonate complexes. *J. Inorg. Biochem.* **1984**, *21*, 73-82.

(67) Cafe, M. C.; Robb, I. D. The adsorption of polyelectrolytes on barium sulfate crystals. *J. Colloid Interface Sci.* **1982**, *86*, 411-421.

(68) Adam, U. S.; Robb, I. D. Adsorption and exchange of polyelectrolytes on crystal surfaces. *J. Chem. Soc. Faraday Trans. 1* **1983**, *79*, 2745-2753.

(69) Geffroy, C.; Persello, J.; Foissy, A.; Lixon, P.; Tournilhac, F.; Cabane, B. Molar mass selectivity in the adsorption of polyacrylates on calcite. *Colloid Surf. A* **2000**, *162*, 107-121.

(70) Paquette, J.; Reeder, R. J. Relationship between surface structure, growth mechanism, and trace element incorporation in calcite. *Geochim. Cosmochim. Acta* **1995**, *59*, 735-749.

(71) Ohtani, N.; Katsuno, M.; Aigo, T.; Fujimoto, T.; Tsuge, H.; Yashiro, H.; Kanaya, M. Step bunching behaviour on the {0001} surface of hexagonal SiC. *J. Cryst. Growth* **2000**, *210*, 613-622.

(72) Yang, Q.; Liu, Y.; Gu, A.; Ding, J.; Shen, Z. Investigation of calcium carbonate scaling inhibition and scale morphology by AFM. *J. Colloid Interface Sci.* **2001**, *240*, 608-621.

(73) Cölfen, H. Precipitation of carbonates: recent progress in controlled production of complex shapes. *Curr. Opin. Colloid Interface Sci.* **2003**, *8*, 23-31.

(74) Cölfen, H.; Antonietti, M. Crystal design of calcium carbonate microparticles using double-hydrophilic block copolymers. *Langmuir* **1998**, *14*, 582-589.

(75) Butler, M. F.; Glaser, N.; Weaver, A. C.; Kirkland, M.; Heppenstall-Butler, M. Calcium carbonate crystallization in the presence of biopolymers. *Cryst. Growth Des.* **2006**, *6*, 781-794.

(76) Pokroy, B.; Kapon, M.; Marin, F.; Adir, N.; Zolotoyabko, E. Protein-induced, previously unidentified twin form of calcite. *Proc. Natl. Acad. Sci. U.S.A.* **2007**, *104*, 7337-7341.

(77) Behrens, G.; Kuhn, L. T.; Ubic, R.; Heuer, A. H. Raman spectra of vateritic calcium carbonate. *Spectrosc. Lett.* **1995**, *28*, 983-995.

(78) Andreassen, J. P. Formation mechanism and morphology in precipitation of vaterite - nano-aggregation or crystal growth? *J. Cryst. Growth* **2005**, *274*, 256-264.

GENERAL DISCUSSION AND PERSPECTIVES

10

The development of technologies that can remove phosphonate antiscalants from membrane concentrates is of considerable environmental value, as well as a necessity to comply with the increasing regulatory pressure on concentrate disposal. Also, the technical ability to remove antiscalants would be of significant value for concentrate demineralization processes. This work presented a new process that removes phosphonates from membrane concentrates by means of adsorption onto iron oxy-hydroxides. This process also allows for the recovery of the phosphonates, which offers the possibility to reuse them as antiscalant. The question rises whether this phosphonate removal technology can be employed for other phosphonate containing waste water streams as well. Alternatively, the undesired discharge of phosphonates may also be avoided by minimizing their use or by replacing them with environmentally friendly alternative antiscalants. Smart sensors that predict the risk of scaling at an early stage can help to minimize the dosage of phosphonate antiscalants. This work contributed to the development of such a sensor by showing that ultrasonic irradiation can be used as an actuator for crystal growth and precipitation. In this final chapter, the results of the work presented in this thesis are being discussed and, where possible, placed into perspective.

10.1 Concentrate treatment

10.1.1 Phosphonate removal and recovery

Porous iron oxy-hydroxides have a high affinity for phosphonate anions, which leads to favorable adsorption characteristics and high adsorption capacities. In addition, this affinity is maintained at increasing salinity and phosphonate is preferentially adsorbed over other anions present in membrane concentrates. Therefore, iron oxy-hydroxides show relatively high phosphonate adsorption capacities compared to anion exchange resins and activated carbon.

The presence of calcium increases the phosphonate adsorption capacity of iron oxy-hydroxides substantially, which is beneficial for the adsorption process in membrane concentrates. Thus, contradictory as it seems, phosphonates are added when calcium is present, whereas calcium in turn helps to remove phosphonates again. The kinetics of NTMP adsorption onto iron oxy-hydroxides can be predicted fairly well with models that consider either combined film-pore or combined film-surface diffusion as the main mechanisms for mass transport. The intraparticle diffusion of phosphonate through the pore liquid or over the surface of the pore walls is the rate limiting step in the adsorption process.

The phosphonate that has been removed by adsorption onto iron oxy-hydroxide can be desorbed by treating the saturated adsorbent with a sodium hydroxide base solution. This means that NTMP can be recovered from the RO concentrate, under the condition that the phosphonate can be removed from the basic regeneration solution again. This can be achieved by nano-filtration or by precipitating the phosphonate with calcium. Nano-filtration is technically more attractive, because the phosphonate can be recovered without the presence of calcium and an additional solid/liquid separation step.

The use of adsorption technology to remove and recover phosphonates is a viable option, due to its efficiency and its technical feasibility to achieve low levels of phosphonate. By treating concentrates with the adsorption process developed here, the discharge of phosphonates can be avoided and it helps to improve any further demineralization processes. Also, the opportunity to

recover and reuse the phosphonates helps to save the world's non-renewable phosphorous resources.

10.1.2 Zero liquid discharge

As the number and size of RO desalination plants increases, so does the resultant concentrate volumes, and inevitably, the challenges of disposing concentrates. An alternative for concentrate disposal may be reduction of its volume by zero liquid discharge (ZLD) processes, because not only the chemical additives like antiscalants impose an environmental threat, also the accumulated salts in the concentrate can locally affect the eco-systems in the receiving water.

A ZLD process is a high water product recovery process where either the final concentrate is disposed of within the plant boundary (e.g., in an evaporation pond) or the process produces solids (i.e., salts) for disposal. The use of evaporation ponds is much less feasible for large concentrate streams, and therefore demineralization should be done via enhanced precipitation/ crystallization techniques. The precipitation of mineral salts occurs in a sequence according to their solubility and propensity for coprecipitation and adsorption. Besides the supersaturation, the efficiency of precipitation is also dependent on the residence time, agitation and the presence of other species, such as antiscalants. Therefore, these precipitation processes can be improved when antiscalants are removed first via adsorption onto iron oxy-hydroxide.

Although ZLD sounds promising because the discharge of a concentrate stream is being avoided, it also means that desalination processes produce solid waste streams instead. The question raises what to do with the solid waste, which needs to be transported and disposed of at suitable locations. Alternative applications of the produced salt may be found in some cases when the specifications of the salt product can be controlled. Although the high water product recovery helps to off set the additional energy costs for extracting the salts in a solid form, ZLD is currently very expensive. However, with increasing regulatory pressure and the development of more energy efficient precipitation technologies, ZLD may become common practice in future desalination

processes.

10.2 Minimizing the use of phosphonate antiscalants

Optimization of antiscalant dosage may be achieved by improving the prediction of the risk of scaling using on-line sensoring techniques. Some work was presented on the actuator part of a sensor that enhances precipitation and crystal growth by the application of ultrasound. The cavitation phenomena that occur by applying ultrasound can enhance crystal growth, even in the presence of a phosphonate antiscalant. This indicates that ultrasound can indeed serve as actuator for calcium carbonate crystallization and possibly for other scaling salts. Recent results show that ultrasound reduces the induction time of calcium carbonate crystallization, but it has no effect on the primary crystal nucleation (1). Thus, it seems that the presence of crystal nuclei with a certain critical size is a prerequisite for ultrasound to actuate crystallization.

Another way to minimize antiscalant dosage lies in acquiring a better understanding of the mechanisms involved in nucleation inhibition and in crystal growth inhibition. The presented crystal growth experiments revealed that antiscalants loose their inhibitory effect after a distinct period of time. It would be of major interest to understand this phenomenon better so that more effective antiscalants or antiscalant mixtures can be formulated. If the antiscalant is more effective, less is needed to obtain the same effective scale control.

Besides calculating the chemical speciation, it would also make sense to take into account the inhibiting effect of present natural organic matter and metal ions when estimating the required dosage of phosphonates. These compounds are known to inhibit crystallization as well, and therefore, depending on the type and amounts of these compounds, less phosphonates may actually be needed for scale prevention.

10.3 Alternatives for phosphonate antiscalants

Although it is technically possible to remove phosphonates, the best way

to remove phosphonates from membrane concentrates is by eliminating their use. This work showed that there are effective environmentally friendly alternatives available that can replace the phosphonates HEDP and NTMP for the inhibition of $CaCO_3$ crystallization. These carboxymethyl inuline biopolymers are nontoxic, free of phosphorous, and inherently biodegradable. Therefore, they will have much less impact on the environment. This novel class of antiscalants demands further research that addresses their stability and effectiveness in the process equipment at various temperatures and under influence of metal ions like manganese and iron.

Besides carboxymethyl inulin biopolymers, natural organic matter, like humic acids, is also known to inhibit the precipitation and growth of scaling salts (2, 3). Therefore, it would be worthwhile to investigate their potential as antiscalant as well. A fraction with a specific average molecular weight and a high number of carboxylic acid groups could be isolated and purified that may effectively be employed as antiscalant formulation.

10.4 Phosphonate removal from other waste water streams

This work shows that the discharge of phosphonate antiscalants along with the RO membrane concentrate can be avoided. However, RO desalination is not the only or the largest market for phosphonate antiscalants. According to Thermphos, one of the world's largest producers of phosphonates, more phosphonates are currently being consumed for scale control in oil fields and cooling waters. Especially the usage of phosphonates in cooling waters is of concern, because cooling waters generally are being discharged on surface waters. It will probably be more difficult to replace these phosphonates with environmentally friendly alternatives because in heat exchange equipment phosphonates not only function as scale inhibitor, but they also serve as effective corrosion inhibitors (4, 5) and are known for their high thermal stability (6).

It is reasonable to expect that the technology presented here is also applicable for treating cooling water streams, since they have a similar pH and also contain an excess calcium concentration, which will enhance the

phosphonate adsorption process. However, a difference can be expected between the temperatures of wasted cooling waters and RO membrane concentrates. Water streams produced in oil fields may even be hotter (up to 75 °C). Thus, the determination of the adsorption isotherms and adsorption kinetics at elevated temperatures is of considerable practical value, as well as being essential for the design and control of adsorption processes to treat these streams. Although phosphonates are frequently used in household products, like dishwater tablets and washing powders, they do not impose a direct threat to the marine environment. It has been shown that after their discharge in the sewage, phosphonates are removed almost completely in the municipal waste water treatment plants (7), most likely by adsorption onto activated sludge, iron oxides and other natural organic matter (8). Therefore, the surplus value of phosphonate removal via adsorption onto iron oxy-hydroxides will be low for these waste water streams.

10.5 References

(1) Wagterveld, R. M.; Miedema, H.; Witkamp, G. J. Effect of ultrasonic treatment on early growth during $CaCO_3$ precipitation. *Cryst. Growth Des.* **2012**, *12*, 4403-4410.

(2) Hoch, A. R.; Reddy, M. M.; Aiken, G. R. Calcite crystal growth inhibition by humic substances with emphasis on hydrophobic acids from the Florida Everglades. *Geochim. Cosmochim. Acta* **2000**, *64*, 61-72.

(3) Lebron, I.; Suarez, D. L. Calcite nucleation and precipitation kinetics as affected by dissolved organic matter at 25 °C and pH > 7.5. *Geochim. Cosmochim. Acta* **1996**, *60*, 2765-2776.

(4) Labjar, N.; Lebrini, M.; Bentiss, F.; Chihib, N.-E.; Hajjaji, S. E.; Jama, C. Corrosion inhibition of carbon steel and antibacterial properties of aminotris-(methylenephosphonic) acid. *Mater. Chem. Phys.* **2010**, *119*, 330-336.

(5) Nakayama, N. Inhibitory effects of nitrilotris(methylenephosphonic acid) on cathodic reactions of steels in saturated $Ca(OH)_2$ solutions. *Corros. Sci.* **2000**, *42*, 1897-1920.

(6) Martell, A. E.; Motekaitis, R. J.; Fried, A. R.; Wilson, J. S.; Macmillan, D. T. Thermal-decomposition of EDTA, NTA, and nitrilotrimethylenephosphonic acid in aqueous solution. *Can. J. Chem.* **1975**, *53*, 3471-3476.

(7) Jaworska, J.; Van Genderen-Takken, H.; Hanstveit, A.; van de Plassche, E.; Feijtel,

T. Environmental risk assessment of phosphonates, used in domestic laundry and cleaning agents in The Netherlands. *Chemosphere* **2002**, *47*, 655-665.

(8) Nowack, B. Aminopolyphosphonate removal during wastewater treatment. *Water Res.* **2002**, *36*, 4636-4642.

APPENDIX: A

LANGMUIR PARAMETERS

Table A1. Parameters obtained from the Langmuir fits of the adsorption isotherms for Amberlite IRA-410, Amberlite IRA-900 and SAE-Super.

Adsorbent	Parameter	Units	Solution						NF-concentrate
			1	2	3	4	5	6	pH 7.0
IRA-410	Γ_{max}	mg g^{-1}	144	67.4	61.2	127	87.7	107	19.1
	$\Gamma_{12.5}$	mg g^{-1}	142	21.1	33.4	2.13	9.42	9.30	6.17
	K_{ads}	dm^3 kg^{-1}	5170	36.5	96.4	1.36	9.63	7.56	38.2
	$\Delta G_{0,ads}$	kJ mol^{-1}	-21.2	-8.92	-11.3	-0.76	-5.61	-5.01	-9.03
	R^2	-	0.993	0.990	0.996	0.999	0.992	0.992	0.941
IRA-900	Γ_{max}	mg g^{-1}	167	28.8	31.8	-	31.3	80.0	11.4
	$\Gamma_{12.5}$	mg g^{-1}	114	4.23	7.03	0.466	2.31	2.31	2.91
	K_{ads}	dm^3 kg^{-1}	2960	13.8	22.7	0.207	6.36	2.38	27.3
	$\Delta G_{0,ads}$	kJ mol^{-1}	-19.8	-6.51	-7.74	3.90	-4.59	-2.15	-8.20
	R^2	-	0.973	0.983	0.999	0.995	0.983	0.973	0.889
SAE-Super	Γ_{max}	mg g^{-1}	7.92	27.9	4.05	5.77	24.8	39.9	2.61
	$\Gamma_{12.5}$	mg g^{-1}	2.48	1.91	0.86	1.19	0.52	0.85	1.68
	K_{ads}	dm^3 kg^{-1}	36.6	5.87	21.5	20.8	1.71	1.73	0.145
	$\Delta G_{0,ads}$	kJ mol^{-1}	-8.92	-4.39	-7.61	-7.52	-1.33	-1.36	-12.3
	R^2	-	0.923	0.907	0.864	0.954	0.981	0.887	0.917

APPENDIX: B
MATLAB COMPUTER CODES

Parameter description:

cb	dimensionless liquid-phase concentration at any time *t*
c0	initial liquid-phase concentration
cp	dimensionless concentration of adsorbate in the pores at any time *t*
Dp	effective pore diffusivity
Ds	effective surface diffusivity
epsilon	particle porosity
k0	constant in the Freundlich isotherm
n	exponent in the Freundlich isotherm
q	dimensionless amount adsorbed on the surface
rho	particle density
tau	dimensionless time
te	total time of the adsorption process
t	dimensionless duration of one time step
x	dimensionless radial coordinate of the particle

Parameter estimation surface diffusion model (SDM)

Main program for parameter estimation:

```
clear all           %   Clear all variables in function
workspace
close all           %   Close all figures
clc                 %   Clear command window

global cb q k index q0 Bi par p

warning off

imax=180; jmax=50; npar=2; Nmax=100;
Xc=zeros(imax,jmax,npar);
RESNORMc=zeros(imax,jmax);
RESIDUALc=zeros(imax,jmax,Nmax);

exp_ind='0803B_F'                          %  Experiment ID
parfilename = ['GFH_parameters_',exp_ind];
```

```
load(parfilename)                              %  load parameter
values

for i=1:imax
    for j=1:jmax


% - Change scaling factors
    Ds =  0.005*(-29+i*30e-15*1e15);
    kf = 0.05*(-2+j*4e-5*1e5)/2;
    p.Ds  =   Ds*1e-15;
    p.kf  =   kf*1e-5;

    par   =   [Ds kf];

    p,par

load experimental_data            %  load experimental data

   var_name_t=['t_exp_0803B']; var_name_C=['C_exp_0803B'];
   data(1,:) = eval(var_name_t)';  data(2,:) =
eval(var_name_C)';

% - Simulation mode
       [F,Out]=adsorptionSDM_F_RSM(par,data);

% - Calculation residuals from experimental data and simulation
       e = F';
       X = par';
       RESNORM = e'*e;
       RESIDUAL= e;

       Xc(i,j,1:npar)=X;
       MSE(i,j)=RESNORM./(length(data(1,:))-2);
       RESIDUALc(i,j,1:length(RESIDUAL))=RESIDUAL;
    end;
end;
if size(MSE)~=[1 1]
figure(1);mesh([Ds/imax:Ds/imax:Ds],[kf/jmax:kf/jmax:kf],MSE');
figure(2);contour(log10([Ds/imax:Ds/imax:Ds]),[kf/jmax:kf/jmax:
kf],MSE',200);
end;
return;
```

Function that evaluates the SDM model in dimensionless form:

```
function [F,Out]=adsorptionSDM_F_RSM(par,data)

global cb q k index q0 Bi p
Ds       =   par(1)*1e-15;     %  effective surface diffusivity
```

```
kf        =   par(2)*1e-5; %  external mass transfer coefficient

te        =   4.8;                    %  time (h)

tau       =   (Ds*te*3600)/(p.R0^2);  %  Dimensionless time
dt        =   tau/99;
tstep     =   (tau/dt)+1;
cb        =   1;
q         =   zeros(3,51,101);
q_out     =   zeros(3,51,101);
cb_array =   ones(101,1);
cp        =   zeros(3,51,101);

% - Value of q corresponding with c0 according to the
Freundlich isotherm
q0       =   p.k0*(p.c0^(p.n));
Bi       =   (kf*p.R0*p.c0)/(Ds*p.rho*q0);     %  Biot number
dg       =   (p.w/p.v)*(q0/p.c0);  % solute distribution
parameter
m = 2;                       %  Parameter for spherical geometry

 for k = 1:tstep;

     index = 0;
     x = 0:(1/50):1;          %  50 points in the x-direction
     t = [0 dt/2 dt];

% - Algorithm that solves the non-linear parabolic partial
differential equation
     sol = pdepe(m,@SDM_eq,@SDM_IC,@SDM_BC_F,x,t);

% - Extracts the first solution component as q
     q(:,:,k+1) = sol(:,:,1);

% - Average loading particle
     q_av = 3*trapz(x,q(3,:,k+1).*x.^2);
     q_av_out(k+1,:) = q_av;

% - Overal mass balance bulk liquid in nondimensional form
    cb = 1-(dg.*q_av);
    cb_array(k+1) = cb;

 end
% - Measurement selection for initial guess parameters
te_m = data(1,:); ce_m = data(2,:);
cb_hat    = interp1(0:te/tstep:te,cb_array,te_m);
Out   = cb_hat;
% - Residuals
F=(ce_m-cb_hat);
J = F*F'/(length(F)); disp('MSE: '); disp(J);
```

Subfunction that evaluates the boundary conditions components:

```
function [pl,ql,pr,qr] = SDM_BC_F(~,ql,cb,qr,~)

global cb k index q0 Bi par p

Ds      =   par(1)*1e-15;
kf      =   par(2)*1e-5;


% - Value of q corresponding with c0 according to the
Freundlich isotherm
q0      =   p.k0*(p.c0^(p.n));
Bi      =    (kf*p.R0*p.c0)/(Ds*p.rho*q0);

pl = ql;
ql = 0;
% - Boundary condition at the sphere surface
pr = -Bi.*(cb-((qr.*q0./p.k0).^(1/p.n).*(1/p.c0)));
qr = 1;

end
```

Subfunction that evaluates of differential equation components:

```
function [c,b,s] = SDM_eq(x,t,q,DqDx)

c = 1;
b = DqDx;
s = 0;

end
```

Subfunction that evaluates the initial conditions components:

```
function qi = SDM_IC(q)

global q k index

index = index + 1;
qi = q(3,index,k);

end
```

Parameter estimation pore diffusion model (PDM)

Function that evaluates the PDM model in dimensionless form:

```
function [F,Out]=adsorptionPDM_F_RSM(par,data)

global cb cp k index q0 par beta p

Dp        =   par(1)*1e-10;        %  effective pore diffusivity
kf        =   par(2)*1e-5;
te        =   5;
tau       =   (Dp*te*3600)/(p.R0^2);
dt        =   tau/399;
tstep     =   (tau/dt)+1;
cb        =   1;
q         =   1e-24*ones(3,51,401);
q_out     =   1e-24*ones(3,51,401);
cb_array =   ones(401,1);
cp        =   1e-24*ones(3,51,401);

q0        =   p.k0*(p.c0^(p.n));

% - Dimensionless variables

Bi        =   (kf*p.R0)/(Dp*p.epsilon);
alpha     =   (p.w*p.epsilon)/(p.v*p.rho);
beta      =   (p.rho*q0)/(p.c0*p.epsilon);

m = 2;

for k = 1:tstep;

    index = 0;
    x = 0:(1/50):1;
    t = [0 dt/2 dt];
    sol = pdepe(m,@PDM_eq_F_RSM,@PDM_IC,@PDM_BC_RSM,x,t);
    cp(:,:,k+1) = sol(:,:,1);

% - Dimensionless concentration of adsorbate at the particle
surface related to the dimensionless pore concentration by the
Freundlich isotherm

    q = p.k0.*p.c0.^p.n.*(1/q0).*(cp.^(p.n));

    q_out(:,:,k+1) = q(:,:,1);

% - Overal mass balance bulk liquid in non-dimensional form

cb = 1-
(3*alpha*trapz(x,((beta.*q(3,:,k+1)+cp(3,:,k+1)).*x.^2)));
```

```
cb_array(k+1) = real(cb);

end

te_m = data(1,:); ce_m = data(2,:);
cb_hat   = interp1(0:te/tstep:te,cb_array,te_m);
Out  = cb_hat;

F=(ce_m-cb_hat);
J = F*F'/(length(F)); disp('MSE: '); disp(J);
```

Subfunction that evaluates the boundary conditions components:

```
function [pl,ql,pr,qr] = PDM_BC_RSM(~,cpl,cb,cpr,~)

global cb par p
Dp     =   par(1)*1e-10;
kf     =   par(2)*1e-5;

Bi     =   (kf*p.R0)/(Dp*p.epsilon);

pl = cpl;
ql = 0;
pr = -Bi.*(cb-cpr);  % boundary condition at the sphere surface
qr = 1;

end
```

Subfunction that evaluates of differential equation components:

```
function [c,b,s] = PDM_eq_F(~,~,cp,DcpDx)

global p

c = 1+((1-
p.epsilon).*((p.rho/p.epsilon).*p.k0*p.n.*(p.c0.*cp).^(p.n-
1)));
b = DcpDx;
s = 0;

end
```

Subfunction that evaluates the initial conditions components:

```
function cpi = PDM_IC(cp)

global k cp index

index = index + 1;

cpi = cp(3,index,k);

end
```

APPENDIX: C

INPUT PARAMETERS ADSORPTION COLUMN MODELING

Table C1. Input parameters for modeling the column adsorption experiments and results of the column regeneration

Adsorption								*Regeneration*		
Solution	***EBCT***	R_0[(a)]	t_{bt}[(b)]	D_s	***Bi***	***St***	D_g	***NaOH***	V_r/V_b	***H***[(c)]
		$\times 10^{-4}$		$\times 10^{-15}$						
	(s)	***(m)***	***(h)***	$(m^2\ s^{-1})$	***(-)***	***(-)***	***(-)***	***(M)***		***(%)***
SC 1	34	4.5	1.2	4.0	316	1.62	44251	0.1	2 × 17	34 -> 44
	34[(d)]	4.5	3.1	3.5	258	1.62	61957	0.1	2 × 17	36 -> 43
	20	4.5	0.4	3.0	421	0.95	44252	-	-	-
	20	4.5	0.4	3.0	421	0.95	44252	0.1	297	65
	33	4.5	1.5	4.2	301	1.59	44252	0.1	292	70
	33	3.5	2.0	3.2	307	2.08	62982	0.5	37	43
SC 2	34	4.5	0.9	3.5	361	1.62	44252	-	-	-
	20	4.5	0.4	4.4	287	0.97	44252	0.1	67	37[(e)]
	32	3.5	2.0	3.2	307	2.08	62982	-	-	-
	20	3.5	0.5	3.2	307	1.25	62982	0.1	62	52
	32[(d)]	3.5	3.9	2.5	281	2.08	88180	-	-	-
	20	1.7	4.4	3.2	149	2.68	75731	-	-	-
	32	1.7	15.3	4.2	114	4.40	75731	-	-	-

(a) average value of the particle radius; (b) breakthrough time corresponding with $c_b/c_0 = 0.2$; (c) maximum efficiency; (d) c_0 = 10 g m^{-3} in these experiments; (e) regeneration done in continuous mode;

All input parameters were based on the same wet weight values.

Table C2. Properties of the differently sized GFH grains.

Grain size (*mm*)	R_0 **×10^{-4}** (*m*)	**Water content** (%)	ρ_p **wet adsorbent** (*kg dm^{-3}*)	ρ_b **wet adsorbent** (*kg dm^{-3}*)	ε_b (a)
0.5 - 2.0	4.5	55.0	1.55	1.29	0.2
0.5 - 1.0	3.5	57.0	1.53	1.36	0.1
0.2 - 0.5	1.7	56.3	1.55	1.39	0.1

(a) $\varepsilon_b = 1 - \rho_b / \rho_p$

Table C3. Calculation Reynolds numbers and k_f.

R_0 **×10^{-4}** (*m*)	φ_v **×10^{-7}** (*m^3 s^{-1}*)	ν_f **×10^{-3}** (*m s^{-1}*)	**Re** (-)	k_f (a) **×10^{-5}** (*m s^{-1}*)
4.5	1.05	2.1	2.3	2.5
4.5	1.72	3.4	3.8	3.3
3.5	1.05	2.1	1.6	2.6
3.5	1.72	3.4	2.6	3.4
1.7	1.05	2.1	0.8	3.8
1.7	1.72	3.4	1.3	4.8

(a) calculated from the Wakao and Funazkri correlation.

APPENDIX: D

EFFECT OF ULTRASOUND ON CALCITE GROWTH

Table D1. Seeded calcite growth in the presence of NTMP: effect of ultrasound on R_i and t_i as a function of NTMP concentration. Conditions: $[Ca^{2+}] = [HCO_3^-] = 2$ mM, $S = 2.48$, pH = 8.65, IS = 0.1 M, $T = 298$ K

Experiment	Ultrasound (45 min)	[NTMP] ($mg\ dm^{-3}$)	R_i $\times 10^{-6}$ ($mol\ g^{-1}\ min^{-1}$)	$R_{i,I}$ $\times 10^{-5}$ ($mol\ m^{-2}\ min^{-1}$)	t_i (min)
1	no	0	38.0	22.4	0
2	no	0	37.8	22.2	0
3	no	0	35.9	21.1	0
4	no	0	38.3	22.6	0
5	no	0	39.0	22.9	0
7	no	0.01	26.2	15.4	50.9
8	yes	0.01	27.2	-	36.4
9	no	0.03	3.63	2.14	167
10	no	0.03	3.47	2.04	115
11	yes, 95 min	0.03	6.40	-	70.4
12	no	0.03	2.65	1.56	164
12	no	0.03	4.94	2.91	75.0
12	no	0.03	3.50	2.06	98.0
12	no	0.03	3.45	2.03	88.0
13	yes	0.03	4.77	-	125
13	no	0.03	4.11	-	95.0
13	no	0.03	3.01	-	112
13	no	0.03	2.56	-	131
14	yes	0.03	5.84	-	116
14	yes	0.03	8.13	-	57.0
14	yes	0.03	6.74	-	66.0
14	yes	0.03	7.14	-	60.0
15	no	0.04	0.49	0.290	741
16	no	0.04	0.57	0.335	786
17	yes	0.04	1.33	-	171
18	yes	0.04	1.33	-	177
19	no	0.05	0.54	0.318	805

20	no	0.05	0.38	0.224	819
21	yes	0.05	0.92	-	306
22	yes	0.05	1.04	-	

ACKNOWLEDGEMENTS

I am sincerely and heartily grateful to my promoter, Geert-Jan Witkamp, for the guidance, support and encouraging attitude he showed me throughout my research project. Besides I would like to thank Martijn Wagterveld for the successful collaboration, useful discussions and for his pleasant company during the courses and conferences we have visited together. I owe sincere and earnest thankfulness to Karel Keesman for his enthusiasm and help with modelling in Matlab and with the writing of Chapter 3. I would also like to express my thanks to Mateo Mayer and Maarten Biesheuvel for their useful advices.

I am also truly indebted and thankful to the students who have helped me by doing their internship or master thesis research within my project: Taina Tervahauta, Rutger Beckers, Monika Jarzembowska, Adriaan van den Bruinhorst, and Maria Valero Fabregat.

I would also like to thank the good technical and analytical staff at Wetsus: Wim Borgonje, Jan Tuinstra, Harrie Bos, Harm van der Kooi and Ernst Pandstra, thank you for your technical support. Jelmer Dijkstra, Mieke de Haan, Janneke Tempel and Marianne Heegstra thank you for analysing my thousands of ICP samples. Besides, I would like to thank Ton van der Zande for his help with Raman analysis.

My gratitude also goes to all my colleagues at Wetsus. Marco, Elsemiek, Lucia, David, Urania, Joao, Jordi, Joeri, and Pedro for the pleasant working atmosphere in our office. I would also like to thank Camiel Janssen for his conversations, Kamuran Yasadi for his help with FT-IR analysis, and Arie Zwijnenburg for his SEM courses. Adriaan Jeremiasse, Piotr Dlugolecki and Pieter Wartena thank you for the very nice motorbike trips.

I would like to thank all the others for making my time at Wetsus pleasant and rewarding.

My gratitude goes also to the members of the "Concentrates" theme, especially Albert Janssen, Koos Baas and Ron Jong. Thank you for your support.

Finally, I would like to thank my beloved Sonja for her patience, help and for presenting me with two beautiful daughters, Marin and Amber.

ABOUT THE AUTHOR

Luciaan Boels was born 8th of May 1984 in Emmen, The Netherlands. After finishing his pre-university education at the Hondsrug College in Emmen in 2002, he studied Chemical Engineering at the Groningen University and obtained his Master of Science degree (cum laude) in 2007. In 2008, he started his PhD research at Wetsus, Centre of Excellence for Sustainable Water Technology in Leeuwarden under the supervision of Prof. Dr. Geert-Jan Witkamp at the Delft University of Technology. In 2010 his research was awarded the Marcel Mulder prize. Since the 1st of September 2012 he works for Shell as a research engineer in enhanced oil recovery.